Investigation of Gravity Based Separation of Immiscible Liquids

by

©Weiwei E

A Dissertation submitted to the School of Graduate Studies in partial fulfillment of the requirements for the degree of

Doctor of Philosophy

Faculty of Engineering and Applied Science

Memorial University of Newfoundland

May 2020

St. John's Newfoundland

Abstract

Separation of oil and water plays an important role in oil production and other industries. Separation efficiency is a key factor for oil and gas production equipment, such as compressors and water treatment equipment. Thus, the improvement of oil / water separation efficiency is a task of increasing importance for the industry, especially manufacturers of separation equipment.

This thesis analyzes the separation of oil from an oil / water mixture and, in particular, the coalescence of oil droplets formed during separation by using a combination of experimental and numerical modeling methods. A gravity-based separator is designed and built to conduct optimization experiments on a continuous oil/water separation process. Another laboratory-scale experimental setup is developed to investigate and optimize a batch separation process.

Two-dimensional Computational Fluid Dynamics (CFD) models are developed using the Fluent Software package with the same geometric profiles of the two experimental models to investigate further the effects of a broader range of operating conditions on the separation process systematically. In addition, two other available software packages, OpenFoam and Flow-3D, are explored to model the oil / water separation process for the Base Case. The results show that they were not as accurate as Fluent but much faster.

A new semi - analytical model is developed to predict liquid / liquid separation

dynamics with a focus on water / oil mixtures. The model employs a force balance on the droplets to predict the rising velocity of the oil phase. The effect of droplet coalescence on the droplet's rising velocity is investigated, and a new correlation is developed that predicts the coalescence rate based on the oil / water fraction, and the initial droplet diameter. Numerical simulations of a batch oil / water separation process are conducted to develop the droplet coalescence. An equivalent experiment is conducted, and the experimental results are found to agree well with the numerical predictions (relative error of 13.39 %). The proposed semi-analytical model can predict the rate of separation with a relative error of 6.35 % compared to full numerical predictions. The analytical model provides an alternative technique to predict the separation of liquid / liquid mixtures at a much lower computational cost, useful for initial design or analysis of separation scenarios.

Finally, a new geometric design correlation is developed using a non-dimensional analysis method. A parametric study of numerical predictions conducted with CFD Fluent is employed to investigate several critical variables that affect the separator design. Additionally, a series of simulations are conducted to validate the correlation model by changing the value of dimensionless groups. The correlation results show that increasing the Reynolds and Euler numbers require a separator with a longer length to height ratio to achieve the same separation efficiency. However, an increase in the Weber number requires a separator with a smaller length to height ratio.

Acknowledgements

I would like to express my sincerest thanks and appreciation to my supervisor Kevin Pope, without whose support and guidance this research would not be possible. It is a great honor to work under his supervision. I also wish to thank Dr. Xili Duan for his mentoring and constructive comments on my thesis. Also, I wish to Dr. Yuri Muzychka for his creative and comprehensive advice making this work a success.

I am also thankful for the financial support from the Natural Sciences and Engineering Research Council of Canada (NSERC) and the Research & Development Corporation (RDC) support for building the flow loop.

My gratitude also goes to Dr. Zongming Wang, Craig Mitchell, Greg O'Leary, and Brian Pretty for their remarkable help, knowledge, and patience concerning my experimental study. I wish to thank Flow Sciences for providing me a free four-month Flow3D research license for my project. I would also like to acknowledge the support and help from all my friends, particularly from Mr. Mark Walsh, a great friend who supported me during my research.

Finally, a sincere thank you to my parents and my family who support me in every possible way with their understanding, patience, and encouragement throughout my entire Ph.D. study journey. Without your sacrifices, I would not be able to achieve this degree.

This thesis is dedicated to you.

Table of Contents

List of Tables

List of Figures

List of Abbreviations and Symbols

Abbreviations

2-D	Two dimensions
3-D	Three dimensions
API	American petroleum institute
CFD	Computational fluid dynamics
DAQ	Data acquisition system
DOE	Design of experiments
GPM	Gallon per minute
LLCC	Liquid / liquid cylindrical cyclone
MPS	Moving particle semi-impicit
N-S	Navier-Stockes equation
PBE	Population balance model
RNG	Re-normalization group
RSM	Response Surface Methodology
RTD	Residence time distribution
S-S	Steady state
T	Temperature
UDF	User defined function
VOF	Volume of fluid model

Nomenclature

a	constant
b	constant
c	constant
A_h	separator horizontal area, m^2
A_C	separator cross-sectional area, m^2
C_D	drag coefficient
d	droplet diameter, m
E	separation efficiency
f	original volume fraction
f', f''	linear function
F	force, N
g	gravitational acceleration, m/s^2
G	gravitational force, N
h	separator vertical height, m
$h\prime$	separated phase thickness, m
H	interface vertical location,, m
L	theoretical length of separator, m
M	mass of droplet, kg
n	binary droplet coalescence step
r	radius of droplet, um
P	pressure, Pa
Q	flow rate, m^3/s
v	droplet velocity, m/s

v_i	variables
v'	the moving speed of the interface, m/s
V	volume of fluid, m^3
W	width of separator, m
x	separator horizontal length,, m
Y	droplet rising distance, m
Y'	dimensionless distance

Greek symbols

ρ	density, kg/m^3
σ_R	uncertainty
Π_i	dimensionless group
τ	residence time, s
μ	dynamic viscosity, $kg/m \cdot s$
ν	kinematic viscosity, m^2/s
ϕ	dependent variable
Γ_ϕ	exchange coefficient
V	flow velocity vector
S_ϕ	source of the variable
σ	surface tension, N/m
ε	volume fraction of fluid
θ	angle, $^\circ$
δ	change of value

Subscripts

b	buoyancy
c	cross section
co	coalescence
d	drag
D	dimensionless
f	force
h	horizontal
h_1	separated oil phase height
h_2	unseparated oil height
in	inlet
m	mixture
o	oil
ori	original value
o/w	oil droplet in water
out	outlet
r	rise distance
s	single drop
$s-s$	steady-state
v	vertical direction
w	water
w/o	water droplet in oil

Chapter 1

Introduction

1.1 Background

Liquid / liquid separation for different density liquids is an important process in the petroleum, pharmaceuticals, and environmental protection industries. In recent years, with the development of subsea processing equipment, the petroleum industry has become more interested in subsea reservoirs [1–7]. Subsea equipment can include separators, pumps, and long-distance pipe lines [1]. As subsea separation requires moving to higher pressure applications, a requirement for the development of more advanced separation technologies that can provide enhanced performance with improved compactness and reduced costs while operating at higher subsea pressures is becoming more important. Terje et al. [2] provides detailed information about subsea oil production, water removal strategies, existing problems, marine operations, and safety concerns regarding an oil / water subsea separator installed offshore Brazil. This station is 29 m long, 10.8 m wide, 8.4 m high, and has an overall weight around 394 tonnes [3].

In recent years the advancement of the petroleum industry into deeper water and

harsher environments requires more effective and productive separators. Considering safety and financial costs, the performance prediction of these separators under the subsea operation conditions is a highly significant part of the design process.

Based on the literature review conducted as part of this study, there is room remaining to improve the design and efficiency of these subsea separation systems. This can be accomplished with the use of numerical modeling, provided that such models can be validated by reference to experimental work, or in some cases, other numerical models.

Oil and water multiphase flow separation technologies have been widely studied for many decades. The fundamental operating principle for oil / water separation is based on the density difference. Andrew [8] summarizes gravity separation methods as follows: jigs, pitched sluices, spirals, shaking tables, fine particle separators, and sizing. Most separators are designed based on the idea of a droplet force imbalance to separate oil from water. Therefore, the separation process is relatively slow and inefficient. Tremendous efforts have been made to improve the performance of separators, ranging from internal structure design improvement to optimization of operating conditions. Based on current technology, gravity-based oil / water separators fall into two categories: horizontal separators and vertical separators. Each type of them has advantages and weaknesses. Horizontal separators perform at high processing capabilities rates, but the separators occupy large spaces. Conversely, vertical separators require little plot space, and can be more easily transported and installed than horizontal separators; however, they have relatively small capacities compared to horizontal separators [9].

A better understanding leads to the ability to model the internal processes and improve separation efficiency or optimize separator design. With the development of modern technology, using computer-aided tools to predict and simulate the separation

process is potentially very beneficial. Computational fluid dynamic (CFD) simulation method is widely used to investigate the oil / water separation process and the separator design. Due to the complexity combined with the non-linear and time-dependent nature of oil / water separation, it is a general challenging to analytically solve this class of problems. However, analytical models can offer a relatively quick insight into separation processes, or separator design, at the early stages of design or evaluation. Although significant computational separator research has been conducted in the last six decades, there are still relatively few published papers in which analytical models have been developed to cover the oil / water separation process.

1.2 Scope and Objective

In the petroleum industry, due to the shape dependency of separator technology on the economic performance and separation efficiency, current problems require studies and analyses oriented specifically to the geometries used in that industry for oil / water separation processes. Due to the wide use of gravity-based separators, this study focuses on those oil / water separation processes. The study aims to improve numerical models and to develop analytical models by combining them with the experimental method. The CFD simulation method, semi - analytical modeling method, and dimensional analysis method are used in this study.

The overall research objective of the work is to explore methods of numerical and analytical modeling that can be applied to separators to better understand the liquid / liquid separation dynamics.

The sub tasks to achieve this overall objective are:

1. Develop high level semi-analytical models of droplet coalescence to guide separator design.

2. Develop simple physical models that can be applied at normal pressures and temperatures in order to validate or calibrate the analytical and numerical models.

3. Analyze and compare results using a non-dimensional framework to determine general guidelines for the effects of the operational parameters on separator dimensions and operations.

1.3 Methodology

In this study, three basic methodologies, analytical, simulation, and experimental methods are used. The combinations between each methodology are presented in Figure 1.1. Analytical models are first developed to aid in separator design. Then a laboratory-scale separator is designed based on the analytical models. CFD models for separators are developed and validated based on the lab-scale experimental results. These CFD models are then used to model a wider range of operating parameters. Results from the comparison between CFD and experimental models are presented and discussed. Next, a correlation is developed using dimensional analysis that provides insight into the effect of various operating parameters on the required design dimensions of separators. Finally, conclusions, contributions, and suggestions for future work are presented.

1.4 Outline of the thesis

The thesis is organized in nine chapters as follows:

- **Chapter 2** presents a review of previous studies of oil / water separation and separators. The literature review is focused on three research methods: experi-

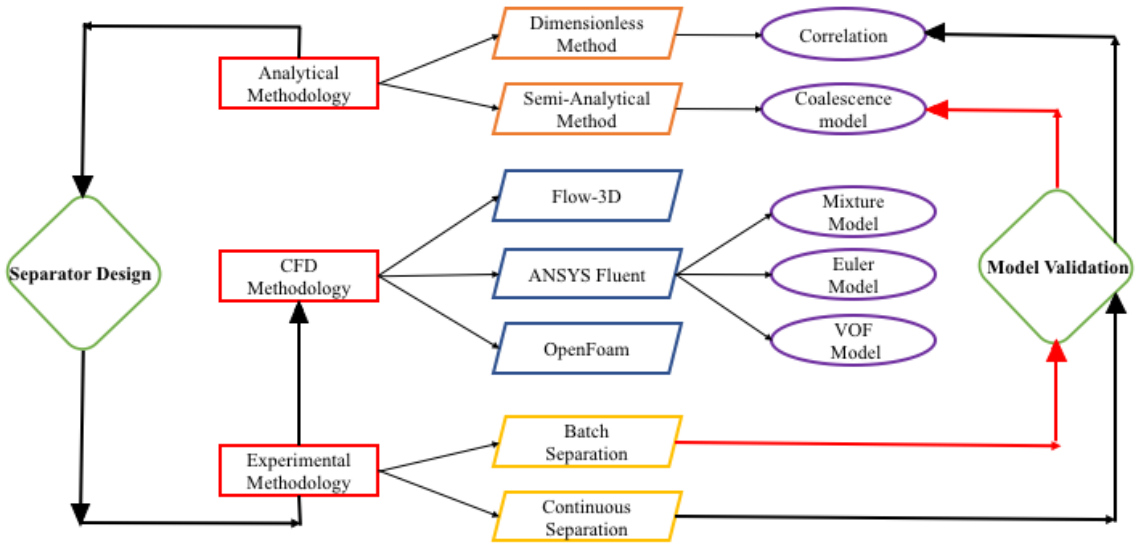

Figure 1.1: Methodology flowchart

mental methods, CFD simulation methods, and analytical methods.

- **Chapter 3** develops an improved analytical model for separator design and oil / water interface tracking. Oil droplet rising velocity theory and droplet coalescence theory are also discussed in this chapter.

- **Chapter 4** presents the development of laboratory-scale separators for batch separation and continuous separation. For continuous separation, an industry-scale horizontal separator is designed. In addition, an uncertainty analysis for both experimental studies is presented in this chapter.

- **Chapter 5** presents the development of numerical simulation studies. ANSYS Fluent, Flow-3D, and OpenFOAM simulation geometries and formulations are presented in this chapter. Also, a mesh independence study and the rationale for the model selection of Fluent are also discussed in this chapter.

- **Chapter 6** develops and discusses a semi-analytical model for droplet coales-

cence. The coalescence model is developed based on the binary coalescence process. In addition, an algorithm developed for interface tracking of the oil / water interface.

- **Chapter 7** presents the numerical work to model the oil / water separation process for the various operating conditions used during the experimental trials to validate the numerical simulation model.

- **Chapter 8** shows the correlation developed based on dimensional analysis to calculate the oil / water separation processes, which can be used to guide separator designs.

- **Chapter 9** presents conclusions and contributions of the thesis work and suggests recommendations for future work.

Chapter 2

Literature Review

2.1 Multiphase Separation Background

The separation of immiscible liquids by using gravity is a physical process that is common in the chemical and petroleum industries [10–13]. Oil / water separation has been studied both experimentally and theoretically by numerous investigators in the past few decades. Two-phase oil / water separators are important in the oil extraction industry to separate water from the produced oil. The separation efficiency directly affects the performance of downstream oil processing equipment. Therefore, various studies focus on this critical area using experimental, numerical, and analytical methods. This chapter reviews the important literature on experimental, numerical, and analytical methods for multiphase separators to reflect the current state of the art and address recent findings.

2.2 Gravity Based Separators

Gravity separators are designed to separate immiscible phases with different densities. There are a number of parameters that affect the performance of a separator, such as

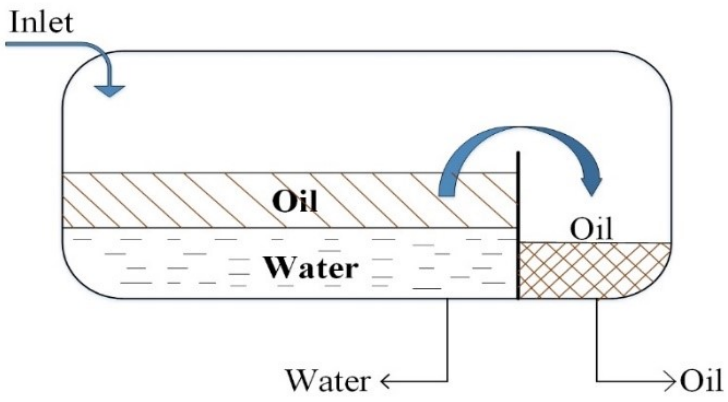

Figure 2.1: Schematic of the Gravity Horizontal Separator

the separator dimensions, number, type, location of baffles, and residence time [14,15]. Horizontal separators generally have a larger capacity and longer residence time, which results in a better separation efficiency [16, 17]. Most of the research shows that horizontal separators are more economical and provide higher separation efficiency; however, vertical separators are more suitable for space-limited areas.

Gravity-based separation relies on the difference between the specific gravity of oil and water. The most common form of the multiphase separator is a horizontal or vertical tank that has the function of providing a relative residence time for the light phase to coalesce and separate from the heavier phase. The detailed differences between the two types of gravity separators are described in the following.

The typical structure of horizontal gravity separator is shown in Figure 2.1 (Redrawn from API, 1987 [18]). In this type of separator, the multiphase fluid stays in the settling section to be segmented. In the segment section, oil droplets coalesce. With sufficient residence time, oil and water separate into two distinct phases. During the separation period, the oil droplets' rising velocity is perpendicular to the incoming flow.

One of the most important criteria for the design of a horizontal separator is the

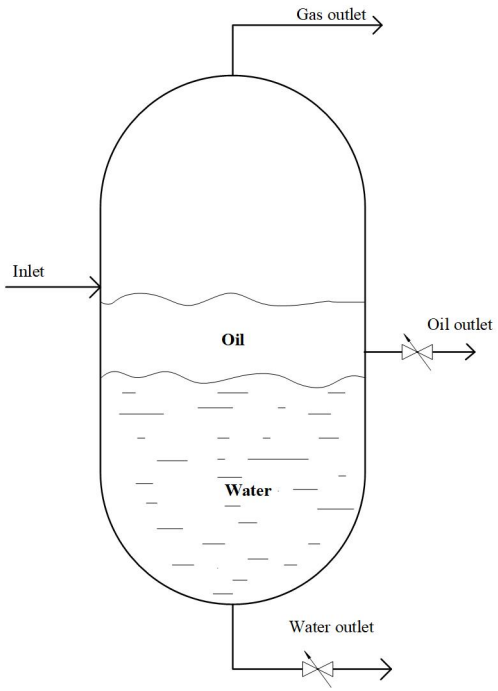

Figure 2.2: Schematic of the Gravity Vertical Separator

volume of the liquid collection segment. To obtain a high separation efficiency, the segmented zone must provide enough residence time for oil droplets to rise from the bottom of the separator to the top of the water phase.

Unlike horizontal separators, vertical separators need a relatively small space, and they are easier to move and install [19]. Due to its geometrical limits, a vertical separator typically provides less separation efficiency than horizontal designs. However, in a limited space area, like an off-shore platform, a vertical separator may be more suitable. The typical structure of a vertical separator is shown in Figure 2.2 (Redraw from API, 1987 [18]).

When designing a multiphase separator, the first factor that needs to be considered is the orientation. Based on Smith and Stewart's studies [20, 21], horizontal separators generally have better separation efficiency and are more economical with high oil volume fraction fluids. The vertical separator is more often designed for cases

of separate fluids with low oil volume fraction. Although previous studies provide guidelines for choosing orientation, as highlighted by Svrcek and Monner [22], it is still necessary to consider all the influencing factors when determining which type is more suitable.

Many factors affect the separation efficiency of a separator. First is the operating conditions. Keller [23] presents a study of multiphase separation with oil density between 11 to 70 API gravity. In this study, the multiphase flow was injected into the separator, passing through a filter medium system to collect oil droplets. The filter medium has different mesh sizes that are affected by gravity. The design of this filter formed oil droplet size distribution pattern that increased uniformly and progressively from a small median size to a large median size. An experimental study of the separation process conducted by Padilla et al. [24] found that the average diameter of droplets increases dramatically in the vertical direction due to coalescence; however, in the horizontal direction, the average diameter showed small change. One of the reasons for this trend is due to the droplet coalescence process. Droplets with different sizes present different rising velocity; these droplets are moving relatively faster. Thus, droplets with different diameters located in different vertical locations. The thickness of the dispersion phase is related to the dispersed phase flow rate, not the total flow rate.

Second, the structure of a gravity separator directly affects the performance; therefore, many experimental studies focus on separator design. Rowley and Davies [25] proposed a sedimentation-oriented model, to produce more oil droplets between parallel plates, which enables the smallest oil droplets to coalesce faster in a gravity separator. Lars Schlieper et al. [26] investigated the separation behavior of a horizontal gravity separator with three different inner components. Their study mainly focused on the effect of the inflow, the plate material, and the plate distance, on

separation length within the separator. This study shows that the presence of inner components inside a separator, like plates, can aid the separation process. In 2009, Fitnawan et al. [27] investigated an inclined gravity downhole oil / water separator. In their paper, the performance effects of the separator's depth, inclination, tubing size, and tubing configuration were studied. Both experimental and simulation methods were used in the study. Their simulation results show that for a water volume fraction of approximately 81-87 %, the inclined separator was able to increase separation efficiency by up to 82 %.

Third, droplet size, which is one of the most critical factors that influence the separation efficiency. There is only limited experimental work has been conducted in this area. Jeelani et al. [28] developed a droplet population balance model in a flow system where oil is the continuous phase and water as the dispersed phase. The oil sample in this study has a viscosity of 56.5 mPa.s at 25 °C. Padilla et al. [24] used an experimental method to plot the droplet size distribution in the separator by changing the inlet flow rate. The study found that the size of the droplets slightly changed in the horizontal direction; however, there was a significant change in the vertical direction. The thickness of the emulsion layer depended on the flow rate of the dispersed phase, while it was independent of the total flow rate.

Forth, the mixing conditions of oil/ water also influence the separation efficiency in specific contexts. Yusuf et al. [29] conducted an experimental study to investigate the impact of oil viscosity on flow patterns. They used oil viscosity that is equal to 1.2 cp, and then compared it to oil viscosity at 1.6 cp. They observed differences in their flow pattern maps from those in previous studies. In addition, they investigated the oil viscosity effect on the pressure gradient. The results show that flow with oil viscosity at 1.2 cp presents a greater pressure gradient than oil viscosity equal to 1.6 cp.

Fifth, the type of separator also affect the separation efficiency. Besides gravity-based separators, centrifugal separators are another type of separator based on using the density difference of the immiscible liquids. The centrifugal separator has many advantages, like compact geometry, less weight, economic efficiency, and easy operation. In this type of separator, a swirling motion is produced by the tangential injection of pressurized fluid into the cyclone body. Liquid / Liquid Hydrocyclone (LLHC) is the most popular type of centrifugal separator. The typical structure of a hydro cyclone is shown in Figure 2.3 (Redrawn from [30], 2011). The multiphase flow enters through the inlet under high pressure to the swirl chamber. The lighter phase runs into the center, creates a reverse vortex flow, then leaves through the overflow outlet, while the denser phase moves to the wall of the cyclone and down the wall to the underflow outlet at the opposite end from the inlet [31]. Flow behaviors of oil / water multiphase flow in LLHC are very complex [13, 30, 32–34].

Zhang et al. [35] found that inlet pressure has a significant effect on the separation efficiency for a centrifugal separator. Their simulation results show that the separation efficiency reaches 100 % at 2 kPa, compared to separation efficiency 97 % at 10 kPa, which means that efficiency increased with the decrease of inlet pressure. Based on previous studies, Butin et al. [36] investigated a new centrifugal separator, the 3C cyclone separator, which is designed for a subsea bulk oil / water separation system. The 3C cyclone separator concept is based on an innovative geometry, aimed to improve the system flexibility for various operating conditions, considering the subsea operating environment. Compared to the traditional centrifugal separator, the 3C cyclone separator has a shorter length and more complicated internal structure to promote higher performance. The influence of flow rates, water volume fraction, oil viscosity, and oil droplet separation was studied using experimental methods. The flow rate is the main driver for the diameter of max oil droplet separation. When the

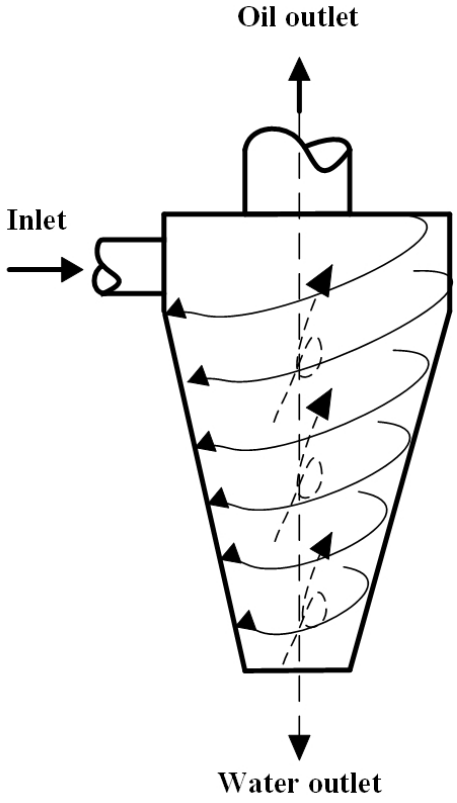

Figure 2.3: Schematic of the Centrifugal Separator

flow rates changes from 1 to 1.3 and 1.6 l/s, the max oil droplet diameters are 17, 12, and 10 μm, respectively. The study also found that the influence of the oil viscosity on the max oil droplet diameter is negligible since diameter only changes from 17 to 21 μm with an oil viscosity increase from 40 to 70 cP. The water volume fraction greatly influences the separation efficiency of the 3C cyclone separator.

In the petroleum industry, oil production in the last five decades has increased water volume fraction with produced oil; therefore, the transportation of both oil and water from the reservoir has become common. This gives rise to the study of drag reduction [37]. Eshrati et al. [38] studied the effect of oil fraction and the polymer-polymer mixture conditions on drag reduction. The percentage of polymer concentrations was in the range of 5 to 30 ppm. They proposed that the optimum polymer concentration is 10 ppm.

2.3 CFD Simulation Studies

Computational Fluid Dynamics (CFD) simulation is widely used to improve the design of separators and their operating conditions to enhance separation efficiency. Numerous studies have been published in these areas, especially for two-phase and three-phase flows.

This section presents a review of CFD-based studies for multiphase flow separation, especially oil-water flow systems. In Table 2.1, a summary of CFD simulation studies on operating conditions in horizontal separators is presented. Both two-dimensional (2-D) and three-dimensional (3-D) simulations are included. Operating pressure, flow rate, and fluid volume fraction are the typical variables that are investigated.

Table 2.1: CFD Separation Operating Conditions Literature Review

Authors	Modeling dimensions	Phases	Pressure (kPa)	Flowrate (m^3/h)	Volume fraction%	Temperature ($°C$)	Residence time (s)	Simulation model
Lee J. et al. [39]	3-D	Gas, oil, water	100, 400	Water: 491.87	Oil:85.5	42, 50	240, 330	—
Lee J. et al. [40]	3-D	Gas, oil, water	690	Water: 117.25	Oil:22.85	50	15	—
Lu Y. et al. [41]	2-D	Gas, oil, water	1280	Water: 631	Oil:40.81	135	1130	—
Austrheim T. [42]	3-D	Gas, oil, water	2000, 5000, 9200	Water: 0.05-1.0	Oil:0.2	21	—	—
Laleh P. [43]	3-D	Gas, oil, water	70, 700, 2760	Water: 4 (m/s)	Oil:27.3	55.4	100	VOF+DPM, $K-\epsilon$
Liang Y. [44]	3-D	Gas, oil, water	300	16, 18, 20, 22, 24	Water:64, 72, 80, 88, 96	48	—	VOF+RNG, K-ϵ
Zhang X. et al. [35]	3-D	Oil, water	1, 2, 5, 10	—	Oil:95	default	—	
Behin J. [45]	3-D	Gas, water	atmosphere	5, 7.5, 10	Water:20	default	800	Euler-Euler, $K-\epsilon$
Kocherginsky N. et al. [37]	3-D	Oil, water	atmosphere	0.04 m/s	Oil:1, 2.5, 5, 10	default	1200	—
Abdulah R. et al. [46]	2-D	Oil, water	atmosphere	0.04 m/s	—	default	130	VOF+RNG
Huang S. [47]	2-D	Oil, water	atmosphere	2	Water:10	default	—	Euler-Euler, RSM

As shown in Table 2.1, CFD studies focus on three-phase [39–44] and two-phase flows [35, 37, 45–47]. The k-ϵ turbulence model is one of the most popular models used to simulate multiphase flow [43–45, 48]. By using the standard k-ϵ model combined with the multiphase mixing model, Yuling et al. [48] investigated the internal flow field inside a gravity separator focused on the effects of different components on internal flow fields. They analyzed the velocity and flow fields of two different inlet configurations and four different rectifiers. The simulation results show that a separator with internal structures has better separation behavior.

ANSYS Fluent provides three different models to simulate multiphase flow, which are the Mixture model, VOF model, and Euler-Euler model. Each of them is developed for modeling different multiphase situations. As listed in Table 2.1, the Euler-Euler model is the most popular for simulating oil / water multiphase flow among the study [45, 47, 49, 50]. Noroozi et al. [50] used the Euler-Euler model to study the effect of different inlet designs on oil-water separation efficiency. Four different inlet structures were simulated in the study. Pressure distribution, velocity vectors, and separation efficiency were calculated and compared for these four structures. The study showed that using a helical form of inlet structures improved the separation efficiency by approximately 10 %.

Noroozi and Hashemabadi [51] studied the effect of inlet chamber design on a deoiling hydro cyclone efficiency. Four inlet chamber configurations were investigated: exponential, conical, quadratic polynomial body profile, and a standard inlet. The algebraic slip mixture model and RSM were used to predict the multiphase flow behavior. The study shows that separation efficiency can be improved by approximately 8% by using the exponential body shape. Wilkinson et al. [52] focused on the effect of baffles on separation efficiency for a horizontal separator. The study found that a single perforated plate near the inlet improves the velocity uniformity downstream

of the baffle. Additionally, when baffles are located next to each other, two baffles provided better flow uniformity.

Frankiewicz and Lee [53] studied both steady-state and transient flow by using a standard $k - \epsilon$ turbulence model and a VOF model. They developed a user-defined function (UDF) model to simulate the actual floating location of the platform. They indicated that a suitable location of baffles is essential. If baffles are improperly located, significant interface turbulence will generate within the separator, which reduces the separation efficiency tremendously. Chen et al. [54] used mathematical models to optimize the structure of an inclined oil-water separator. A separator with a diameter/length ratio of 1/15 and 12° inclination angle was recommended.

Lian et al. [44] investigated the impact of flow rate and volume fraction on the separation efficiency of a vertical three-phase separator. The flow rate range was 16 to 24 m^3/h with fixed gas and water volume fractions, at 0.5 and 0.8, respectively. Their results showed that the gas volume fraction at the gas outlets increases with an increasing flow rate from 0.975 to 0.995. Zhou et al. [55] used CFD simulation methods to study an oil-gas separator. This study provided evidence that collision plays an essential role in the oil-gas separation process. They also modified the separator design to improve separation efficiency. Their results show that a separator with baffles placed at the entrance has a better separation efficiency than separator without baffles.

Residence time distribution (RTD) is one of the experimental methods to study flow structure [45]. However, the RTD model is not accurate enough to analyze complex flow, such as oil-water multiphase flow. To improve the design of three-phase gravity separators, Mehdi et al. [16] developed a computer code based on the evolutionary computational method to improve the design of three-phase gravity separators. The effect of separator design factors, such as separator length, diameter, water

chamber length, residence time, and surge time on separation efficiency was tested in this study. For the defined minimum separator size, simulation results showed that the minimum required residence time was the time required for the light phase to rise and separate from the heavy phase. In their study, an optimal design of a separator with a volume of approximately 18.4 m^3 was selected.

A Moving Particle Semi-Implicit (MPS) method has been used to model oil / water flow in a complex 2-D geometry separator [56]. Studies modeled two geometries, one with baffles, and the other without baffle. When oil weir height is made lower than 200 cm, the separation efficiency becomes independent of oil weir height; however, when the weir height is made greater than 350 mm, the separation efficiency becomes 100 %. The separation efficiency decreases with the increase of the vertical distance between the inlet and the initial water surface, but after 150 mm, this distance does not affect separation efficiency. A renewal rate was introduced in this study. The renewal rate is the ratio between the flow rate and the separation chamber volume. The separation efficiency decreases significantly with the increase in the renewal rate. Kyung and Moo [57] also used the MPS method to trace the oil-water interface. By comparing the simulation results with previous experimental results, they proved that this model provides an accurate prediction of interface location variations over time.

CFD simulation techniques are also used to study centrifugal separators [49,55,58, 59]. In a cylindrical cyclone separator, Liu et al. [49] used the Euler-Euler multiphase model combined with the Reynolds Stress Model (RSM) to simulate the flow field and predict separation performance. The results of this study show that increasing the flow split-ratio can greatly improve separation efficiency (flow split-ratio is defined as the ratio between the overflow liquid flow rate and the inlet liquid flow rate). A non-dimensional separation acceleration G-force (G_f) is defined in this study as the ratio between centrifugal acceleration and gravitational acceleration. The study

showed that an increase of G_f in a certain range could improve oil / water separation efficiency. However, an extremely high G_f may have the opposite effect due to the formation of emulsification. Shi et al. [59] systematically studied the influence of vortex finder designs, optimum insertion depth, and diameter of liquid / liquid cylindrical cyclone (LLCC) separator by using CFD simulations. The steady multiphase flow was modeled using a mixture model and the RNG k- ϵ model. Both numerical results and experimental results showed that the length and the shape of the vortex finder affect separation efficiency. Also, increasing the inlet velocity can improve separation. The oil droplet size has a significant impact on separation efficiency with increasing diameter of oil droplets, increasing the separation efficiency. Additionally, increasing the oil volume fraction from 10 to 30 % decreased separation efficiency.

Several studies have also used CFD methods to investigate the flow structure in pipelines, such as stratified flow or slug flow. By studying the internal flow field of the three-phase separator, Zhenlin et al. [60] found areas of no flow velocity, vortex flow, and flow "short circuit" inside the separator. These three areas reduced the time for oil droplets to stay in the separator, therefore, reduced the separation efficiency. Luo et al. [61] used the RSM model to study the impact of velocity and pressure on turbulence flow, and their simulation results indicate that the flow exhibits Rankine-Eddy flow characteristics.

2.4 Analytical Models

There are two types of analytical models for liquid / liquid separation. Empirical models are generated by investigating key factors, such as liquid physical properties, operating conditions, with an experimental process to measure a correlation between the separation efficiency and the factors [62, 63]. The disadvantage of this type of

model is that it cannot be reliably extended to applications beyond the range of the experimental studies. An experimental study by Breisig et al. [64] investigated a droplet-based liquid / liquid separation process inside a porous capillary. A new continuous microscale liquid / liquid separator was investigated and proved the possibility of scale-up for industry use. The liquid-liquid separation was conducted in microfluidic equipment, which is the combination of the droplet formation stage and phase separation stage into a single device. However, droplet formation and coalescence processes were not considered. Mathematical models are obtained by formulating differential conservation equations for both phases. The population balance model (PBE) is one of the most widely used in this type of model [65]. In the PBE model, the dispersed phase comprises discontinuous droplets evenly distributed in the continuous phase. One of the advantages of the PBE model is that it considers droplet coalescence and breakage processes [66]. Ramakrishna [67] provided a comprehensive review of PBE models. Nguemaha and Zhou [68] investigated a computational method to calculate the phase diagrams of a protein-regulator mixture separated in a liquid-liquid separator. With the development of food industry, such as protein, liquid / liquid separation studies more focus on the biomedical sector [68–72]. The main interest of these studies is to improve the separation efficiency using either improved experimental setups or chemical enhance to help the separation process.

2.5 Liquid / Liquid Coalescence

The density differences of two phases result in a slow separation of drops in a gravitational field. For an oil / water multiphase flow separation process, the main challenge is to increase droplet size. Coalescence is the main process of droplet growth, and a coalescence theory for researchers to calculate the analytical models for oil / water

separation in multiphase flow is required. The coalescence process involves interaction between droplets and the surrounding liquid, which is considered more complex than other processes, for example, the break-up process [73].

As liquid / liquid separation is caused by a buoyancy force on the less-dense droplets, the terminal velocity of oil droplets is significantly affected by droplet diameter; thus, droplet coalescence has a significant impact on separation dynamics [74]. Coalescence can be divided into three main steps [75, 76]: (i) droplets approach and collide with each other, which is called the transport step, (ii) droplets keep in contact until the films of the droplets reach a critical thickness, and (iii) the droplet's films merge into each other resulting in coalescence into a larger droplet, which is called the kinetic step [77]. Therefore, there is no sharp interfaces between oil / water face due to the complex coalescence process. Experimental studies show that the first step requires more time than the second step. This means that the coalescence time mainly depends on the droplets' transport time. Various mechanisms contribute to collisions, such as oil droplet random motion, and different rising velocities due to the different droplet diameters [78–80]. However, not every collision will result in coalescence, which is related to collision frequency and coalescence efficacy [81].

The oil / water multiphase separation process can be defined as four zones in the separator, as shown in Figure 2.4 (Redrawn from [82]): clear oil zone, sedimentation zone, dense-packed zone, and clear water zone. In the sedimentation zone, droplets of the dispersed phase (oil phase) are highly active, and the coalescence process takes place in this zone.

Gimes [83] presented a population balance model for the batch gravity separation of the oil and water multiphase system. The physical properties of bulk liquids, the phase interface, and the interface activity of phases were considered in his model. Some sub-models developed in this study are the model for interfacial coalescence;

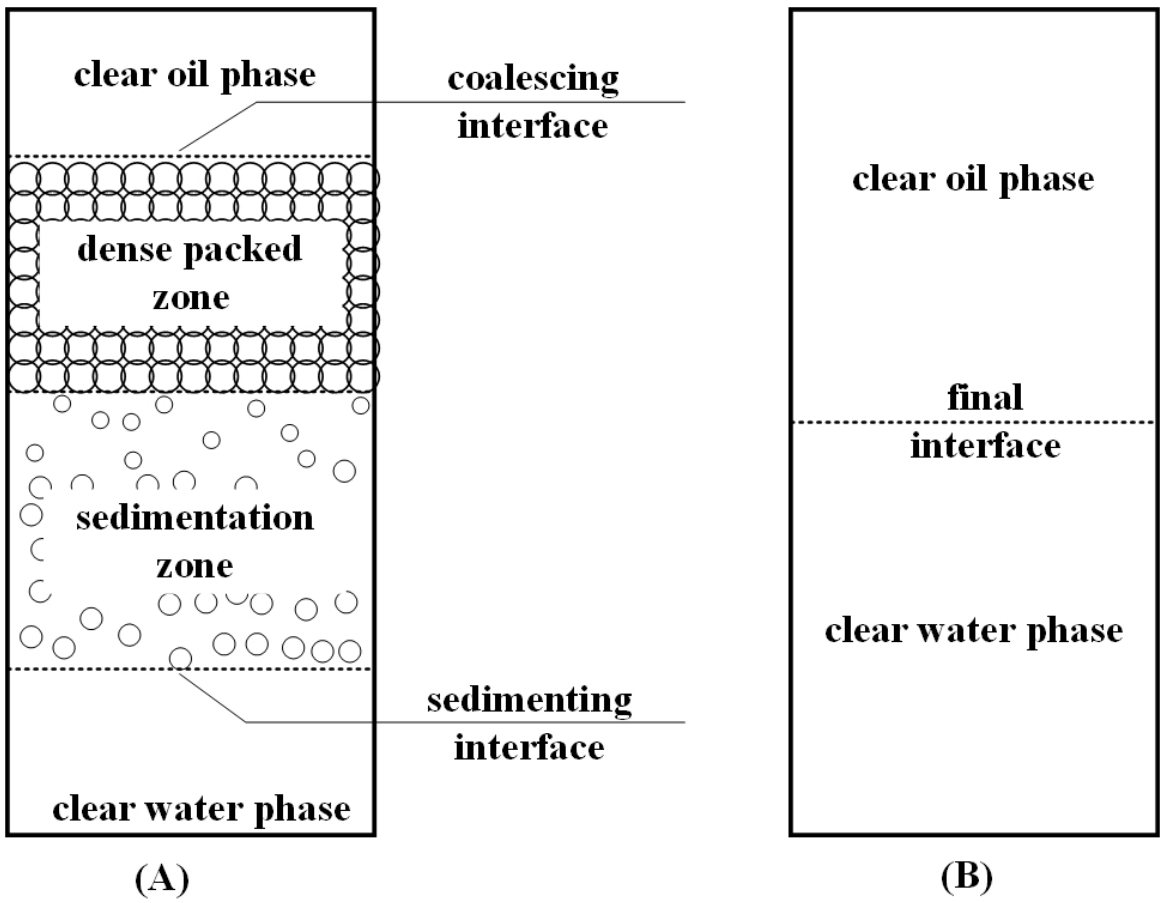

Figure 2.4: Scheme of gravity based oil-water separation

the model to predict the volume fraction of the dispersed phase-changing process at any axial position and time; the model to calculate the interface location of the resolved dispersed phase as a function of time; and the model to estimate droplet size distribution, droplet growth rate, and the standard deviation of droplet diameter. More details of these models are provided in Ref [83].

A population balance method is used by Ruiz and Padilla [84] to develop a mathematical model for steady-state (S-S) flow in a separator. The population balance method considers the droplet size distributions in its model. Their model developed an expression for the frequency of binary droplet coalescence, and the rate of growth of drops from the passive to the active interface. Results showed that coalescence frequency does not depend on droplet size, which is validated by experimental results from their previous work. One of the contributions of this study is that the model can provide an accurate prediction of the thickness of the emulsion layer.

Coalescence frequency is affected by collision frequency and coalescence efficiency, as not all collisions result in coalescence. Many papers on coalescence efficiency and collision frequency have been published, as presented in Table 2.2. Howarth [85] proposed an equation to predict droplet coalescence frequency in a homogeneous flow with uniform droplet size. Howarth assumed that most collisions result in coalescence, but stated the coalescence frequency is a function of the critical velocity of two droplets without giving a value for the critical velocity. Lehr et al. [86] developed a model to predict the critical approach velocity as an empirical relationship theory based on experimental results. The model showed that small approach velocities lead to high coalescence efficiency. An energy model, which was proposed by Howarth [87], found that most collisions cause immediate coalescence and the probability increases as the collision energy increase. Furthermore, in Sovova's model [88], the coalescence efficiency initially decreases with increasing bubble diameters, then increases with

increasing bubble diameters after a critical diameter. This critical bubble diameter is 0.005 m in their study. The reason for the trend is the model combined the surface merging model and the interfacial energy model. Therefore, the coalescence efficiency decreases for small bubbles and then increases with the diameter of the bubble.

Another model, developed by Chesters [89], separated the collisions in a turbulent flow into viscous and inertial collisions. The reason for considering inertial collisions was that he found the inertial force between two particles is greater than the external force exerted by the flow. The film drainage model determines coalescence efficiency based on the contact time and the drainage time of two droplets [89–93]. Drainage time is the time required for the film of two drops to be thinned to a critical thickness. Various factors contribute to the drainage time, such as the shape of droplets, and whether the droplet shape is deformable or non-deformable.

Modeling bubble or drop coalescence is very complex, and there are no satisfactory models that represent all mechanisms or are applicable to a wide range of conditions. Some models show that coalescence efficiency decreases with increasing bubble size [86, 89, 94]. Another model presents that the coalescence efficiency decreases with increasing bubble size until it reaches the critical droplet diameter, then increases with droplet diameter [88]. In general, these models describe the coalescence behavior qualitatively, but not quantitatively because they do not account for all the relevant parameters due to the complexity of mechanisms and the coalescence process. Most of the previous models are developed for bubbles, and only a limited quantity of studies [85, 88, 93] have been developed to model droplet coalescence. If the viscosity term is ignored, in the bubble coalescence, then under suitable transformations of the variables, the Weber number and radius ratios are canceled from the governing equations, and a universal solution can be obtained. With this simplification, the bubble coalescence process model becomes less complex compared to droplet coalescence.

Table 2.2: A summary of the coalescence frequency models

Type	Authors	Theory/Model	Drop/Bubble
Coalescence Efficiency	Howarth [85] 1964	Critical velocity model	Drop
	Lehr, et al. [86] 2002		Bubble
	Howarth [87] 1967	Interfacial energy model	Bubble
	Sovova [88] 1981		Drop
	Alopaeus, et al. [90] 2002		Bubble
	Chesters [89] 1991	Surface merging model	Bubble
	Vaughn, Slattery, [91] 1995		Bubble
	Podgorska, Baldyga [92] 2001		Bubble
	Liu, Li [93] 1999		Drop
Collision Frequency	Prince, Blance [94] 1990	Buoyancy	Bubble
	Wang et al., [95] 2005	Turbulence fluctuations	Bubble

2.6 Dimensionless Method in Separator Design

Historically, the field of dynamics of the separation process has been modeled using complex analytical and numerical models, such as droplet coalescence models. There is only a few research describe the dimensionless group effect on the separation process. Jeelani et al. [28] developed a model that describes the kinetics of the Reynolds number to estimate the separated oil volume from a continuous separation process. The separator design criterion is extended by using the residence time distribution method, which predicts the hydrodynamics and mixing conditions in the continuous phase [96]. Another model of the separator is developed to estimate the steady-state flows and separator behavior with various operating conditions [97]. These models did not consider variations of reservoir conditions in the field. Even within one reservoir, the amount of oil volume fraction changes during a reservoir's lifetime. These variations exert a potential effect on oil / water separation efficiency, which in turn affects the performance of the separator. Therefore, fundamental research is needed to study the relationship between the geometric designs of a separator and the physical properties of fluids.

2.7 Summary

In conclusion, it is evident in the literature that although separation technologies are mature, there is still room for improvement in separator design to improve operating efficiency. In addition, improved modeling, either analytical or numerical, can allow separation processes to be developed or improved for previously unstudied operating conditions such as those found in subsea installations.

Numerical modeling is a viable approach but remains computationally expensive, and only some programs are able to model two-phase flows. None of the available

programs provide a full model of the coalescence process.

Analytical models are necessity relatively simplified due to the overall complexity of the separation process and the flows within a separator. As with numerical models, mathematical models are significantly limited in their ability to model the coalescence process. Based on previous research studies, the understanding of droplet coalescence efficiency and the collision frequency is still limited due to its complexity, which involves viscosity. Therefore, only limited studies have been conducted on this topic.

Based on the literature review, it is determined that there is room for improvement in the understanding of separator design and, in particular, the specific effects of operating parameters on the physical design of separator technology. This thesis addresses these issues by first developing high-level semi-analytical models of droplet coalescence to guide separator design. This is then supplemented with the development of simple physical models that can be tested at normal pressures and temperatures in order to validate or calibrate the analytical and numerical models. In addition, developing 2-D and 3-D numerical models that can be used to simulate the high-pressure subsea separation process. The additional work involved using other software to develop 3-D models. These were compared to the original simulations and to physical models. Finally, to develop a method of correlation, based on dimensional analysis, to allow CFD results calibrated with the lab-scale experimental data, to be scaled up to prototype behavior.

The specific research objectives developed for this study is to explore methods of numerical and analytical modeling, including dimensional analysis, that can be applied to separators to better understand the effects of operating parameters such as temperature, pressure, mixture ratios and flow velocity on the design parameters and physical size requirements for flow through separators.

Chapter 3

Development of Semi - Analytical Models

In this section, the separation process for a multiphase separator is modeled. This mathematical method is used to optimize separator design parameters such as length and width, based on Stokes law.

3.1 Mathematical Design Model for Separators

As shown in Figure 3.1, ideal operating conditions allow mixture has enough residence time to allow an oil droplet to travel in a separator through the longest path, which is the distance between the bottom of the separator and the oil / water interface. Therefore, modeling the oil separation hydrodynamics based on the separation of this longest path droplet would ensure the removal of all other droplets with the same or larger diameter.

This process assumes that Stokes law governs the rising vertical velocity (v_v) of the traversing oil droplet on its path to the oil / water interface, and the inlet flow rate

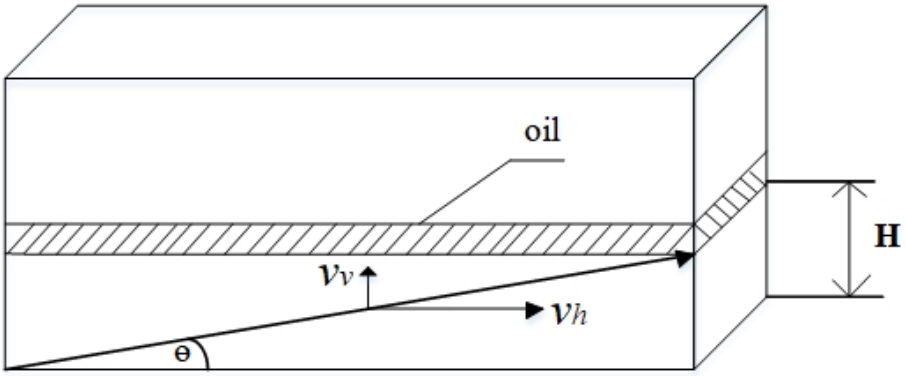

Figure 3.1: Oil separation process under ideal operating conditions

governs the horizontal velocity (v_h). The vertical velocity is estimated from Stokes law by the equation:

$$v_v = \frac{2}{9} \cdot \frac{(\rho_w - \rho_o) \cdot g \cdot r^2}{\mu_w} \tag{3.1}$$

where, ρ_w, and ρ_o are the density of water and oil, respectively, r is the droplet diameter, and μ_w is the water viscosity.

The horizontal velocity component is estimated from the residence time as $V_h = L/\tau$, where L is the length of the separator and $\tau = V_{total}/q_{in}$ is the residence time, V_{total} is the volume of the separator, q_{in} is inlet flow rate of the multiphase fluid. Therefore, the level of the oil / water interface (H) is determined from

$$A_c = \frac{q_{in}}{v_h} \tag{3.2}$$

$$H = v_v \cdot \frac{L}{v_h} \tag{3.3}$$

where A_c is the cross-sectional area of the multiphase flow, θ is the angle which defines the longest droplet path to the level oil-water interface (H), which can be estimated from

$$\theta = arctan(\frac{v_v}{v_h}) \tag{3.4}$$

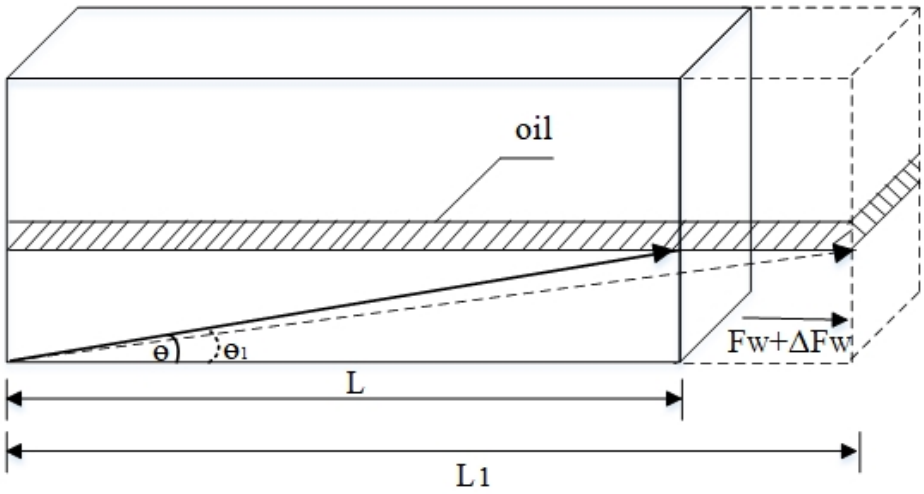

Figure 3.2: Oil separation process under high flow rate

The design parameters W, H, L of the water phase will have ideal operating condition values. In reality, most of the time, separators cannot reach a complete separation; therefore, we have to assume that the water outlet F_w will increase by a value of ΔF as a result of a corresponding un-separated oil. This results in an angle change of the longest path of a traversing oil droplet from θ to θ_1, where $\theta_1 < \theta$. Figure 3.2 demonstrates that extending the length of the separator to $L_1 = L + \Delta L$ will result in complete separation. Assuming that the design parameters A_c, H, θ remain the same, as shown in Figure 3.2, then:

$$\theta_1 = arctan(\frac{v_v + \delta v_v}{v_h}) \tag{3.5}$$

Additionally, another simplification assumption has to be made in order to estimate the volume fraction of the unseparated oil, ε. As shown in Figure 3.3, we assume that the unseparated oil droplets in the water phase form a "tail" extending into the virtual separator extension, also shown by the dashed line that unseparated oil exists within the water. However, the accuracy of this assumption is dependent on the geometry of the separator. Based on this assumption, region V_3 represents the

volume of the unseparated oil V_2. Figure 3.3 shows that region V_3 is the difference between the oil volume in the virtual separator (represented by $V_t = V_1 + V_2$), and the oil volume in the actual separator (V_1). The volume $V_1 + V_2$ can be calculated as the difference between the volume of the rectangular segment defined by parameters. L_1, W, H:

$$L_1 = \frac{L}{v_h} \cdot cot(arc(tan(\frac{v_v + \delta v_v}{v_h}))) \tag{3.6}$$

where

$$V_t = V_1 + V_2 = \frac{1}{2} \cdot L_1 \cdot H \cdot W \tag{3.7}$$

Furthermore, V_1 is the volume of the rectangular segment parameter represented by h_1, W, and L,

$$V_1 = \frac{1}{2} \cdot (2 \cdot v_v \cdot \frac{L}{v_h} - h_1) \cdot L \cdot W \tag{3.8}$$

$$V_2 = \frac{1}{2} \cdot (2 \cdot v_v \cdot \frac{L}{v_h} - h_1) \cdot (L_1 - L) \cdot W \tag{3.9}$$

where the virtual oil / water interface height h_1 is defined by the equation:

$$h_1 = L \cdot tan\theta_1 \tag{3.10}$$

Consequently, one can estimate the unseparated ε from the equation:

$$\varepsilon = \begin{cases} V_2/(V_1 + V_2), & (L_1 > L) \\ 0, & (else) \end{cases} \tag{3.11}$$

Having estimated the unseparated oil fluid volume fraction ε, we can calculate the separated and unseparated volumetric flow components of the fluid F_{h_1} standing for

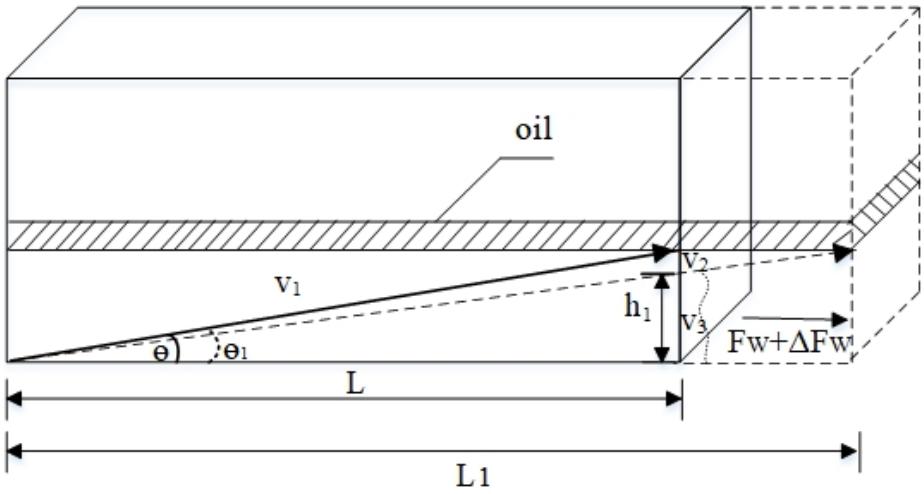

Figure 3.3: Unseparated oil under high flow rate

the separated oil and F_{h_2} standing for the unseparated oil,

$$F_{h_1} = \varepsilon \cdot v_o \cdot F_{in} \tag{3.12}$$

$$F_{h_2} = (1 - \varepsilon) \cdot v_o \cdot F_{in} \tag{3.13}$$

$$F_{w_{out}} = F_{h_2} + F_{in} \cdot v_w \tag{3.14}$$

$$\frac{dv_w}{dt} = F_{in} - F_{w_{out}} - F_{h_1} \tag{3.15}$$

where, v_o, v_w is inlet volume fraction of oil and water, respectively, F_{in} is inlet flow rate, v_w is water phase volume, and $F_{w_{out}}$ is water outlet volumetric outflow.

The analytical model to predict the separation efficiency is presented above. However, this model has some limitations based on the following simplified assumptions made in this separation process model:

1. The separation processes are isothermal in all phases of the separator at all operating temperatures.

2. The oil droplets in the water phase have a uniform droplet size distribution with

a diameter $d = 50\ \mu m$.

3. The rising velocities of oil droplets obey Stokes law.

3.2 Interface Tracking Model

A model was developed to track the oil / water interface in a batch situation where a tank without inlets or outlets had a uniform mixture with a specific oil volume fraction at the start. The motion equation for an oil droplet surrounded by water is

$$M\frac{\partial v_v}{\partial t} = F_b - G_f - F_d \tag{3.16}$$

where M is the mass of the droplet, F_b is the buoyancy on the droplet, and F_d is the viscous drag force on the droplet. The parameters are

$$M = \rho_o \cdot \frac{4}{3} \cdot [\frac{d}{2}]^3 \tag{3.17}$$

$$F_b - G_f = [\rho_w - \rho_o] \cdot g \cdot \frac{4}{3} \cdot [\frac{d}{2}]^3 \tag{3.18}$$

$$F_d = C_D \cdot \pi \cdot [\frac{d}{2}]^2 \cdot \rho_w \cdot \frac{U^2}{2} \tag{3.19}$$

It is assumed that the droplet is moving at terminal speed v_t:

$$v_t = \sqrt{\frac{(\rho_w - \rho_o) \cdot g \cdot \frac{8}{3} \cdot (\frac{d}{2})^3}{C_D \cdot \rho_w}} \tag{3.20}$$

The tank is divided into horizontal slices with thickness h', and cross-sectional area A, with the volume of a slice being $A \cdot h'$.

At any time i, there is a volumetric flow of oil into a slice from the slice below and a volumetric flow of oil out of the slice into the slice above. The net volume of

oil moved is

$$\Delta V = v_{t(i-1)} \cdot \Delta t \cdot f_{(i-1)} \cdot A \cdot h' - v_{t(i)} \cdot \Delta t \cdot f_i \cdot A \cdot h' \tag{3.21}$$

The change in the volume fraction of oil is

$$\Delta f_i = \frac{\Delta V}{A \cdot h'} \tag{3.22}$$

A slice where the volume fraction of oil above it is equal to 1 and the volume fraction of oil below this slice is equal to the original fraction f_{ori}. The volume of oil into the slice from the one below is

$$\Delta V_M = v_t \cdot A \cdot f_{ori} \cdot \Delta t \tag{3.23}$$

The volume that needs to be filled with oil is

$$\Delta V_N = (1 - f_{ori}) \cdot A \cdot h' \tag{3.24}$$

The moving speed of the interface is

$$v' = \frac{h'}{\Delta t} = \frac{(v_t f_{ori})}{1 - f_{ori}} \tag{3.25}$$

The location of the interface is

$$z = h - v' \cdot t \tag{3.26}$$

The time to steady state is

$$\begin{aligned} t_{s-s} &= f_{ori} \cdot \frac{h}{v'} \\ &= \frac{f_{ori} \cdot h}{(v_{s-s} \cdot f_{ori})/(1 - f_{ori})} \\ &= \frac{h}{v_{s-s} \cdot (1 - f_{ori})} \end{aligned} \tag{3.27}$$

For a steady state case, $F_b - G_f = F_d$, and $v_v = v_{s-s}$

$$(\rho_w - \rho_o) \cdot g \cdot \frac{4}{3}[\frac{d}{2}]^3 = C_D \cdot \pi \cdot [\frac{d}{2}]^2 \cdot \rho_w \cdot \frac{v_{s-s}^2}{2} \tag{3.28}$$

For low Reynolds number flow around a droplet

$$\begin{aligned} C_D &= \frac{24}{Re} \\ &= \frac{\rho_w \cdot v_{s-s} \cdot d}{\mu_w} \end{aligned} \tag{3.29}$$

Substitution into the L = W equation provides

$$v_{s-s} = \frac{(\rho_w - \rho_o) \cdot g}{18 \cdot \mu_w} \cdot d^2 \tag{3.30}$$

The interface equations becomes

$$v' = \frac{(\rho_w - \rho_o) \cdot g}{18 \cdot \mu_w} \cdot d^2 \cdot \frac{f_o}{1 - f_o} \tag{3.31}$$

$$t_{s-s} = \frac{h \cdot (1 - f_{ori}) \cdot (18\mu_w)}{(\rho_w - \rho_o) \cdot g \cdot d^2} \tag{3.32}$$

Note that v' increases with increasing $(\rho_w - \rho_o)$, but t_{s-s} decreases as f_{ori} increases. Thus one might expect the effective $(\rho_w - \rho_o)$ to decrease. In addition, v' decreases with increasing μ_w, however, t_{s-s} increases. As f_{ori} increases, one might expect the

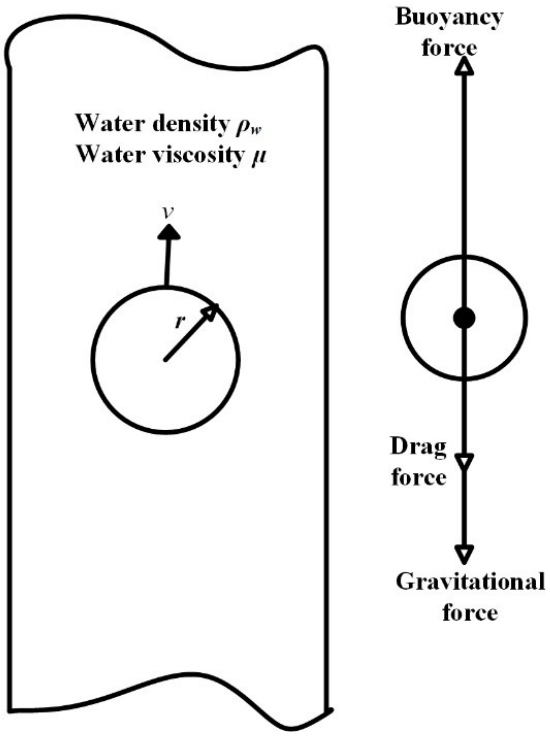

Figure 3.4: Force balance on a spherical oil droplet rising in the water phase

effective μ_w to increase.

3.3 Terminal Velocity Theory

In this section, the force balance for one droplet is analyzed, and an analytical model is developed to predict the separation process. As discussed in the previous section (page 34, section 3.1), the oil / water separation process occurs under a low Reynolds number flow in which is assumed to be laminar flow. In an oil / water flow system, three forces determine the oil rising velocity, drag force, gravitational force, and buoyancy force, as shown in Figure 3.4. In small Reynolds number flow, the drag force is predominantly from viscous forces, and these forces are proportional to viscosity. Therefore,

$$F_d \propto \mu \tag{3.33}$$

The drag force F_d on a sphere is described by Stokes' law with the following assumptions:(a) sphere rigid, (b) it is an infinite medium, (c) there is no slip at the surface,(d) inertial forces are insignificant. Therefore, the governing equation becomes

$$\frac{1}{\rho}\frac{\partial p}{\partial x} = \frac{\mu}{\rho} \cdot \frac{\partial u^2}{\partial x \partial x} \tag{3.34}$$

Here, dimensionless characteristic velocity u_0 and length are defined as $Re = \rho \cdot u \cdot l/\mu$, $\mu = \rho \cdot v$, u stands for the mean velocity.

For a spherical oil droplet, Eq. 3.34 has an analytical solution based on spherical coordinates. Assuming the oil droplet has radius R, we have:

$$\begin{aligned} P &= P_0 - \frac{3}{2} \cdot (\frac{\mu u}{R}) \cdot (\frac{R}{r})^2 \cdot cos\theta \\ u_\theta &= u \cdot sin\theta[1 - \frac{3}{4} \cdot (\frac{R}{r}) - \frac{1}{4} \cdot (\frac{R}{r})^3] \\ u_r &= u \cdot cos\theta[1 - \frac{3}{2} \cdot (\frac{R}{r}) + \frac{1}{2} \cdot (\frac{R}{r})^3] \end{aligned} \tag{3.35}$$

Force balance is used on one oil droplet to solve the above equation. Three forces are acting on one droplet, F_B, F_D, and F_g,

$$\begin{aligned} F_b - F_d - F_g &= m\frac{du}{dt}, \\ \rho_w \cdot V - C_D \cdot \frac{1}{2} \cdot \rho_w \cdot u^2 \cdot A_p - \rho_{oil} \cdot V \cdot g &= \rho_o \cdot V \cdot \frac{du}{dt}, \end{aligned} \tag{3.36}$$

where C_D is controlled by droplet velocity. To solve Eq.3.36, we first assume the motion of the oil drop is in the laminar regime. Therefore, C_D is equals to $C_D = 24/Re$, the terminal velocity is determined by Stokes's law [98].

$$u = \frac{2}{9} \cdot \frac{g \cdot r^2}{\mu}(\rho_w - \rho_o) \tag{3.37}$$

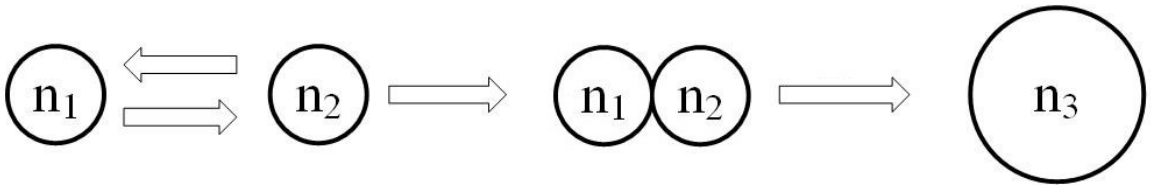

Figure 3.5: Schematic of oil droplets coalescence process

As presented in Eq. 3.37, the rising velocity of a droplet is directly proportional to the size of the droplet. Droplets are easily deformed during the separation process. The deformation of the droplet affects the droplet diameter. However, for small droplets (150 μm < d < 500 μm), it is assumed that the deformation effect on rising velocity is minimal. The same assumption has been used in many previous studies. Estrade et al. [99] used the same assumption to experimentally investigate the binary droplet collision with an error within 10 %. The same assumption was also used by Wang et al. [100] to develop an analytical model between coalescence and droplet size. More studies can be found in the review paper of Tom et al. [101]. As illustrated in Figure 3.5, droplet coalescence includes three main steps: (i) the transport step where droplets approach each other, (ii) droplets keep in contact until the films of the droplets reach a critical thickness, and (iii) the kinetic step where droplets merge into larger droplets [102]. Several factors affect this coalescence process, including the number of droplet collisions, relative velocities of droplets, size of droplets, and viscosity of the fluid.

3.4 Mass Balance for Coalesced Drops

Brownian collisions and gravity differences between oil and water contribute to the movement of oil droplets, resulting in the coalescence of oil droplets. In the coalescence process, droplets initially undergo binary coalescence, resulting in an increase in the average droplet diameter with time, and then undergo further coalescence be-

tween larger droplets until they reach the interface layer, and separate from the water phase. Therefore, for more accurate predictions of liquid / liquid separation, droplet coalescence needs to be represented.

In the development of the droplet coalescence model, it is assumed that the oil droplets initially have the same diameter and are equally distributed in the water phase. This condition is difficult to be fully achieved in fluid mixtures. However, a previous study conducted by John et al. [103] found that over 90 percent of droplets are distributed around a mean droplet size, with an average deviation of 3.6 %. In the study, video microscope was used to measure water droplet size in an oil phase with various mixing conditions. Thus, in this paper, it is assumed that droplets have the same initial diameter. Therefore, a new correlation for coalescence can be developed. The diameter of oil droplets after the first coalescence is calculated in the following way:

$$2 \cdot V_n \cdot \rho = V_{n+1} \cdot \rho \tag{3.38}$$

$$2 \cdot \frac{4}{3}\pi \cdot {r^3}_n \cdot \rho = \frac{4}{3}\pi \cdot {r^3}_{n+1} \cdot \rho \tag{3.39}$$

where V_{n-1} and V_n are the volumes of the droplets before and after coalescence, respectively, and the variable n denotes the times of sequential coalescence occurrences. The diameter of oil droplets after coalescence is

$$r_{n+1} = \sqrt[3]{2} \cdot r_n \tag{3.40}$$

Therefore, the rising velocity for the droplets is

$$v_{n+1} = \frac{2}{9}\frac{(\rho_w - \rho_o) \cdot {r^2}_{n+1}}{\mu_w} \cdot \rho = \sqrt[3]{4} \cdot v_n \tag{3.41}$$

The rising distance is

$$Y_r = v_{n+1} \cdot t \tag{3.42}$$

Substituting Eq.3.37 and Eq. 3.41 into Eq. 3.42, Y_r becomes

$$Y_r = \frac{2^{5/3}}{9} \frac{(\rho_w - \rho_o) \cdot {r^2}_n}{\mu_w} \cdot g \cdot t \tag{3.43}$$

By assuming that coalescence time is a function of binary droplet coalescence steps per volume, Eqs. 3.40 - 3.42 are used to determine the diameter of droplets after coalescence, the terminal rising velocity of droplets after coalescence, and the rising distance of droplets after coalescence, respectively. The time period of one binary droplet coalescence step includes the time needed for the droplets to approach each other, connect, and then merge to one droplet. A correlation was developed to predict the time-period for each coalescence step for several oil / water fractions and initial droplet diameters based on numerical simulations of evenly-dispersed equivalent-diameter oil droplets in water.

3.5 Dimensional Analysis of Multiphase Separation

The Buckingham Π Theorem [104], using dimensionless Π terms, is selected for this analysis to determine a relationship between the separator geometry and operating conditions effect on separation efficiency.

The theoretical minimum length is that required to achieve the maximum separation efficiency, the required horizontal length of a separator that enables the smallest droplets to separate from the continuous phase based on their rising velocity, which is estimated using Stokes law. The theoretical minimum length of a separator (x)

Table 3.1: Description of the various parameters in fundamental dimensions.

Variable	Description	SI units	Dimensions
x	Separator horizontal length	m	L
h	Separator vertical height	m	L
v	Fluid velocity	m/s	LT^{-1}
ρ_m	Density of mixture	kg/m^3	ML^{-3}
μ_m	Dynamic viscosity of mixture	Pa $\cdot s$	$ML^{-1}T^{-1}$
$\sigma_{o/w}$	Surface tension between oil and water	N/m	MT^{-2}
P	Operating pressure	Pa	$ML^{-1}T^{-2}$

depends on the vertical height of a separator (h), fluid velocity (v), viscosity (μ_m), multiphase fluid density (ρ_m), fluid surface tension between two phases ($\sigma_{o/w}$), and operating pressure (P) in the following way,

$$x = f(h, v, \mu_m, \rho_m, \sigma_{o/w}, P) \tag{3.44}$$

Each of the identified parameters is presented by a set of fundamental dimensions of mass (M), length (L), and time (T) in Table 3.1. Based on the Buckingham Π Theorem [104], four dimensionless Π terms are determined, as presented in Table 3.2. The resulting relationship based on this analysis is as follows:

$$\Pi_1 = \phi(\Pi_2, \Pi_3, \Pi_4) \tag{3.45}$$

or

$$\frac{x}{h} = C \cdot \left(\frac{h \cdot v \cdot \rho_m}{\mu}\right)^{n_1} \cdot \left(\frac{P}{v^2 \cdot \rho_m}\right)^{n_2} \cdot \left(\frac{h \cdot v^2 \cdot \rho_m}{\sigma_{o/w}}\right)^{n_3} \tag{3.46}$$

Here, assume mixture is imcompressible and isotropic fluid, thus, the mixture density

Table 3.2: Dimensionless Π terms.

Π Terms	Dimensionless Group	Name
Π_1	$\frac{x}{h}$	Separator length/height ratio
Π_2	$\frac{h \cdot v \cdot \rho_m}{\mu}$	Reynolds number
Π_3	$\frac{P}{\rho_m \cdot v^2}$	Euler number
Π_4	$\frac{h \cdot v^2 \cdot \rho_m}{\sigma_{o/w}}$	Weber number

and the mixture viscosity are defined as

$$\rho_m = \sum_{k=1}^{n} \alpha_k \rho_k \tag{3.47}$$

$$\mu_m = \sum_{k=1}^{n} \varepsilon_k \mu_k \tag{3.48}$$

where k represents phase k, ε is volume fraction. Changing the volume fraction of each phase results in the change of mixture density and viscosity. According to Sydney's [105] study, the relation between the temperature T and the surface tension is linear through a relatively small temperature range, 20 - 65 $^{\circ}C$. Therefore, this linear relationship between surface tension and temperature is applied in this study.

Chapter 4

Development of Experimental Study

This chapter describes two experimental setups designed to test CFD models at the droplet and prototype tank levels. The motivation of conducting both batch and continuous separation experiments in this chapter is to use batch simulation results to provide a fundamental check on CFD. Also, test batch runs are used to validate the previously developed analytical models to make them better for the initial design. The comparison between CFD and experimental results is then carried forward to a continuous flow scenario, which more realistically approximates real-world separation equipment and provides the basis for extrapolation to the subsea high-pressure separator modeling.

4.1 Batch Separation

4.1.1 Experimental setup design

This section presents an experimental setup to investigate the droplet level dynamics of liquid / liquid separation. A series of experiments on oil / water batch separation was conducted in a transparent vessel with a high-resolution camera to record the separation process. A mixture was prepared with a volume ratio of water to oil of 4:1. The water phase, with a volume of 400 ml, was measured by two volumetric flasks with a capacity of 200 ml, with ± 0.1 ml accuracy. The oil phase, with a volume of 100 ml, was measured via a graduated cylinder with an accuracy of ± 1.0 ml. To generate a homogeneous oil / water mixture, the two phases were mixed in a transparent vessel with a capacity of 600 ml (± 3.0 ml), and a height of 90 mm (± 0.5 mm). The mixture was stirred at a speed of 1100 rpm using a magnetic stirrer for 30 min. This procedure generates a homogeneous oil / water mixture with a mean oil droplet diameter of approximately 200 μm [106–108]. The temperature was maintained at 20 °C for all experiments. The high-resolution camera was placed in front of the separator (which is a transparent vessel) to record the separation process. To increase the visual observation of the oil / water separation process, a red dye water tracker, which can only be dissolved in water, was added into the water. Also, a measuring scale was placed at the surface of the batch separator with a precision of 1 x 10^{-4} m (0.1 mm) to measure the thickness of the oil layer.

A schematic of the experimental setup for liquid / liquid separation is illustrated in Figure 4.1. The thickness of the oil layer (Y_o) was recorded and measured every 30 s during the batch separation process. This thickness is the distance from the top of the separated oil phase to the top of the interface layer. The variable Yo is used to present the smallest oil droplet rising distance overtime. A normalized thickness (Y')

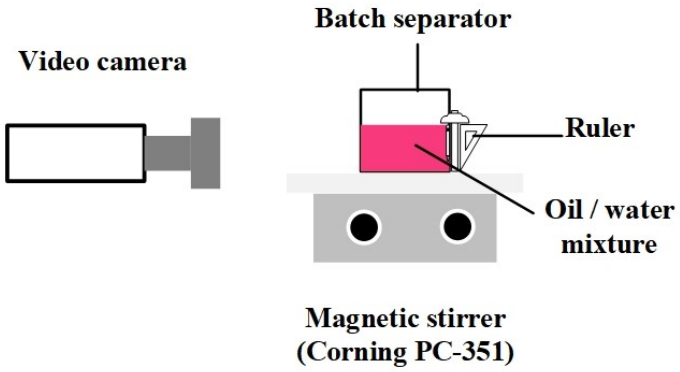

Figure 4.1: Schematic diagram of the experimental setup for liquid / liquid separation

is defined to clearly present the comparison of experimental data with the numerical simulation predictions,

$$Y' = Y_o / Y_{total} \tag{4.1}$$

where Y_{total} represents the total height of the liquid in the separator.

4.1.2 Uncertainty for batch separation setup

The batch separation process is presented in terms of the formation of the oil layer, the thickness of which varies over time. The primary sources of uncertainty in this experiment were from the volumetric flasks, the graduated cylinder, and the ruler. According to the Kline and McClintock method [109], the uncertainty equation to calculate the thickness of the oil layer is:

$$E = \frac{\sigma_R}{E_{Y'_{oil}}} = [\frac{\delta Y'_{oil}}{Y'_{oil}}^2 + \frac{\delta Y_{total}}{Y_{total}}^2]^{\frac{1}{2}} \tag{4.2}$$

where, Y', Y_{total} represents the thickness of the oil layer and the total thickness of the mixture, respectively. Based on Eq. 4.2, the total uncertainty for batch separation setup is $\pm$ 1.95 %.

4.2 Continuous Separation

In this section, the experimental setup for the continuous separation study is presented. First, an industrial scale separator was designed. Second, an experimental loop was built to conduct a continuous separation investigation.

4.2.1 Separator design theory and steps

A gravity-based separator is designed using the oil droplet rising velocity based on Stokes' Law. The separator sizes are calculated based on the maximum time needed for an oil droplet to rise from the inlet to the oil outlet. There are four main factors that need to be considered in terms of designing a separator: 1) Operating temperature. High temperatures have two effects on the separation process. High temperatures reduce the viscosity of the oil. Lower viscosity facilitates the oil / water separation processes by reducing the drag force. Higher temperatures reduce the specific gravity of oil, which further benefits the separation process. 2) Operating pressure. The operating pressure directly determines which type of material to choose for separator, along with the auxiliary equipment. Pressure also affects fluid physical properties, such as density and viscosity. 3) Residence time. A certain minimum residence time must be provided to achieve good separation efficiency. 4) Separator internal structures. Internal components inside the separator reduce the inlet velocity and increase the residence time; therefore, they need to be considered when designing a separator. For instance, important internal components include inlet distributors, internal baffles, and a vortex breaker at the outlet.

The first step for separator design is to calculate the vertical velocity of droplets. From Eq. 3.37, an oil droplet vertical velocity from the bottom of a separator to the surface is $v_v = u$. Also, according to API, horizontal velocity (v_h) is recommended

Table 4.1: Physical Properties of Fluids

Fluids	Abbreviation	Value	Unit
Temperature	T	20	°C
Gravitational acceleration	g	9.81	m/s^2
Water density	ρ_w	992	kg/m^3
Oil density	ρ_0	872	kg/m^3
Dynamic viscosity	μ	0.0013	$N/m^2 \cdot s$

to be 15 times greater than the vertical velocity, or 0.01524 m/s, whichever is the smallest velocity to maintain a laminar flow condition.

The next step is to calculate the separator size. The vertical and horizontal velocities are represented by,

$$v_v = \frac{Q_d}{A_h} \tag{4.3}$$

$$v_h = \frac{Q_d}{A_c} \tag{4.4}$$

where, the Q_d is the designed flow rate in m^3/s, A_h is the separator horizontal area in m^2, and the A_c is the separator cross-sectional area in m^2. Based on oil droplets in Stokes' law, the oil rising velocity, vertical velocity, and the horizontal velocity are used to calculate A_h and A_c, which provides the designed size for the separator. The values of physical properties for the fluids and other required parameters are listed in Table 4.1. According to API, the ratio of length to width should be set to at least 5, and the ratio of depth to width should be set to 0.5 (must be between 0.3 and 0.5).

Based on Eq.(4.3) and Eq.(4.4), for a maximum inlet flow rate of 1.02 m^3/h according the pumps capacity, and a minimum required separation time is 400 s, an ideal separator should be designed with dimensions of 1.8 m x 0.25 m x 0.15 m (length x width x depth). To account for realistic operations, the design must incorporate a

higher capacity with a factor of 1.5 to insure more complete separation.

4.2.2 Continuous separation loop design

Experimental investigations of continuous separation of oil / water were performed in a flow loop, as shown in Figures 4.2 and 4.3. Both oil and water were transferred from the storage tanks to the test section with a pump that connected to 1-inch PVC pipe supply lines. Oil and water entered the test section from the two pipes via a tee-junction. An inline mixer is located in front of the inlet to further mix oil / water. This inline mixer has 12 blades, which is designed to mix immersible liquids with low Reynolds number ($50 < \mathrm{Re} < 1000$) to generate a homogeneous mixture with isotropic droplet size distribution. A flow-meter with a maximum capacity of 2.25 m^3/h was located on each of the flow lines (water and oil). A pressure sensor was attached to the test section. After the pumps, each fluid had a bypass pipe to control the flow rate in the mainline. The mixed oil / water fluid then ran into the separator tank, where the oil and water were separated.

The separator tank had a length of 2.28 m (90 inches) and a width and height of 0.3556 m (14 inches). Three baffles with different functions were placed in the separator. The first baffle, called the flow spreading baffle, was 0.127 m (5 inches) from the inlet and was used to reduce the inlet flow rate. The reduction of the inlet flow rate is important because it is directly related to the oil rising time, which will affect the separation efficiency. The space from the inlet wall to the first baffle is defined as Zone 1.

The second baffle was located 1.778 m (70 inches) from the first baffle, with a height of 0.1778 m (7 inches). This baffle determines the oil / water main separation range, defined as Zone 2. The third baffle was located 0.254 m (10 inches) from the end of the separator and was used to further separate oil in order to comply with

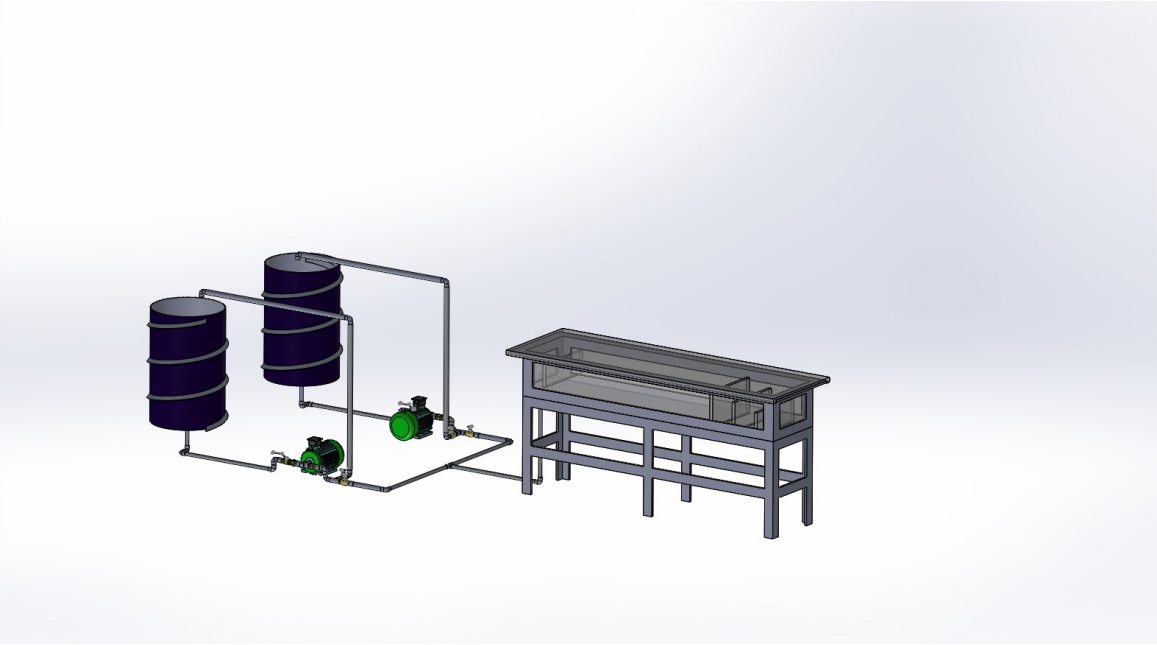

Figure 4.2: 3-D Flow Loop

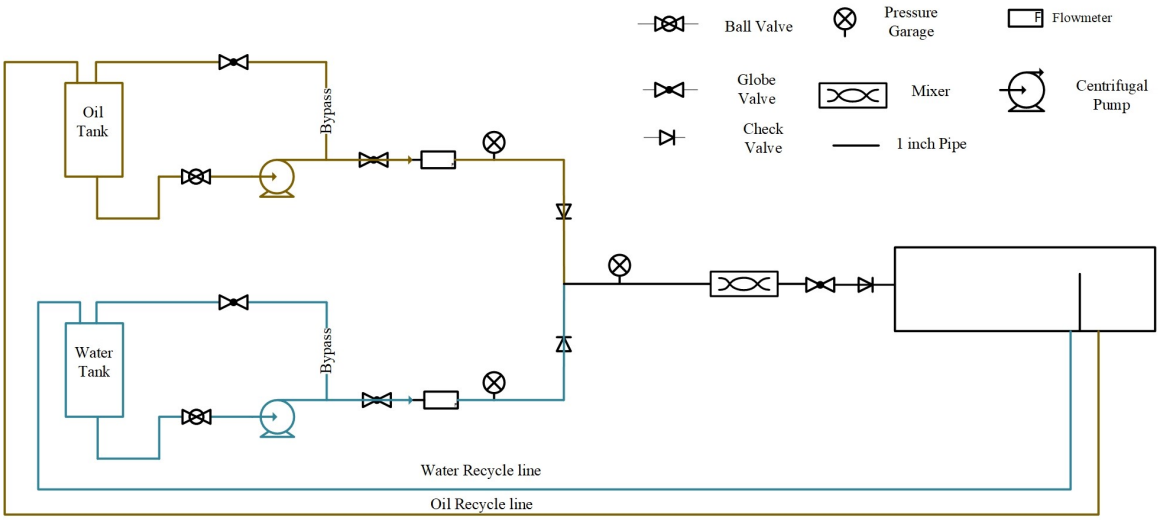

Figure 4.3: Schematic diagram of the oil / water separation flow loop

Table 4.2: Oil and Water Properties

Parameters	Unit	Mineral oil	Water
Density	kg/m^3	872	992
Viscosity (@ 40°C)	cSt	15	0.6579
Interfacial tension	mN/m	20.1	

recycling standards. The area between the third baffle and the end of the separator is defined as Zone 3. Each Zone has different functions. Zone 1 is designed to reduce the inlet velocity to better mix oil / water mixture; Zone 2 is the main separation section, which is used to investigate the separation process. The simulation model share the same geometry design as Zone 2, which will be shown in Chapter 5, Figure 5.1 B. The 3D views of this separator are shown in Figure 4.4. The physical properties for the fluids and parameters are presented in Table 4.2.

Main measurement equipment

- **Centrifugal Separator** A centrifugal separator was used to further separate samples, and to further analyze the oil / water separation efficiency. The module information of the centrifugal separator is listed in Table 4.3. The post-treatment for the samples provided information that is used in the uncertainty analysis of the separation efficiency.

  The relative centrifugal force (RCF) is given in multiples of earth gravity (g). It is a dimensionless number that allows comparison between the efficiency of separation of various instruments, since it is independent of the instrument used. The only values entered in the equation are the radius and speed of centrifugation:

  $$RCF = 11.18 \times (\frac{n}{1000})^2 \times r \tag{4.5}$$

  where r is radius of centrifugation in cm, and n is speed in rpm.

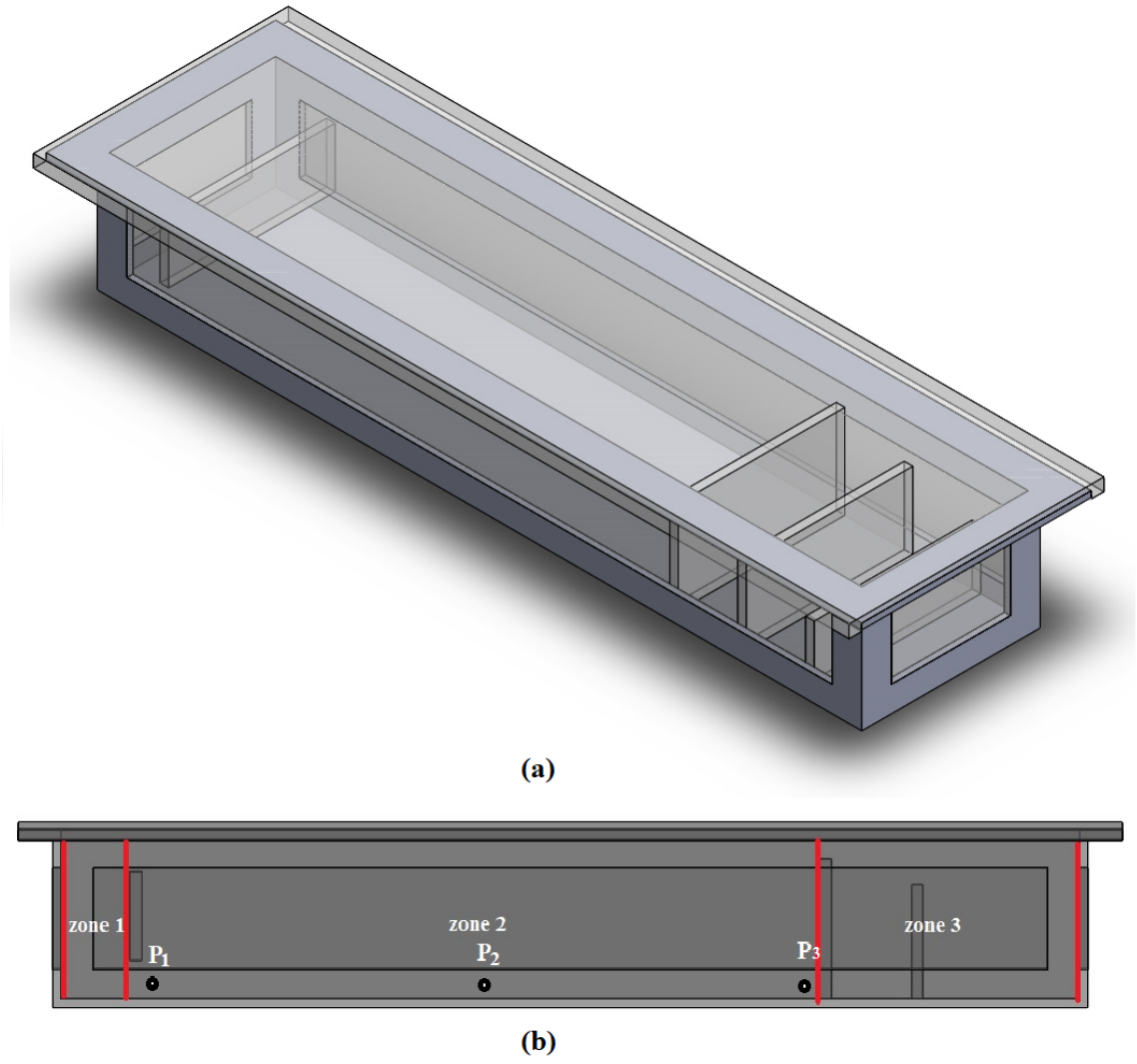

Figure 4.4: 3-D geometric model of the designed separator: (a) Isometric view, (b) Front view

Table 4.3: Biofuge Primo Centrifugal Separator

Rotor designation	Unit	Highconic rotor
maximum permissible load	g	6 ×130
maximum speed n_{max}	min^{-1}	8500
maximum RCF value at n_{max}		10016
angle	$^{\circ}$	45
acceleration time	s	55
braking time	s	35

Table 4.4: Sartorius Analytical Balance BL 60S

Model		BL 60S
Weighting capacity	g	60
Readability	mg	0.1
Tare range (subtractive)	g	60
Repeatability	$\leq \pm mg$	0.1
Sensitivity drift within $+10...30°C$	$\leq \pm K$	2×10^{-6}

In this post-treatment process, the maximum rotation speed has been used, and the RCF value is 10016. The separation process of the samples lasted for 20 min. Under these conditions, it is assumed that the oil and water samples are sufficiently separated, which means that the presence of oil in water is negligible and vice-versa.

- **Analytical Balance** An analytical balance was used to measure the weight of samples before and after the post-separation process. A Sartorius analytical balance (module BL 60S) was selected with the main information for this module is listed in Table 4.4. Flow meters and pressure sensors were installed in the pipelines.

4.2.3 Experimental procedure and operating parameters

National Instruments DAQ USB-6008 DEVICE, NI 9211 Thermo Couple, SignalExpress (National Instruments, 2015), and the LabVIEW (National Instruments, 2015) programs were used for data acquisition. For each test, the separator was first cleaned with pure water, and the water phase was pumped back to the water tank for reuse after each test. The oil phase was further separated in Zone 3 for sufficient resident time, then pumped back to the oil tank for reuse. The separation performance was investigated under various operating conditions. The flow volume was constant at 0.1120 m^3 with accuracy of $\pm$ 0.0114 m^3. Before recording for a test, the volume flows were adjusted by the setup control device. After reaching the operating conditions, the separator was emptied, and then measurements were recorded. When the mixture entered the separator, the inlet volume flow rate reduced dramatically after the mixture hit the first baffle.

At the beginning of the separation process, the unseparated mixture was the main flow in the separator tank. The water or oil phase layer and the oil / water interface layer became visible in the separator with time due to the coalescence and separation process. The location of the interface layer, the top layer of the oil phase, and the top layer of the water phase changed during the separation process. Each operating condition case runs at least twice to achieve repeatability.

To study the separation process, but to avoid the influence of these three layers changing over time, three sampling points were selected from the bottom of the water phase layer, and three more points were selected from the top of the oil phase layer. For each phase, the sampling points were evenly distributed in Zone 2 with the same horizontal position, as shown in Figure 4.4. A maximum volume of 10 ml per sample was taken every minute. The measurement of time using a stopwatch started when the mixture entered Zone 2. The residence time was recorded with an accuracy of

Table 4.5: Testing parameters

Testing parameters	Value
Oil volume fraction	%
10, 20, 30, 35, 50	
Multiphase flow rate	m^3/h
0.227, 0.397, 0.568	

approximately ± 0.5 min. The experiment started with a mixture in Zone 2, with the water volume fraction being the same as the inlet value. As the residence time increased, oil droplets continuously moved to the top layer, and the water volume fraction in the bottom layer increased. Similarly, the oil volume fraction increased in the top layer. Separation efficiency is thus defined as the volume fraction of water in the bottom layer, and the volume fraction of oil in the top layer, represented by Eq. 4.6.

$$\varepsilon = \frac{V_k}{V_{total}} \tag{4.6}$$

where ε is separation efficiency, V_k is phase k volume fraction in the sample, and V_{total} is the total volume fraction in the sample. The volume of each sample can be measured to an accuracy of ± 0.1 ml. In contrast, the accuracy of the sample weight is ± 0.1 mg.

One of the objectives of this study is to provide data on the effect of different operating conditions on oil and water separation efficiency. The oil volume fraction in this experiment is presented in Table 4.5. Based on separator design and the capacity of the separator, the maximum flow rate is less than 1.36 m^3/h (6 GPM). The experimental study was conducted at a temperature of 20°C. The main testing parameters are listed in Table 4.5.

4.2.4 Uncertainty for continuous separation setup

The primary sources of uncertainty in this experiment are calibration of the flow meter (see Appendix A), the accuracy of an analytical balance, and the syringe pump. Other operating uncertainties, such as the change of environment temperature during the experiments, are assumed to be negligible.

In this experimental study, several variables contribute to the overall uncertainty: the flow meter, valves, pressure sensors, and the analytical balance.

The separation efficiency is calculated by oil concentration and oil volume fraction, separately. For example, the concentration method is defined as the percentage of oil weight over the total weight of a sample. The equation of separation efficiency represented by oil concentration is

$$E_{C_{oil}} = \frac{W_{oil}}{W_{total}} \tag{4.7}$$

where, W_{oil}, W_{total} represents the weight of sample after separated / extracted water and the total weight of sample, respectively. The final equation for uncertainty is :

$$E = \frac{\sigma_R}{E_{C_{oil}}} = [\frac{\delta W_{oil}}{W_{oil}}^2 + \frac{\delta W_{total}}{W_{total}}^2]^{\frac{1}{2}} \tag{4.8}$$

4.3 Summary

The experimental apparatus described in this chapter was used to generate experimental data for comparison with the CFD models presented in Chapter 5. The results and comparisons are presented in Chapter 6.

Chapter 5

Development of Numerical Simulations

This chapter describes three CFD simulation models developed using different software packages for oil / water separation. It focuses on ANSYS Fluent, which was initially assumed to be the most appropriate and capable modeling package to be use in modeling two-phase flows. However, the amount of resources required to run full Fluent models was found to be prohibitive in my current research source, thus, other software suites were evaluated, and models were developed to determine if viable models could be developed at a lower computational cost.

5.1 ANSYS Fluent Numerical Simulation Study

In this section, simulation steps and setup of numerical simulation using the ANSYS Fluent are presented. The specific configuration for the simulation is discussed in detail.

5.1.1 Numerical simulation assumptions

To apply the multiphase flow model to the oil / water separation, the following assumptions are maintained: (a) oil droplets are equally dispersed in water, (b) the interpenetration between oil and water should be ignored, meaning oil and water are immiscible with one another, (c) all phases are incompressible, (d) energy losses should be ignored, (e) density and viscosity are both constant in the calculation domain, (f) there is no backward flow at the oil and water outlet, causing the gauge pressure at the outlet to be zero.

5.1.2 Geometry

The objective of this numerical study is to simulate the transient flow of the oil / water separation process. Therefore, only the oil / water separation region is selected for the computational domain. A 2-D two-phase separator model is developed for this study. The length of the computational domain for both separators is 1.776 m, which shares the same geometry as Zone 2 in the experimental setup (see page 52, Figure 4.4). A schematic of the separator for batch separator is presented in Figure 5.1(A). The geometry of the continuous separator is shown in Figure 5.1(B). For the continuous separator, the inlet velocity is adjusted so that the volumetric flow is the same as used in the experiments. The inlet pipe diameter is 0.0254 m, and the inlet is 0.254 m below the top. The pipe diameter of the oil outlet and water outlet are both 0.0254 m.

5.1.3 Mesh Independence Study

A mesh independence study was conducted focusing on the resultant displacement, and a fine mesh was selected to achieve high accuracy. The meshes were generated

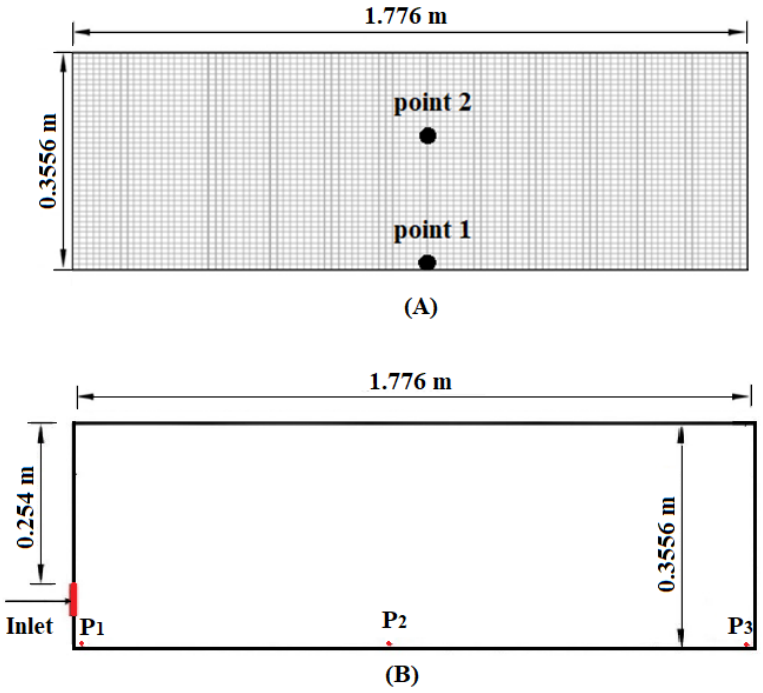

Figure 5.1: Schematic diagram of separator: (A) Batch separator, (B) Continuous separator

using a quadrilaterals method for face meshing, which has an interval size of 0.01. The total amount of nodes is 197,541, with 196,000 elements. The minimum orthogonal quality of this mesh is 1.0, the maximum ortho skew is 0.0, and the maximum aspect ratio is 1.414.

Five different element sizes were selected to create different meshes on the separator (shown in Table 5.1). The oil volume fraction and pressure results are presented in Table 5.2. Their corresponding changes with different mesh sizes are presented in Table 5.3. In these tables, the oil volume fraction refers to the maximum oil volume fraction in the oil sample. It can be seen from Table 5.1 and 5.2 that the element size of 0.05 inches was the most accurate and efficient size for the model. A plot showing the prediction of the oil volume fraction based on the increased node count is shown in Figure 5.2. The point shown in red presents the optimized mesh number. The

Table 5.1: Element size and node count

Element size (inch)	Node count	Face	Cells
0.02	546,156	1,089,744	543,589
0.05	197,541	393,540	196,000
0.08	77,964	154,963	77,000
0.1	49,771	98,770	49,000
0.2	12,987	25,586	12,600

Table 5.2: Mesh convergence study for oil volume fraction and pressure

Mesh	Number of Nodes	Oil volume fraction	Pressure (kPa)
1	546156	0.9301	-1.2790
2	197541	0.9287	-1.2802
3	77964	0.8714	-1.2976
4	49771	0.8458	-1.3315
5	12987	0.8091	-1.3544

element size of 1.27 mm (0.05 inches) was the most accurate and efficient size for the model. The model created with this element size contained approximately 200,000 nodes, which was an enough number of nodes within a Fluent simulation to calculate results accurately.

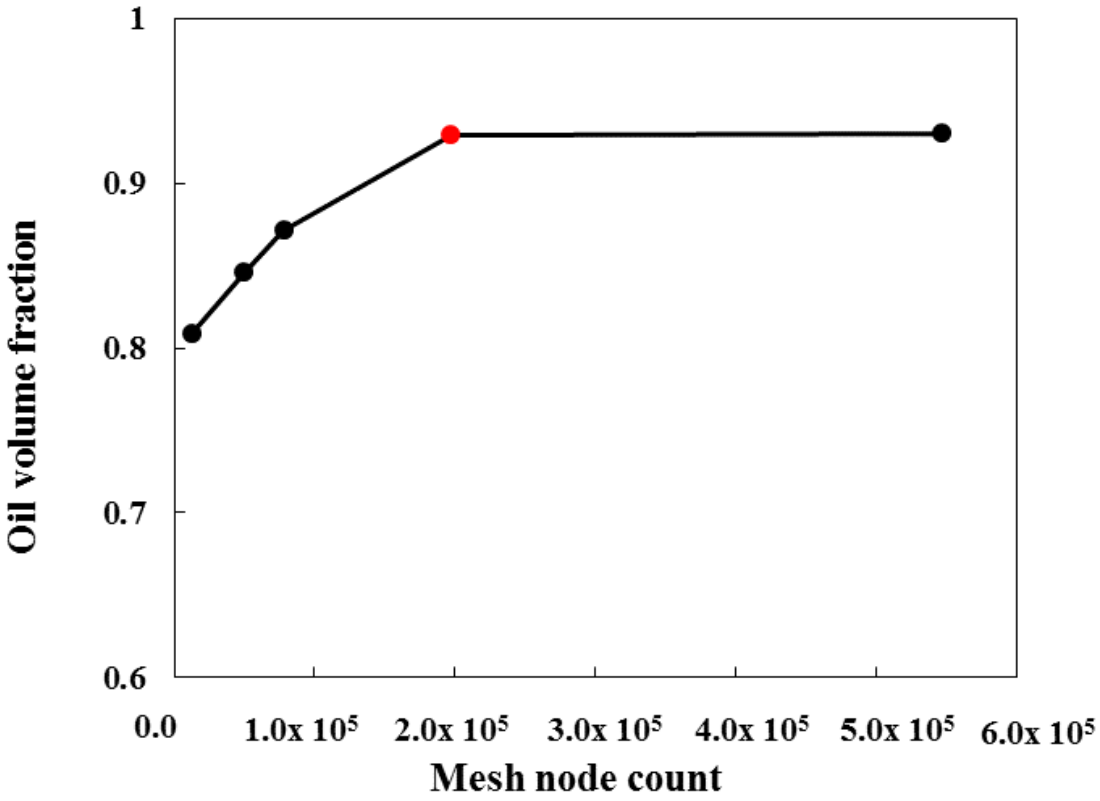

Figure 5.2: Structural mesh dependence study

Table 5.3: Changes in Oil volume fraction and pressure for different meshes

Mesh	Number of Nodes	Change in oil volume fraction	Change in Pressure
1	546156	-	-
2	197541	0.15 %	0.09 %
3	77964	6.31 %	1.46 %
4	49771	9.06 %	3.94 %
5	12987	13.01 %	5.90 %

5.1.4 Multiphase Model

In Fluent, three models are available for multiphase flow problems. Each model has its advantage for different types of problems. The VOF multiphase model is a surface tracking model which can model two or more immiscible fluids by solving a single set of governing equation. The Eulerian model, which is also used for modeling multiphase separation, solves momentum, and continuity equations for each phase; thus, it has a relatively high requirement for computer memory. The Mixture model is a simplified multiphase model that is used to model flows with different velocities, which is an ideal model for a sedimentation process. Based on the literature review in Chapter 1 (see, page 16, Table 2.1), the VOF model and Eulerian model are the most popular two models used in the liquid / liquid separation modeling field. The basic theory of the VOF model is presented in this section.

The VOF model

The VOF model (Volume of Fluid) is a surface tracking method applied to a fixed Eulerian mesh [110]. It is ideal for the study of the interface position between two or more immiscible fluids. In the VOF model, all fluids share a single set of momentum equations. The volume fraction of each phase is tracked in each cell throughout the computational domain. In each control volume, the volume fractions of all phases have a sum of 1. The fields for all variables and properties are shared by the phases and represent volume-averaged values, as long as the volume fraction of each of the phases is known at each location. When the volume fraction of phase one is 1 at certain computational cells, it means only this phase exists in these cells, whereas, if volume fraction is 0, there is no phase one in these cells. When the fraction is between 0 and 1 ($0 <$ fraction < 1), it indicates that both phases exist in this domain. The volume fraction equations in this model are as follows:

The equation for volume fraction variation with time:

$$\frac{\partial F}{\partial t} + \nabla \cdot (F\vec{u}) = 0 \tag{5.1}$$

The volume fraction continuity equation:

$$\frac{\partial \varepsilon_i}{\partial t} + \vec{u}\nabla\varepsilon_i = 0 \tag{5.2}$$

where,

$$\sum_{i=1}^{\infty} \varepsilon_i = 1 \tag{5.3}$$

The Momentum equation:

$$\frac{\partial}{\partial t}(\rho\vec{u}) + \nabla \cdot (\rho\vec{u}\vec{u}) = -\nabla p + \nabla[\mu(\nabla\vec{u} + \nabla\vec{u})] + \rho\vec{g} + F_s \tag{5.4}$$

$$F_s = 2\sigma\kappa\alpha_i\nabla\alpha_i \tag{5.5}$$

where, σ is the surface tension coefficient, $\vec{u}$ is the velocity, μ is the dynamic viscosity, α_i is the volume fraction of phase i, k is surface curvature.

Model Selection Study

Based on the literature review, there is limited research on the oil / water separation process and which model is more suitable for multiphase flow simulation with Fluent. Therefore, in this section, the separation process of oil / water multiphase flow by a horizontal gravity separator is numerically simulated with CFD methods. A model selection study has been conducted.

The contours of volume fraction for different models are shown in Figure 5.3 to Figure 5.5, and constitute one of the most important parameters to define the separation efficiency and the performance of each model. The variation of phase concentration in

the separator for three models is also presented in these figures. Red and blue colors represent oil and water (i.e., the volumetric fractions of the dispersed phase are 1 and 0), respectively. It is found that the VOF model presents the most accurate simulation separation efficiency comparing these three models. As Figure 5.3 shows, the oil volume fraction at the top layer starts to increase significantly at the beginning. After 400 s, the oil volume fraction is close to 1 at the top layer.

In Colman's study [111], he provided a method to measure separation efficiency. In his measurement, polypropylene was utilized to substitute oil droplets as the dispersed phase. His results showed that when an oil droplet had a diameter $d > 45\ \mu m$, the separation efficiency was over 95 %. In this VOF model, the simulation result is consistent with Colman's study. However, in contrast, the Mixture model and Eulerian model predicted poor separation efficiency, as shown in Figure 5.4 and 5.5. This indicates that the VOF model is more suitable for modeling oil / water two-phase separation.

5.1.5 Simulation Setup for Batch Separation

According to the previous model selection study results, the VOF multiphase flow model is adopted for the rest of this thesis, as well as the laminar model. All separator walls are maintained as wall interfaces. The Navier-Stokes (N-S) equations are solved using a pressure-based segregated solver. The Semi-Infinite Method for Pr0essure-Linked Equation (SIMPLE) algorithm [102] is used to calculate the continuity and momentum equations. A stable numerical computation is achieved by setting the under-relaxation factors for pressure and momentum to 0.5 and 0.5, respectively, so that they sum to 1 for better convergence speed [112]. The time step is 1 x 10^{-5} s, and the residual levels for continuity and momentum are 1 x 10^{-5}, which provides a stable and accurate solution for each simulation case, and captures the oil / water

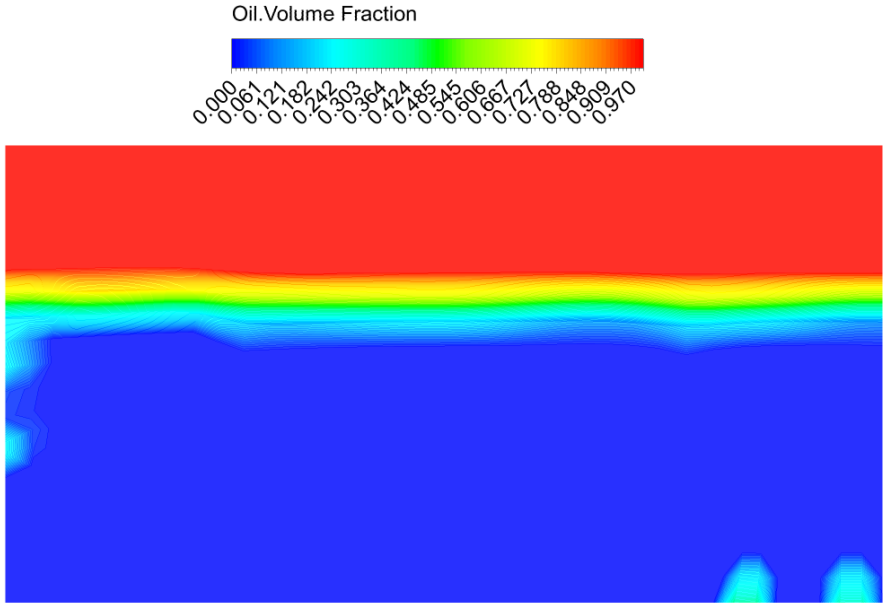

Figure 5.3: Volume fraction for VOF model

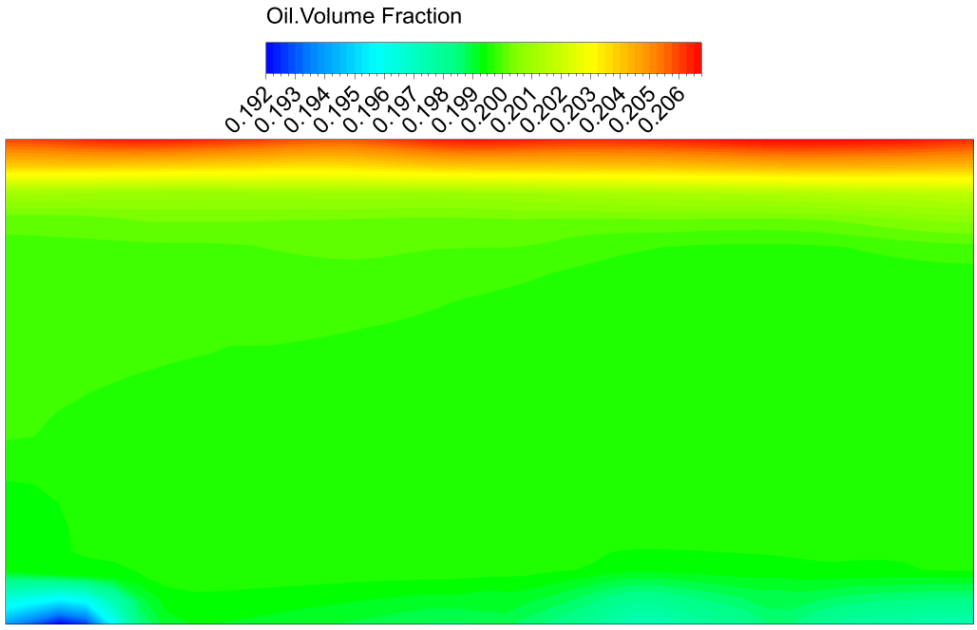

Figure 5.4: Volume fraction for Mixture model

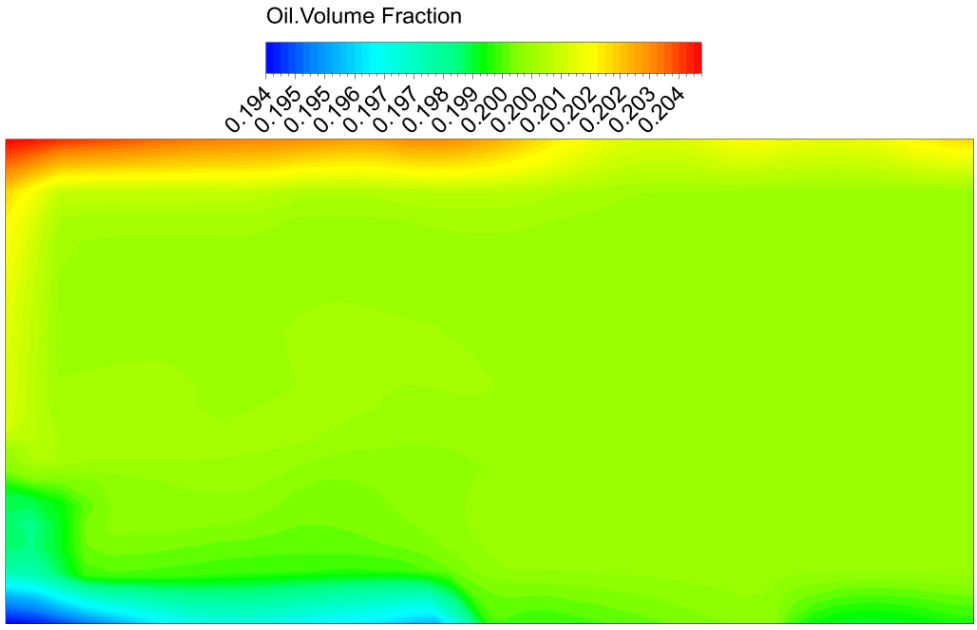

Figure 5.5: Volume fraction for Eulerian model

separation process with the described flow characteristics. The momentum equation is discretized using the Quadratic Upstream Interpolation for Convective Kinetics (QUICK) scheme [110].

For the batch separation process, initial conditions, such as oil volume fraction, are set up into the computational domain by using the patch option in Fluent. The reason for patching the oil volume fraction into the computational domain is that this is a batch separation process, which means the oil / water mixture is already in the separator. The oil and water densities are 872 kg/m^3 and 998 kg/m^3, respectively, and their kinetic viscosities are 0.023 $kg/(m \cdot s)$ and 0.001 $kg/(m \cdot s)$ respectively. The operational pressure and temperature are 101.325 kPa and 20 °C.

5.1.6 Simulation Setup for Continuous Separation

Same as the batch separation process model, a VOF multiphase model is also selected for the continuous separation process. For the fluid in the numerical model, liquid water and oil physical properties are based on the values from the experimental study. For the flow domain, a default operating pressure of 101,325 Pa is used.

Boundary conditions and parameters

For the solution of N-S and momentum equations, appropriate boundary conditions, along with initial conditions, have to be applied to the flow. This section presents the initial and boundary conditions for the simulation study in this thesis: 1) Inlet boundary conditions. For incompressible fluids, mass inlet and velocity inlet have no difference because, for constant density, the velocity inlet boundary condition fixes the mass flow. The pressure inlet defined when the inlet flow rate or velocity is unknown, or there is no inlet. In this study, both the velocity inlet and pressure inlet are used in the two modules separately. 2) Outlet boundary conditions. The pressure outlet condition was used because it often has a better rate of convergence during iteration. 3) Wall interface conditions. In the conditions of this project, the wall of the separator is set, and the medium in the cell zone is multiphase flow. The flow has a no-slip boundary condition. Other parameters, such as roughness, thermal properties, etc., are set at their default values. 4) Operating parameters. The densities of oil and water are 872 kg/m^3 and 992 kg/m^3, respectively. The kinetic viscosity of oil and water are 2.4 x 10^{-3} $kg/(m \cdot s)$ and 1.003 x 10^{-3} $kg/(m \cdot s)$, respectively. The operation gauge pressure is 1 atm or 101,350 Pascal, and the temperature is 288.15 K.

Solver settings

A pressure-based transient solver was used to calculate the oil / water separation process. Gravitational acceleration of -9.81 m/s^2 was activated on the Y-axis on 2-D

Table 5.4: Fluent Solver Settings

Solution	Methods
Scheme	Phase Coupled SIMPLE
Gradient	Least Squares Cell Based
Momentum	Second Order Upwind
Volume Fraction	Geo-Reconstruct
Transient Formulation	Second order Upwind

geometry to simulate a gravity-based separator. Table 5.4 lists the types of solution methods that were used in the Fluent model. Solution methods and schemes were chosen based on examples in the literature and technical support from the ANSYS customer service department. Under-relaxation factors (URF) were set as follows: URF for pressure was 0.7, with 1 for density, body forces, and energy. URF for momentum was 0.3 to control the update of computed variables at each iteration. Therefore, to control the stability and convergence rate of the iterative process. The solution was initialized with standard initialization and was computed from the inlet with a defined velocity in the X-direction. Air was patched into the separator. Residual monitoring was set to absolute criteria of 0.000001 for continuity, u-air, u-oil, u-water, v-air, v-oil, v-water. The calculation was run with a time step of 0.001 s with a maximum of 50 iterations per time step. The solution was completed for 900,000-time steps and thus 900 seconds of flow time.

Time step independence study

In the transient simulation, besides the mesh, the accuracy of the solution is also affected by the time step size. Therefore, a time step independence study was conducted to obtain the most accurate of the simulation results. As can be seen in Table 5.5, five different time steps were investigated by using the selected mesh, which was

Table 5.5: Time Step independence Study

Case	Time stpe	Pressure	Oil volume fraction
1	0.0005	-1.2792	0.9299
2	0.001	-1.2802	0.9287
3	0.002	-1.2969	0.9014
4	0.005	-1.3079	0.8837
5	0.01	-1.3130	0.8756

ranged from 0.0005 to 0.01 s. The most accurate time step size was obtained as 0.0005 s. However, considering the computational costs and the calculation time, a bigger time step of 0.001 s was chosen. The CFD solution with a 1-millisecond time-step size showed an insignificant difference in calculation of the pressure and maximum oil volume fraction.

Based on the above investigation, the simulation setup used in this study is concluded as follows: the multiphase flow model used was the Volume of Fluid (VOF) with two Eulerian phases, in explicit time integration. For the viscous model, the laminar model was chosen due to the actual flow in Zone 2 being in the laminar regime. Gravitational acceleration was then activated in the negative y-direction with a value of $9.81 m/s^2$. The transient process was then defined with a total simulation time between 15 to 30 minutes for all cases. The time step value was chosen using the Courant-Friedrich criterion, which is one of the most common ways to check the stability of an explicit scheme. At each time step, a control-volume based technique was used to convert the governing equations to algebraic equations that can be solved numerically. In the initial condition, Zone 1 and 2 had no mixture and were filled with air. The volume fraction of this was 1. A standard initialization with the Pressure Implicit with Splitting of Operator (PISO) scheme for pressure-velocity coupling

was chosen. The governing equations, together with the initial and boundary conditions, were solved in Fluent 16.2. Integrating the governing equation for each control volume yielded discrete equations that conserved each quantity on a control-volume basis. The set of algebraic equations were solved interactively. When the iterative cycle was completed, the calculation progressed through the remaining time steps.

5.2 Flow-3D Numerical Simulation Study

Flow-3D (10.0.3) software is another numerical application in the field of fluid dynamics with three-dimensional geometry. One of the advantages of Flow-3D is that it has a short computational time, which can significantly reduce the simulation period. Another advantage of Flow-3D is its straightforward simulation setup interface, which includes a series of graphical menus used to set up a problem. For a numerical study, computational time and simulation setup are two important factors, which vary among software. In this thesis, Flow-3D simulation was conducted in order to compare its results with Fluent to choose an optimized simulation software.

5.2.1 Flow-3D Geometry and Setup

The geometry and mesh generated by Flow-3D are shown in Figure 5.6. The multiphase model used in Flow-3D is the drift-flux model. The settlement of drops results in a rise in upward flow in the separator, and dynamical behavior is well defined with the drift-flux model [113, 114]. The model regards the mixture as a single continuous flow, and then solves the volume continuity and the momentum equations for the mixture. Also, the mixture has macroscopic properties, such as the bulk viscosity. The drift-flux model describes the relative flow of the immiscible fluids with different densities. The VOF method, one of the multiphase flow models in Flow-3D [115], enables

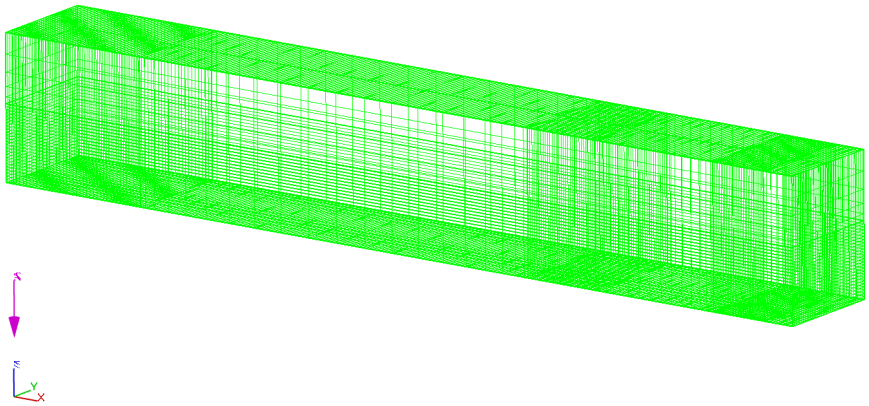

Figure 5.6: Flow-3D Mesh

the tracking of the transient free surface with arbitrary topology and deformations and has been utilized in this study.

5.3 OpenFOAM Numerical Simulation Study

OpenFOAM (18.02) is open-source software that is written in the C++ language. OpenFOAM uses the finite volume method to define how the flow variables are approximated and how the discretization is processed.

In this study, for consistency, the VOF model has been used to simulate the batch separation process. The continuity equation for the volume fraction [116] is

$$\frac{\partial a}{\partial t} + (\boldsymbol{U}\nabla)a = 0 \tag{5.6}$$

where, a is the volume fraction, and its value is between 0 and 1. In the mixture fluid, when a = 0, it refers to the oil phase, and when a = 1, it refers to the water phase.

In contrast to Fluent, the mixture properties, such as density and viscosity, are

calculated based on the volume fraction and according to the following equations:

$$\rho(\mathbf{X}, \mathbf{t}) = \rho_w \alpha + \rho_o (1 - \alpha) \tag{5.7}$$

$$\mu(\mathbf{X}, \mathbf{t}) = \mu_w \alpha + \mu_o (1 - \alpha) \tag{5.8}$$

5.3.1 OpenFOAM Geometry and Setup

The same separator geometry used in the experimental study was used in OpenFOAM (Figure 5.7). The geometry and mesh are defined in the **blockMeshDict** file. After running the snappy mesh generating code, the total number of cells is 222,883, faces mesh is 736,987, and points equal 294,282. Non-orthogonality, or the angle between the center to the centerline between two neighboring faces, and the max skewness are both below 1. The mixture of oil and water occupies the whole domain.

The files U, p, alpha 1, k, and epsilon are defined to set up boundary condition names and values, respectively. All the codes are listed in Appendix K. The specified values for each condition are the same as the experimental study and Flow-3D values.

The fluid properties is definded in the **transportProprieties** file. The oil and water phase is defined as Newtonian flow. Files to define the main proprieties of fluids are listed as follows:

- File **nu** defines the kinematic viscosity, and is set to 1 x 10^{-06} for water and 2.75 x 10^{-06} for oil.
- File **rho** defines the density of oil and water, which is set as the same value as the experimental study; 992 kg/m^3 for water and 872 kg/m^3 for oil.
- File **sigma** defines the surface tension between oil and water, set at 0.0356.

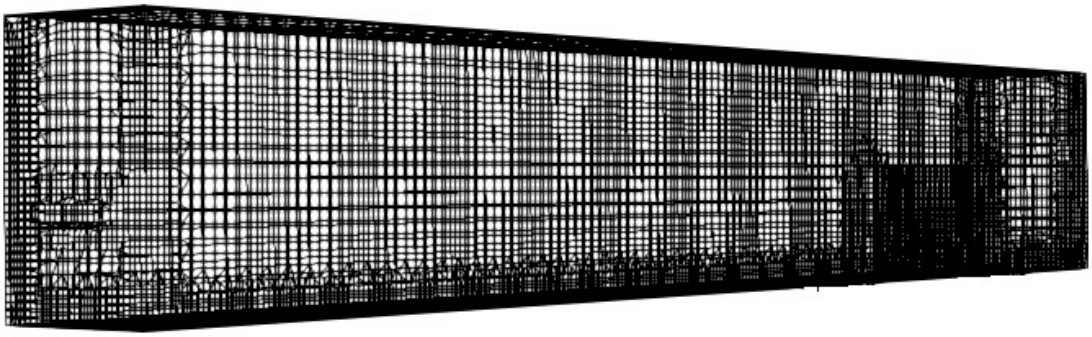

(a)

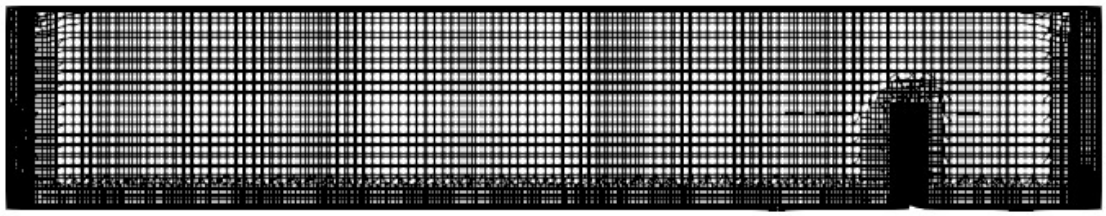

(b)

Figure 5.7: Geometry and mesh - OpenFOAM: (a) Isometric view, (b) Front view

- File **g** defines the gravity value. Gravity is a uniform vector throughout the computational domain, which is 9.8 m/s^2.

The laminar model is selected in **turbulenceProperties** file to maintain the consistency with the other two CFD software and to compare the results more accurately.

5.3.2 OpenFOAM Data Output Setting

As highlighted in the OpenFOAM user guide [117], the surface tracking algorithm in interFOAM is determined by the Courant number. It is defined as follows:

$$C_o = \frac{\Delta \cdot |U|}{\Delta x} \tag{5.9}$$

where Δx is the width of the cell in the velocity direction, and Δt is the time step. The maximum Courant number is the ratio of the maximum distance traveled by the fluid in a time step divided by the cell size. The recommended default value for this variable is ≤ 0.5. The **controlDict** file is used to define these values. In this thesis, four parallel processors were used to calculate the simulation case.

Chapter 6

Semi - Analytical Model: Results and Discussion

This chapter is organized as follows: The first section presents the calculation of oil droplet velocity, and the oil / water interface tracking model is presented in the second section. Afterward, the semi-analytical model for droplet coalescence is covered in detail. Last, the validation of the developed model is conducted.

6.1 Critical Time Calculation and Interface Tracking

Time is a crucial factor in the development of the coalescence model. Therefore, it is essential to calculate the critical time for a droplet to achieve the terminal velocity. If the critical time is very short compared to the coalescence process, the droplet acceleration time can be neglected; otherwise, the droplet acceleration time needs to be considered when developing the coalescence model. The critical time is defined in Eq. 3.36. To solve this equation, a MATLAB code is programmed to calculate the

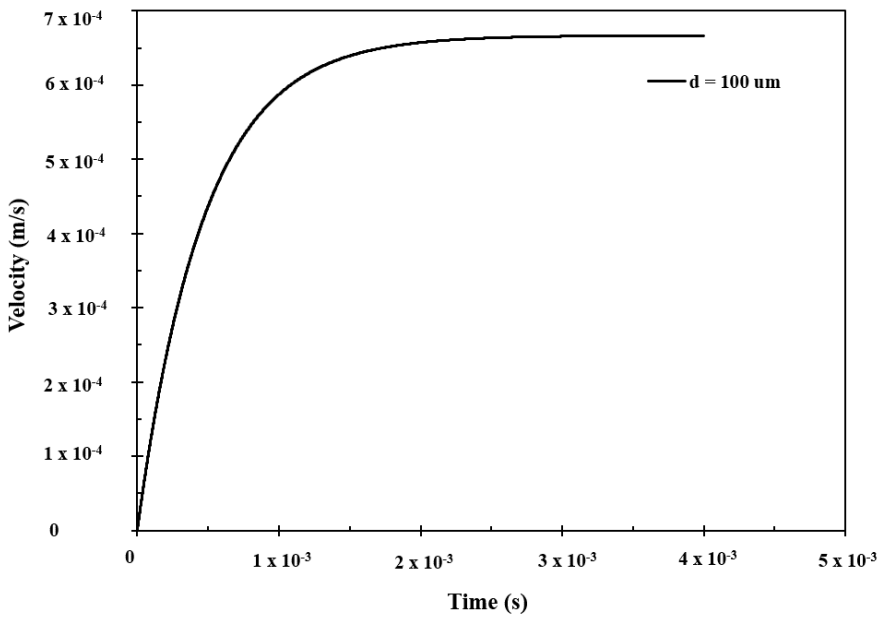

Figure 6.1: Oil droplet rising velocity

critical time (t_{cri}) when the oil droplet reaches a steady-state velocity (u_{s-s}). The single oil droplet terminal velocity is about 6.75 x 10^{-4} m/s (see Figure 6.1). The critical time for this oil droplet to reach terminal velocity is about 3×10^{-3} second. This time is negligible when considering droplet coalescence time. Therefore, we assume that single oil droplet rising velocity is a constant value, $v_v = u_{s-s}$.

The vertical location of the oil / water interface is tracked over time. Figure 6.2 compares the CFD simulation prediction and force balance analytical model. The analytical model is developed based on Stokes' law, where the longest droplet rising path predicted by Stokes' law represents the bottom layer of the mixture.

The interface tracking model predicts a higher interface layer than force balance (see Figure 6.2). This indicates that the separation process is slower than the Stokes' law trend. This is because oil droplets separation process involves collision, coalescence, and breaking. Each of these contributes to slowing the separation process.

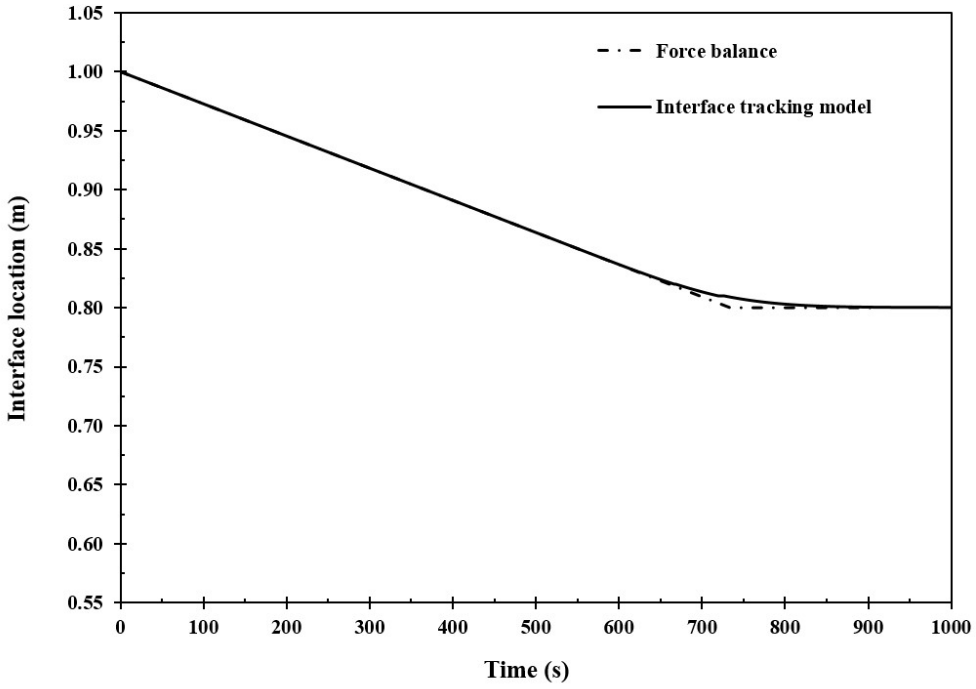

Figure 6.2: Oil / water interface location tracking with force balance model and interface tracking model

6.2 Droplet Coalescence Model Development

As presented in Eq. 3.41, a droplet's rising velocity is proportional to its radius; therefore, as droplets coalesce, the rising velocity increases. Furthermore, the rate of coalescence is proportional to the fraction of the dispersed phase as more droplets are available for collision and coalescence. Thus, to develop a new model for coalescence during oil / water separation, eleven different numerical predictions were conducted (see Table 6.1) with varied droplet diameter and oil fraction ($\varepsilon_o = V_o/V_{total}$).

The terminal velocity of droplets (from Eq. 3.37) with a diameter of 150, 200, 250, and 500 μm was 0.0015, 0.0027, 0.0042, and 0.0167 m/s, respectively. Terminal velocity was reached in 2.5, 7.5, 10, and 70 ms, respectively (see Figure 6.3), which is considered negligible in this study.

Figure 6.4 shows the separation process as predicted by Eq. 3.37. The y-axis

Table 6.1: Numerical study of batch separation cases

Case	Oil droplet diameter (m/s) $d_{oil}(\mu m)$	Oil volume fraction ε
Base case	**100**	0.2
# 1	**150**	0.2
# 2	**200**	0.2
# 3	**500**	0.2
# 4	200	**0.1**
# 5	200	**0.3**
# 6	200	**0.4**
# 7	200	**0.5**
# 8	200	**0.6**
# 9	200	**0.7**
# 10	200	**0.8**
# 11	200	**0.9**

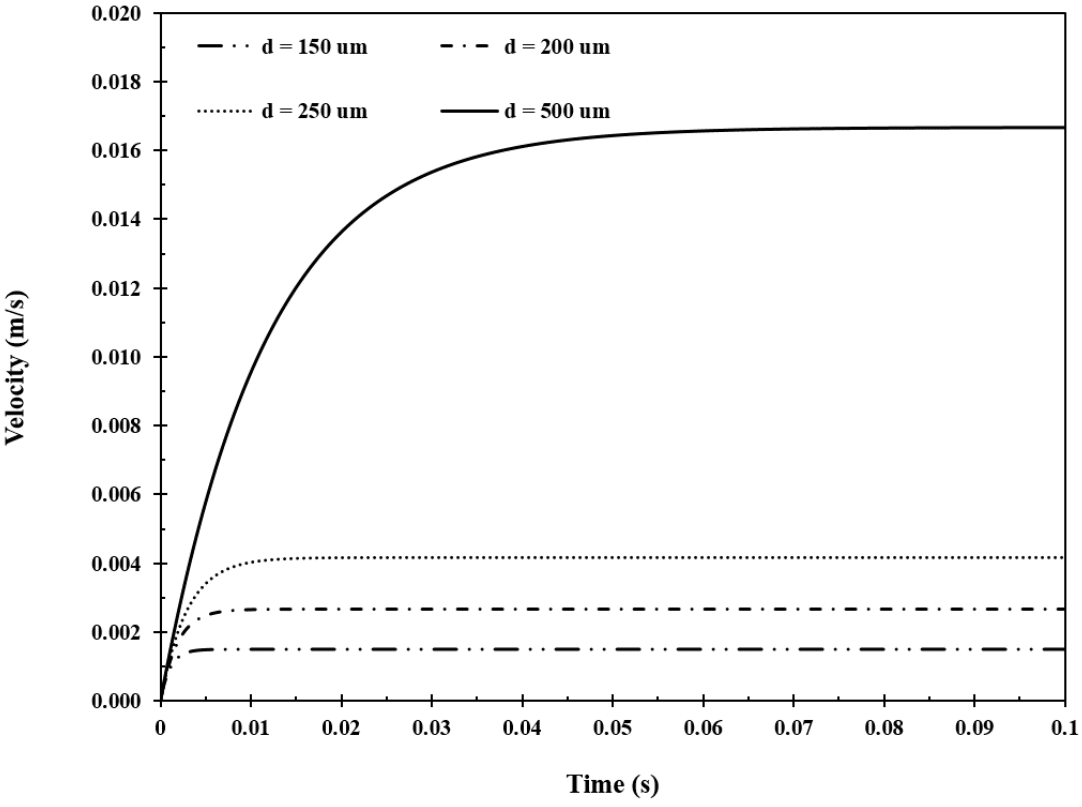

Figure 6.3: Terminal velocity calculation

presents the droplet rising distance (Y_r), which was determined by rising velocity (v_v) and time (t). As illustrated in Figure 6.4 (a) – (c), a force balance model (Eq. 3.37) does not adequately predict the separation process. For example, when the oil droplet diameter is less than 250 μm, the separation time is approximately 10 s, according to the analytical model; however, when the oil droplet diameter is 500 μm, the analytical separation time is less than 2 s. These results do not agree with the numerical predictions. According to the analytical model assumption, all droplets have a uniform diameter, which means the analytical model does not include the droplet coalescence process. Therefore, the separation time predicted by the analytical model is the longest possible. As shown in Figures 6.4 (a) and (b), when oil droplet diameter is smaller than 250 μm, the rising time calculated by Stokes' law requires more time than the simulation results. However, when the droplet diameter is 500 μm, the analytical model requires less separation time than the numerical simulation; see Figure 6.4 (c), which is in contradiction to the analytical assumption. Therefore, the diameter of the droplet after coalescence should be within 250 μm.

Figure 6.5 illustrates a time series of oil volume fraction contours to represent the oil / water separation process. A zoomed-in region (6.6) illustrates a detailed view of the coalescence processes and transient accumulation of the oil phase. From 0 to 2 seconds, the majority of oil droplets have not yet experienced coalescence. In this step, a high density of droplets is formed (see Figure 6.5(a)); the oil phase has not yet accumulated on the surface as the thickness of the oil phase (Y_o) is zero when t = 2 s (Figure 6.6(a)). From 4 to 12 seconds, the system undergoes multiple binary droplet coalescence processes. During this stage, a significant amount of oil is separated from the water to form an oil phase on the surface (Figures. 6.6(b) to 6.6(d)). Also, as illustrated in Figures. 6.6(b) and 6.6(c), the droplets have a variety of different diameters. After the initial coalescence process, the distance between the

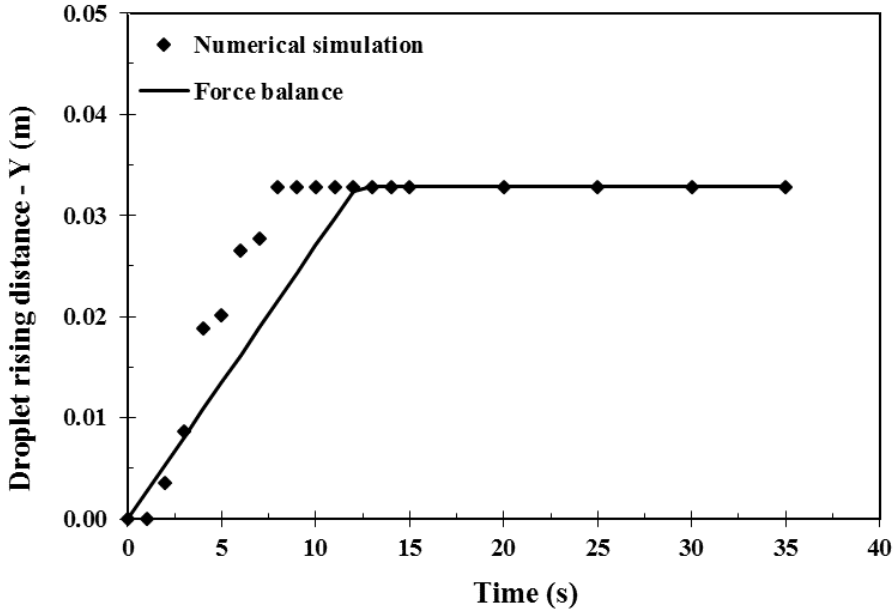
Numerical simulation
Force balance
Droplet rising distance - Y (m)
Time (s)
0.00
0.01
0.02
0.03
0.04
0.05
0
5
10
15
20
25
30
35
40

(a)

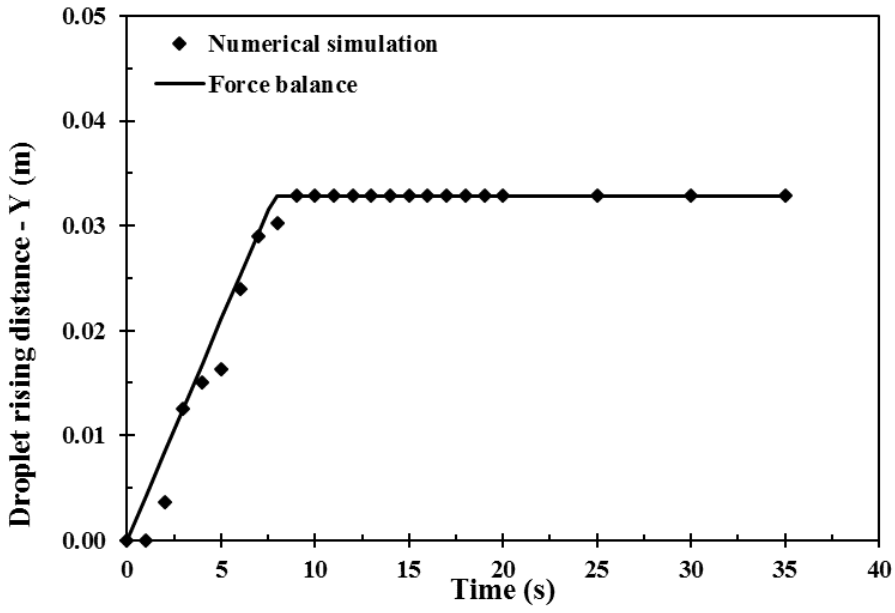
Numerical simulation
Force balance
Droplet rising distance - Y (m)
Time (s)
0.00
0.01
0.02
0.03
0.04
0.05
0
5
10
15
20
25
30
35
40

(b)

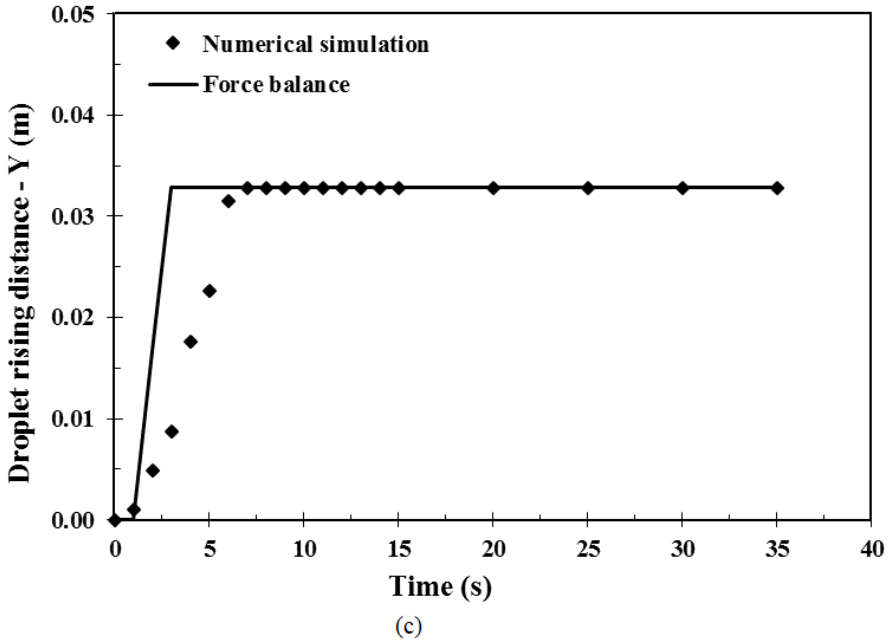

Figure 6.4: Liquid / liquid separation for droplet diameter of (a) 200 μm, (b) 250 μm, and (c) 500 μm

newly formed droplets is different. Therefore, the time needed for the following binary droplet coalescence process varies for different droplet pairs. The entire process lasts approximately 16 seconds, as Y_o becomes independent of time (Figure 6.5(e)).

6.2.1 Numerical simulation data validation

The coalescence model was developed based on numerical data for the simpler case of batch separation. Experiments were conducted, and the results were compared with numerical data to validate the accuracy of the numerical simulation results. As illustrated in Figure 6.7, the oil phase began to form approximately two minutes after the stirrer was turned off, and then the slope increased with time until the separation was complete. The separation process took approximately eighteen minutes to achieve full separation, where $Y' = 20$ %. Validation of the numerical results with experimental data is presented in Figure 6.7. The normalized thickness (Y') is used to

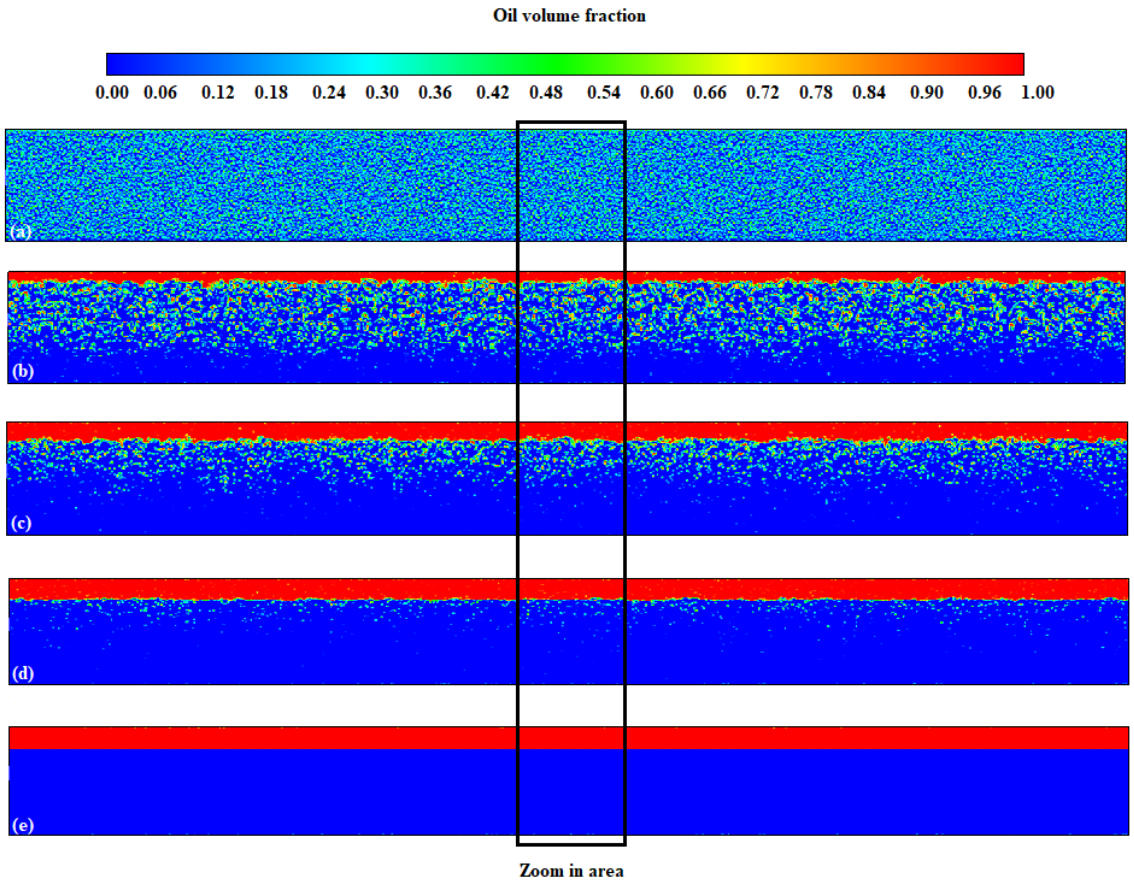

Figure 6.5: Full scale of the separation process presented by oil volume fraction contours for the Base case: (a) t = 2 s, (b) t = 4 s, (c) t = 8 s, (d) t = 12 s, and (e) t = 16 s

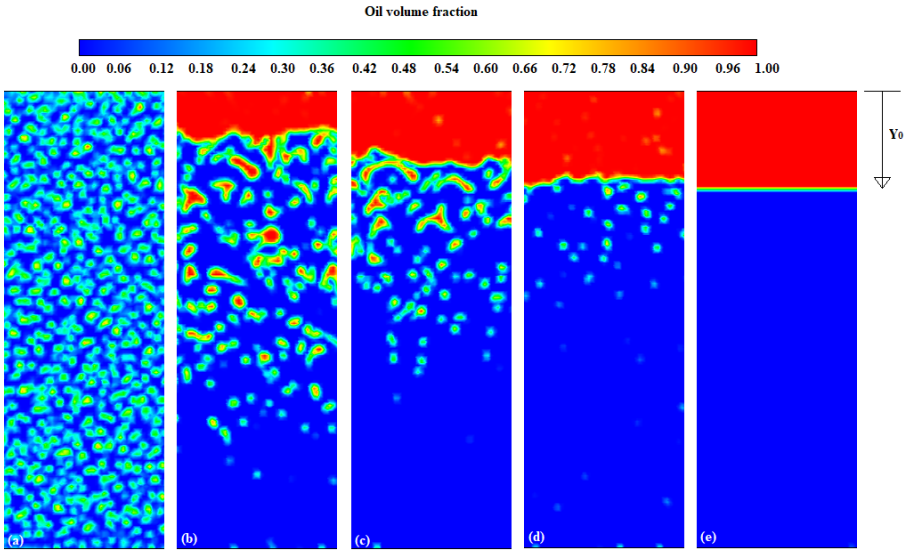

Figure 6.6: Zoomed-in scale of the separation process presented by oil volume fraction contours for the Base case: (a) t = 2 s, (b) t = 4 s, (c) t = 8 s, (d) t = 12 s, and (e) t = 16 s.

compare numerical predictions with experimental data. As illustrated in Figure 6.7, the numerical predictions of liquid / liquid separation agree well with the experimental data (the average relative error was 13.39 %) for an oil / water fraction of 20 / 80 and a liquid height of 17.76 cm.

6.2.2 Development of droplet coalescence model

Numerical simulations were conducted in ANSYS Workbench 18.2 for 2-D simulation of a gravity-based oil / water separator. The CFD simulation results are plotted with the growth of separated oil phase with time as described in the sections following.

(A) Oil droplet in the water phase

When the oil volume fraction is less than 0.5, the mixture can be represented as oil droplets in a continuous oil phase [118]. As illustrated in Figure 6.8, the time for each coalescence step decreases with the increasing oil volume fraction due to the increased

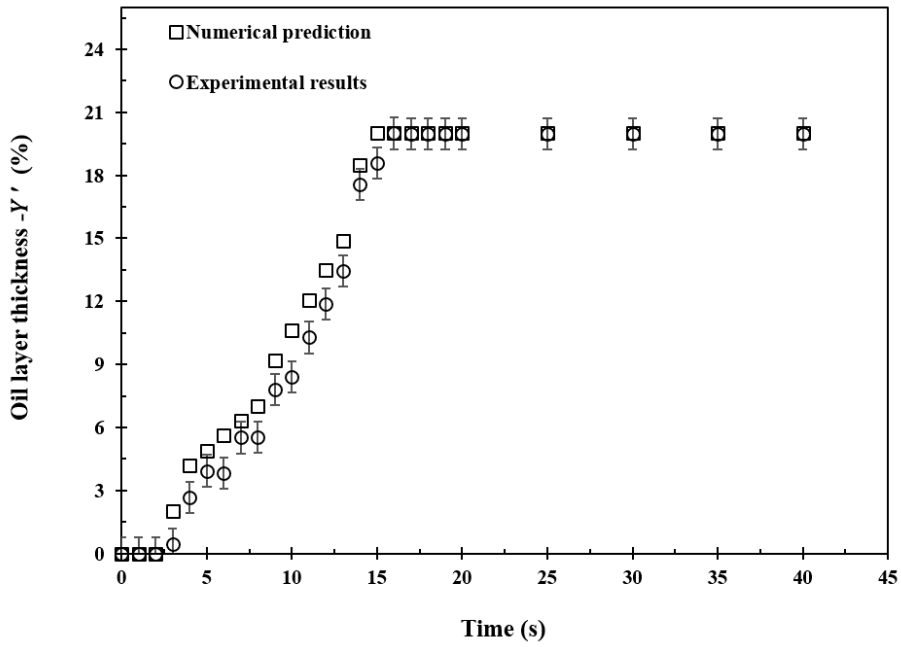

Figure 6.7: Liquid / liquid separation for an oil / water fraction of 20 / 80

quantity of droplets in the mixture. The relationship between total coalescence time and binary droplet coalescence step is a second-order polynomial,

$$t_{coal} = a_{o/w} \cdot 2^{2n} + b_{o/w} \cdot 2^{n} + c_{o/w} \tag{6.1}$$

where the constants $a_{o/w}$, $b_{o/w}$, and $c_{o/w}$ are a function of oil volume fraction, and n is binary droplet coalescence step. They are determined by finding the trendline of each ε_o, by finding the relation between the value of $a_{o/w}$, $b_{o/w}$, and $c_{o/w}$ and the ε_o.

The steps to determine the relationship between ε_o and $a_{o/w}$, as well as $b_{o/w}$, and $c_{o/w}$, are presented in detail for the example where $\varepsilon_o = 0.2$. First, plot the time needed for each binary coalescence process. According to the simulation results, the time needed for the first two droplets to coalesce is 2 s; the time needed for the second coalescence process is 6 s; the time needed for the third coalescence process is 8s. Then plot the trend line for Eq. 6.1 to get the total coalescence time as a function of binary

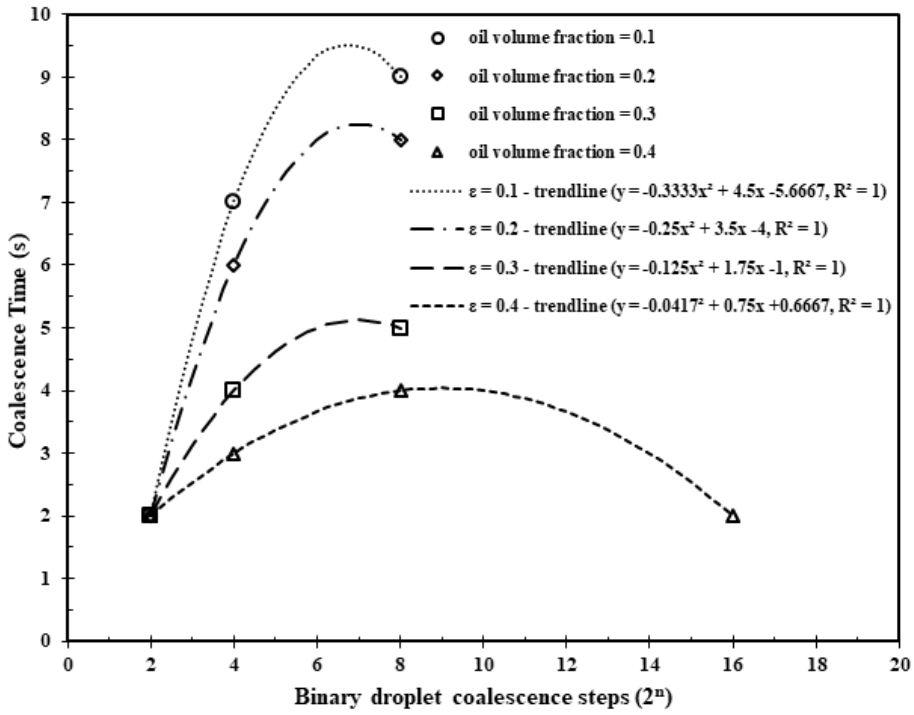

Figure 6.8: The oil droplet in water coalescence model development.

droplet coalescence steps, as shown in Figure 6.8. The same procedure is used for other oil volume fraction cases.

The next step is to find the relationship between $a_{o/w}$, $b_{o/w}$, and $c_{o/w}$ and ε_o separately. For example, to find the relationship between $a_{o/w}$ and ε_o, the values of $a_{o/w}$ for different oil volume fractions are plotted to predict the trend line. This trend line gives the relationship between $a_{o/w}$ and ε_o. Also, the same method was used to predict the relation between $b_{o/w}$, $c_{o/w}$, and ε_o separately. As shown in Figure 6.9, the values of $a_{o/w}$, $b_{o/w}$, and $c_{o/w}$ are linearly proportional to the oil volume fraction of the mixture. Also, the values of $a_{o/w}$ and $c_{o/w}$ increase with increasing oil volume fraction and $b_{o/w}$ decreases with increasing oil volume fraction. Substituting the relationship between the oil volume fraction and $a_{o/w}$, $b_{o/w}$, and $c_{o/w}$ into Eq. 6.1 provides a new correlation for coalescence time as a function of oil volume fraction and binary droplet

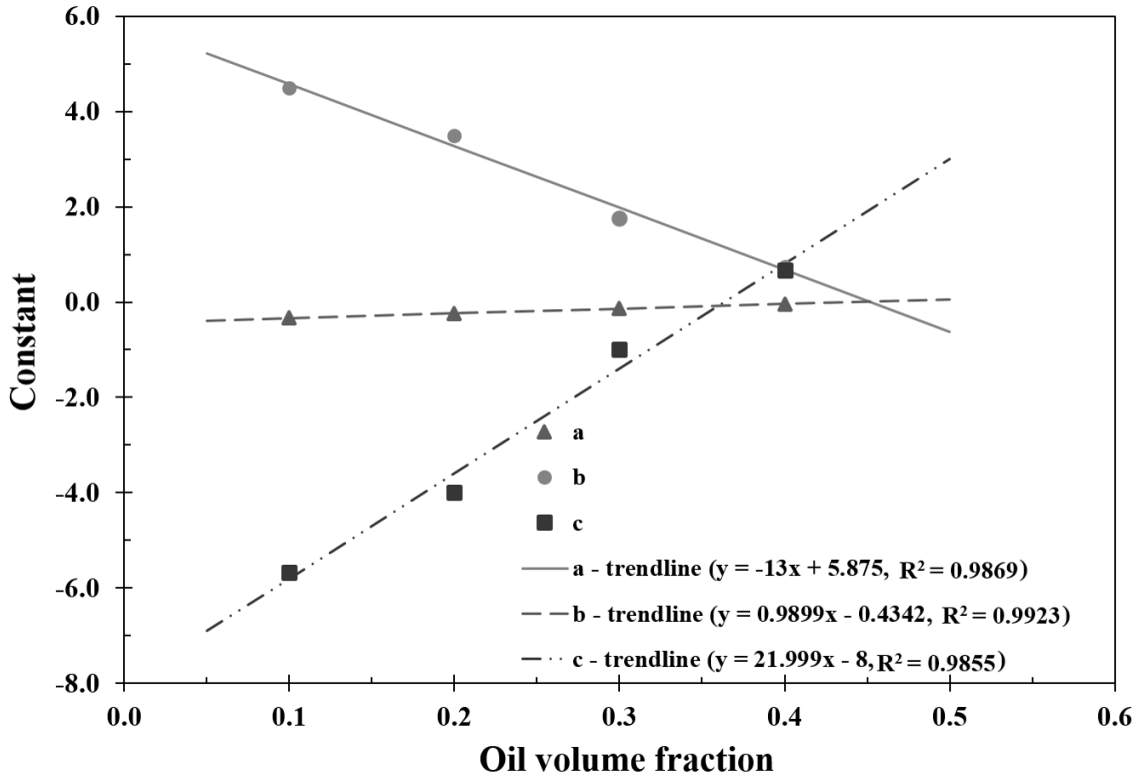

Figure 6.9: Correlation constant values calculation for oil droplet.

coalescence steps,

$$t_{coal} = f_{o/w}(\varepsilon_o) \cdot 2^{2n} + f'_{o/w}(\varepsilon_o) \cdot 2^n + f''_{o/w}(\varepsilon_o) \tag{6.2}$$

where $f_{o/w}$, $f'_{o/w}(\varepsilon_o)$, and $f''_{o/w}(\varepsilon_o) f_{o/w}$, $f'_{o/w}(\varepsilon_o)$ and $f''_{o/w}(\varepsilon_o)$ represent the value of $a_{o/w}, b_{o/w}$, and $c_{o/w}$ as a function of ε_o, respectively.

Figure 6.10 shows how the new coalescence correlation for oil droplets in water (Eq. 6.2) can be used with a force balance (Eq. 3.37) to obtain accurate predictions of liquid / liquid separation dynamics. There is a strong correlation between numerical prediction and Eq. 3.43. (see Figure 6.8). Take the results of $\varepsilon_o = 0.2$ as an example. As presented in Figure 6.10 (b), four binary oil droplets coalescence processes are predicted as there are three velocity steps. Comparing the results of the coalescence

model (Eq. 3.43) with the force balance (Eq. 3.37), one can see that Eq. 3.43, i.e. the coalescence model gives a high accuracy in predicting the oil droplets coalescence process obtained with simulation (average relative error within 10 %).

The developed coalescence model can be combined with a force balance method to predict the separation dynamics with an average error of 7.4 %, 9.2 %, 7.2 %, and 5.9 % for each simulation case as shown in Figure 6.10 (a) – (d), respectively. Even though the proposed coalescence model only applied force balance with droplet coalescence to predict the separation process, it has significantly improved the accuracy compared to the force balance model only, which had an average error in the range of 35 % to 50 %. However, as noted previously, studies [89–93] show that droplet coalescence is a complex process which includes coalescence frequency, coalescence efficiency, and collision frequency. In the present model, all these factors are simplified into the force balance with the binary droplet coalescence process.

(B)Water droplet in the oil phase

When the oil volume fraction is more than 0.5, the mixture can be treated as water droplets in a continuous oil phase [119]. The coalescence model can still follow Eq. 3.41 and Eq. 6.2, but it is for the water droplets coalescence process. Therefore, the coalescence model for water droplet is shown in Eq. 6.3. The same droplet size is used in this simulation study, $d_w = 100\ \mu m$. As demonstrated in Figure 6.11, the time required for each coalescence step decreases with the increasing oil volume fraction due to the decreased quantity of water in the mixture. First, it is assumed that the relationship between the coalescence time and binary droplet coalescence is a second-order polynomial,

$$t_{coal} = a_{w/o} \cdot 2^{2n} + b_{w/o} \cdot 2^{n} + c_{w/o} \tag{6.3}$$

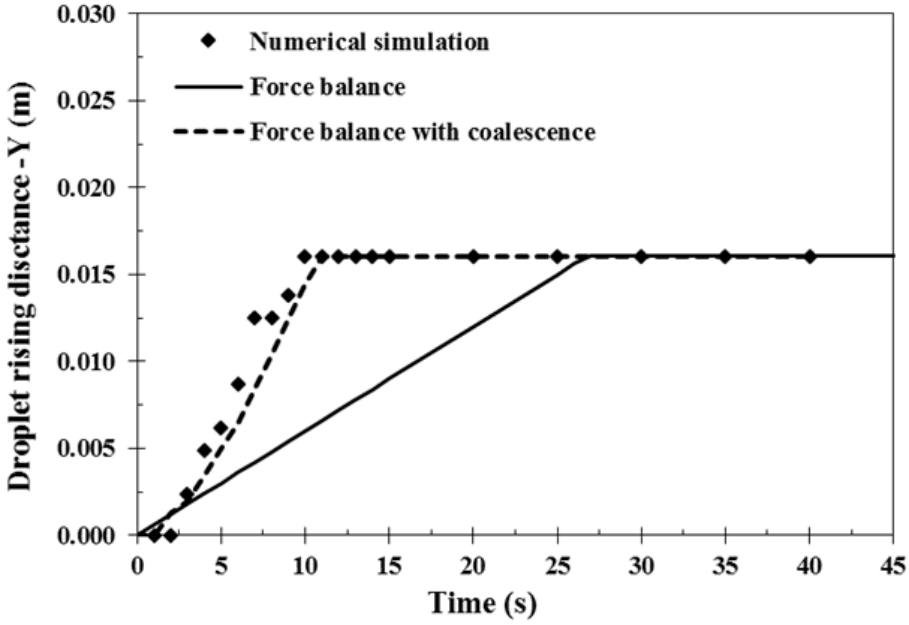
Numerical simulation
Force balance
Force balance with coalescence
Droplet rising disctance - Y (m)
0.030
0.025
0.020
0.015
0.010
0.005
0.000
0
5
10
15
20
25
30
35
40
45
Time (s)

(a)

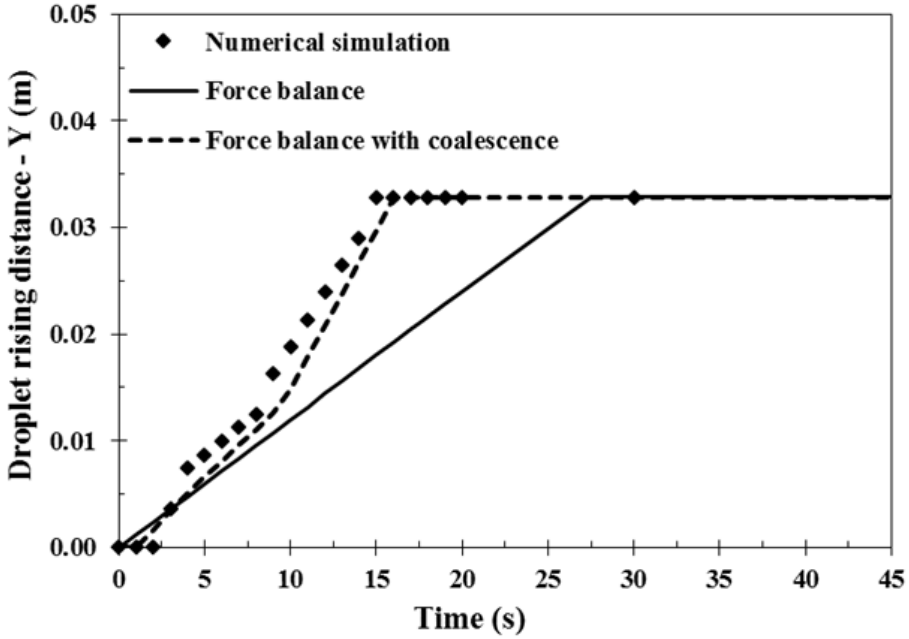
Numerical simulation
Force balance
Force balance with coalescence
Droplet rising distance - Y (m)
0.05
0.04
0.03
0.02
0.01
0.00
0
5
10
15
20
25
30
35
40
45
Time (s)

(b)

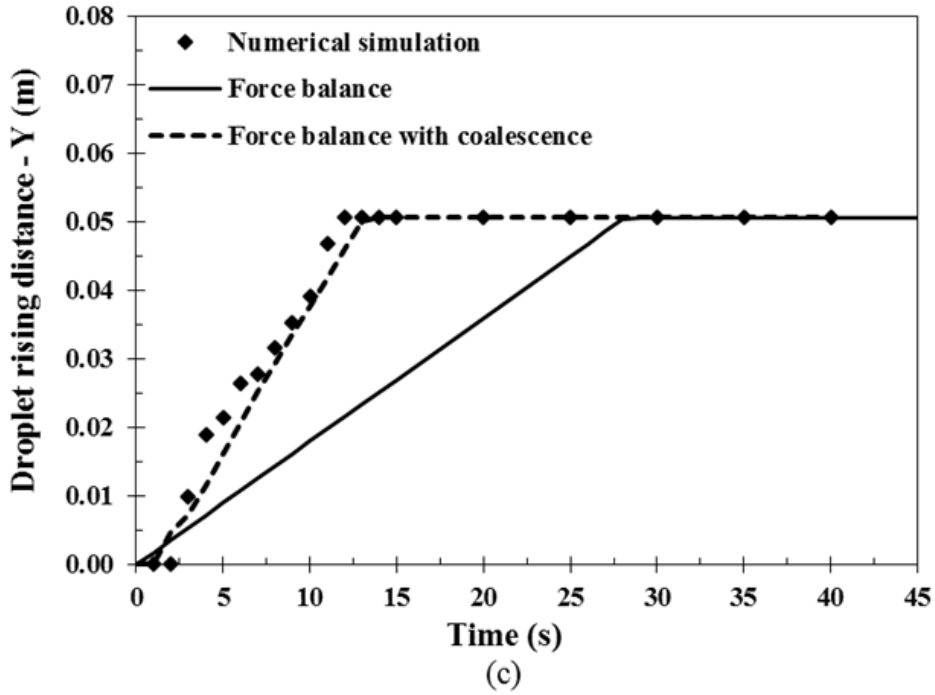

(c)

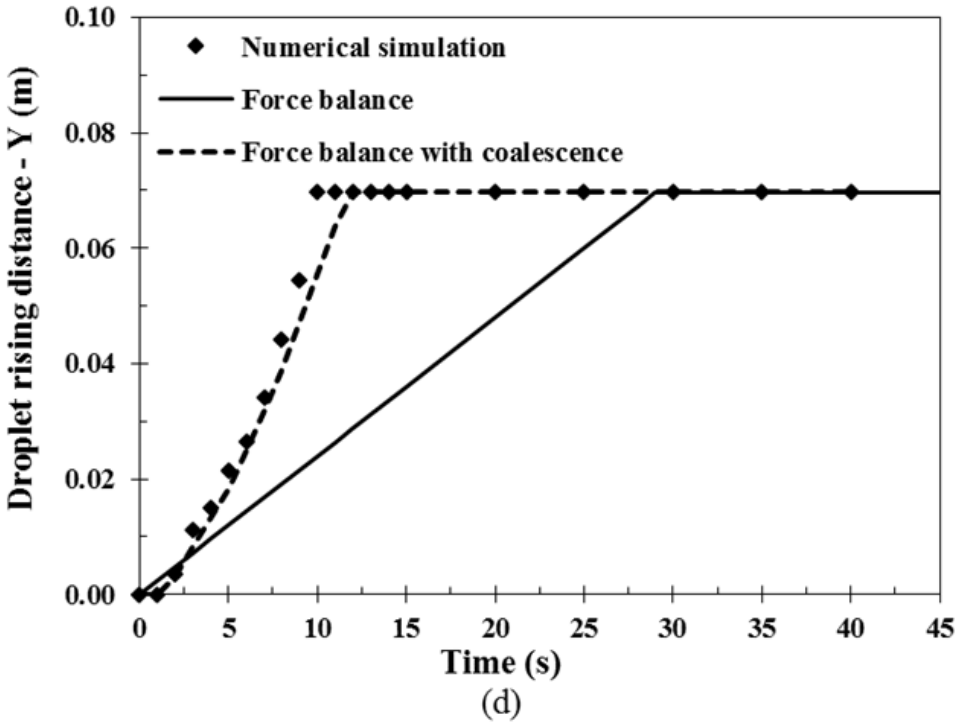

(d)

Figure 6.10: Oil droplets in the water phase coalescence process production comparison: (a) oil volume fraction = 0.1. (b) oil volume fraction = 0.2. (c) oil volume fraction = 0.3. (d) oil volume fraction = 0.4.

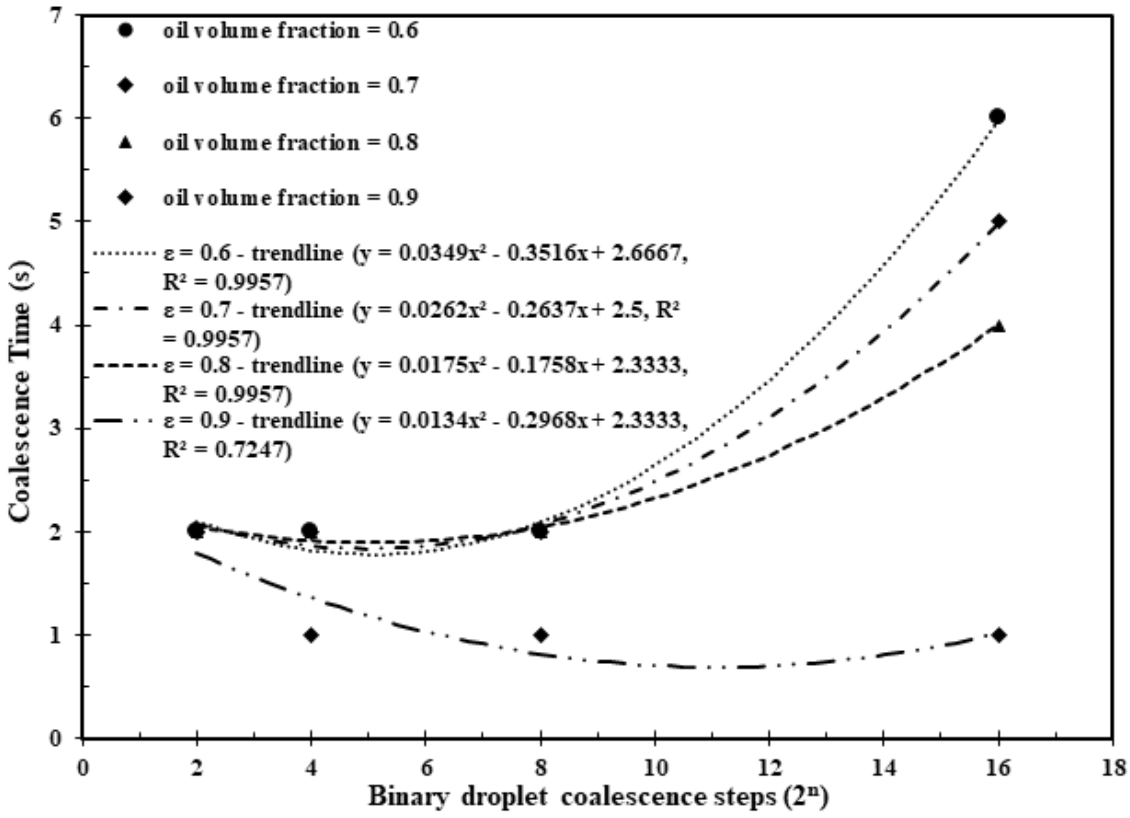

Figure 6.11: The water droplet in oil coalescence model development

where the constants $a_{w/o}$, $b_{w/o}$, and $c_{w/o}$ are functions of oil volume fraction. The same method which is used to determine the value for $a_{o/w}$, $b_{o/w}$, and $c_{o/w}$ is utilized to determine the value for $a_{w/o}$, $b_{w/o}$, and $c_{w/o}$.

The relationship between constants $a_{w/o}$, $b_{w/o}$, and $c_{w/o}$ and ε_o is indicated in Figure 6.11. For example, when $\varepsilon_o = 0.6$, the time needed for the first binary droplets coalescence is 2 s; the time needed for the last binary droplets coalescence is 6 s. Then the trend line for total coalesces time can be found by Eq. 6.3, which is shown in Figure 6.11. As predicted by the trend line, the constant $c_{w/o}$ is independent of ε_o. The average value for $c_{w/o}$ is 2.5. All the solutions for Eq. 6.3 are combined to develop the relationship between $a_{w/o}$, $b_{w/o}$ and ε_o. The results are illustrated in Figure 6.12, where $a_{w/o}$ and $b_{w/o}$ is linearly proportional to ε_o. The value of $a_{w/o}$ slightly decreases

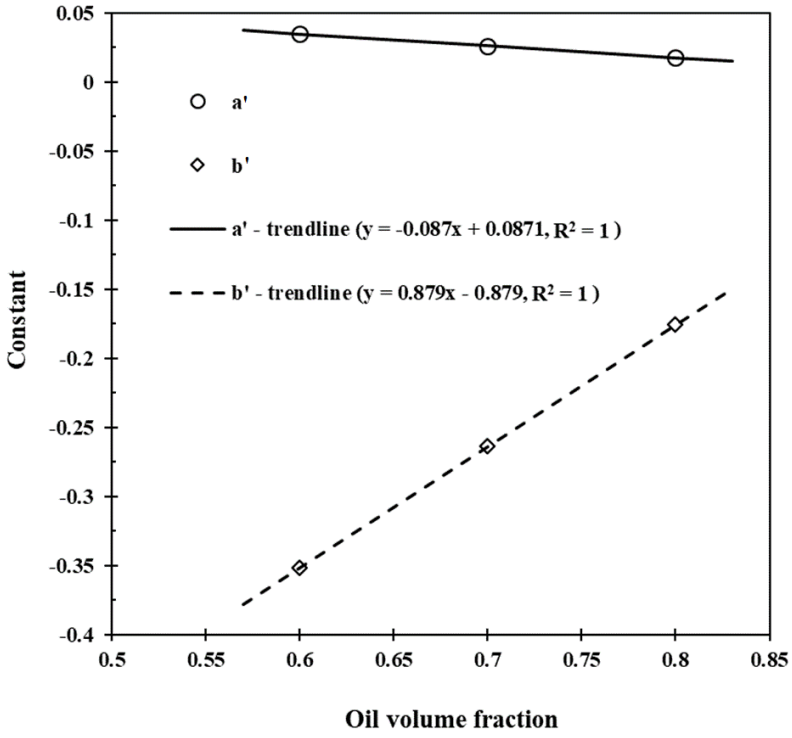

Figure 6.12: Correlation constant values calculation for water droplet.

with ε_o while $b_{w/o}$ increases dramatically with ε_o. Combining the relationship for oil volume fraction with $a_{w/o}$ and $b_{w/o}$ in Eq. 6.3, we obtain the new correlation for coalescence time (t_{coal}) as a function of ε_o and binary droplet coalescence steps,

$$t_{coal} = f_{w/o}(\varepsilon_{oil}) \cdot 2^{2n} + f'_{w/o}(\varepsilon_{oil}) \cdot 2^{n} + 2.5 \tag{6.4}$$

where, $f_{(w/o)}$, $f'_{(w/o)}(\varepsilon_{oil})$ and $f''_{(w/o)}(\varepsilon_{oil})$ represents the constants $a_{w/o}$, $b_{w/o}$, and $c_{w/o}$ as a function of ε_{oil}, respectively.

As illustrated in Figure 6.13, the new coalescence correlation for oil droplets in water (Eq. 6.4) can be combined with a force balance (Eq. 3.37) to obtain accurate predictions of liquid / liquid separation dynamics. As presented in Figure 6.13, both the coalescence process and coalescence time decrease as the oil volume fraction

increases. Similar results were found by Kocherginsky et al. [37]. By studying the demulsification process of water droplets, they found that an increase in the initial water volume fraction results in the decrease of flux, therefore, decreasing the water content in the product oil. According to the coalescence mechanism proposed in their study, a decrease in flux results in an increase of coalescence.

The coalescence model developed here is based on the binary droplet coalescence process, which then updates the droplet force balance equation (see Eq. 3.43) by applying the new droplet diameter. The numerical prediction, the updated force balance equation with the coalescence model, as well as the simplified force balance equation from Stokes law are compared in Figure 6.13. A strong match between the numerical prediction and Eq. 3.43 is shown. For example, four binary oil droplets coalescence processes are predicted as there are three velocity steps presented in Figure 6.13 (c), where $\varepsilon_o = 0.8$. Comparing the results of the coalescence model (Eq. 3.43) with force balance (Eq. 3.37) for water droplets in the oil phase, one can see that the Eq. 3.43 coalescence model shows high accuracy in predicting the water droplets coalescence process (relative error within 15 %).

In Eqs. 6.2 and 6.4, it assumed that droplets have the same diameter, which is difficult to fully achieve in fluid mixtures. However, a previous study conducted by John et al. [103] found that over 90 percent of droplets are distributed around a mean droplet size, with an average error of 3.6%. In the study, they used a particle video microscope to measure water droplet sizea in an oil phase with various mixing conditions. Therefore, in this study it is assumed the droplets have the same diameter. Droplets with different sizes are the other main source of uncertainty in this model. However, the average relative error is low: 10 % and 15 % for Eq. 6.2 and Eq. 6.4, respectively.

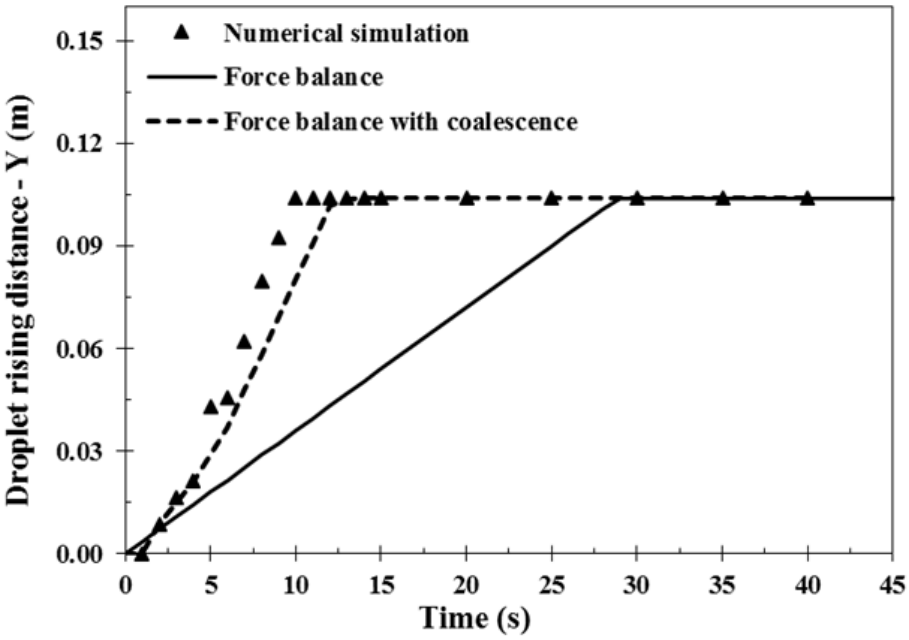
Numerical simulation
Force balance
Force balance with coalescence
Droplet rising distance - Y (m)
0.15
0.12
0.09
0.06
0.03
0.00
0
5
10
15
20
25
30
35
40
45
Time (s)

(a)

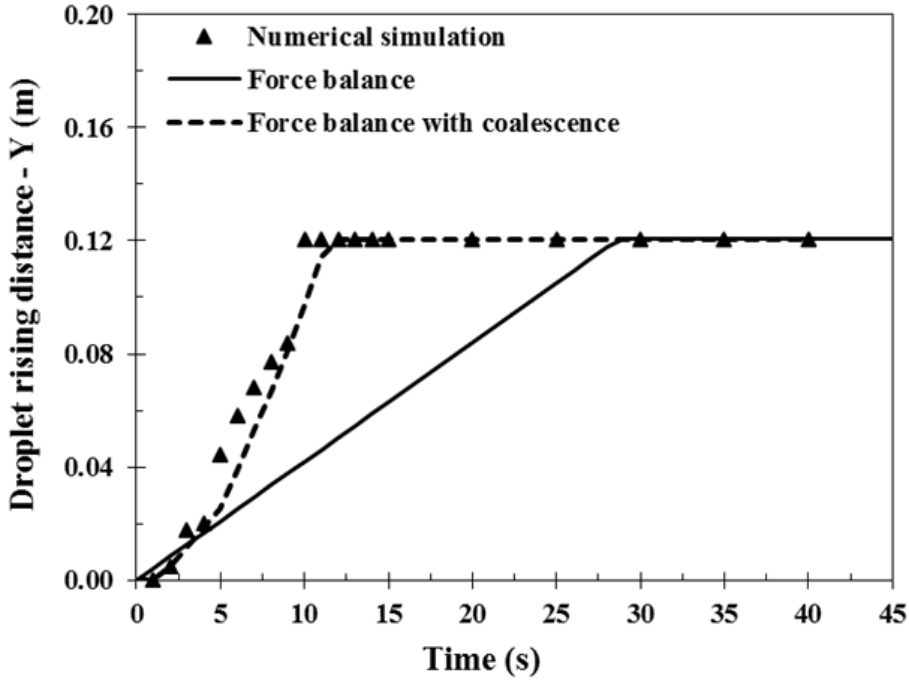
Numerical simulation
Force balance
Force balance with coalescence
Droplet rising distance - Y (m)
0.20
0.16
0.12
0.08
0.04
0.00
0
5
10
15
20
25
30
35
40
45
Time (s)

(b)

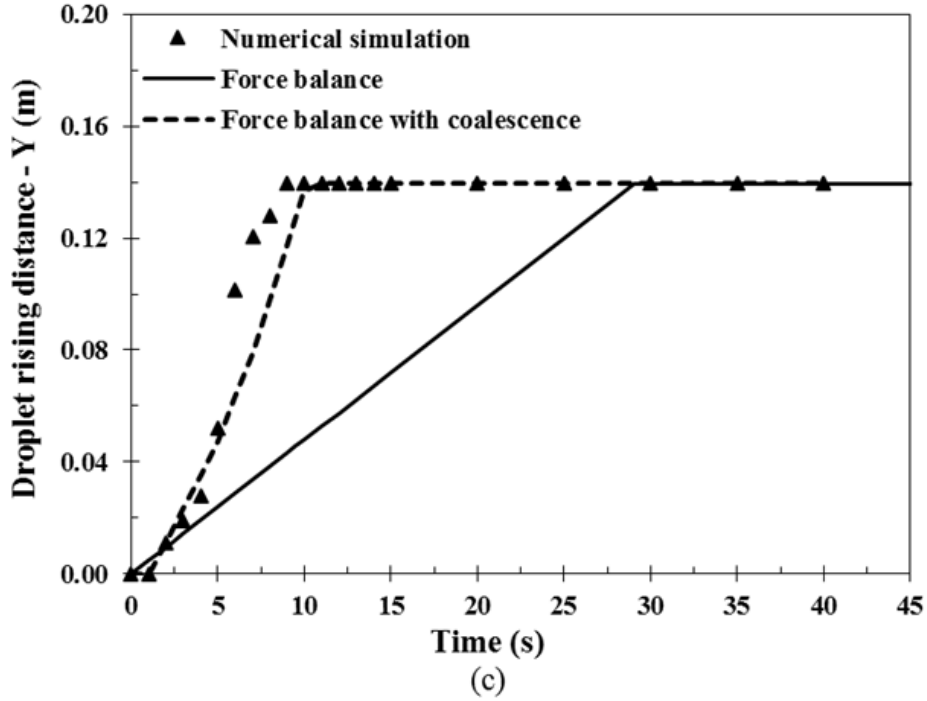

(c)

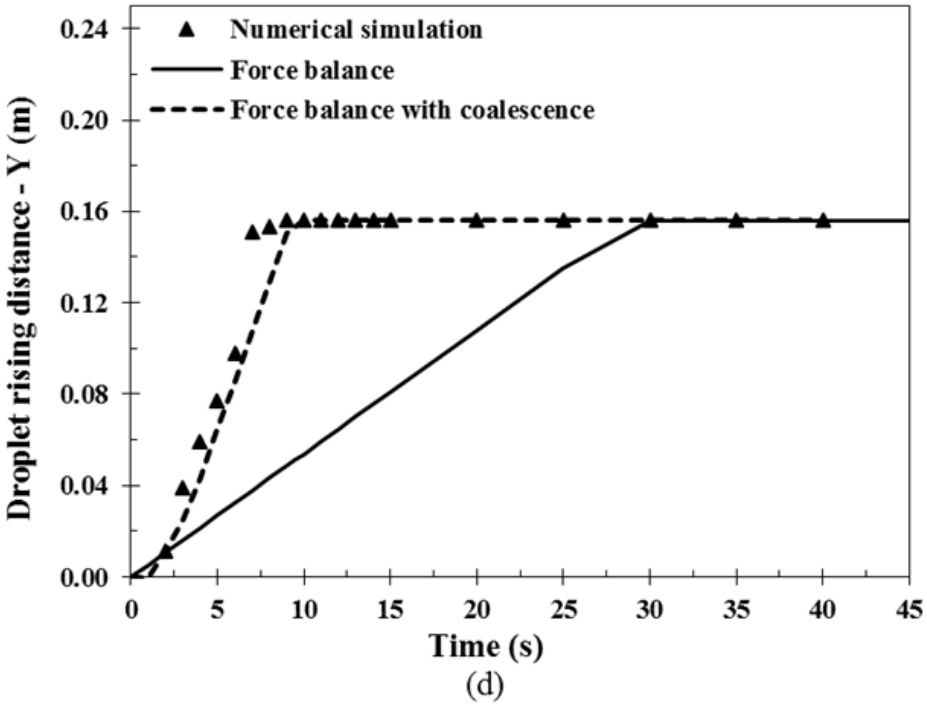

(d)

Figure 6.13: Water droplets in the oil phase coalescence process prediction comparison: (a) oil volume fraction = 0.6. (b) oil volume fraction = 0.7. (c) oil volume fraction = 0.8. (d) oil volume fraction = 0.9.

Table 6.2: Model value calculations

Factors	ε	
	0.25	**0.75**
a	-0.1867	0.02185
b	2.625	-0.21975
c	-2.5	2.5
	$t_{coal}(s)$	
N = 2	2	2
N = 4	5	2
N = 8	6.5	2
N = 16	-	4.6

6.2.3 Coalescence model validation

To validate the model Eq. 6.2 and Eq. 6.4, two numerical simulations were conducted with an oil volume fraction of 0.25 and 0.75, respectively. The value of a, b, and c for each case based on the correlation models and coalescence time based on Eq. 3.41 and Eq. 6.1 are listed in Table 6.2.

The droplet rising distance with time is plotted using models predicted in Eq. 3.43. A comparison of the droplet rising distance with time results obtained from simulation, force balance, and force balance with coalescence, are shown in Figure 6.14 and 6.15. In the oil droplet in water case, $\varepsilon_o = 0.25$, the coalescence time for the first binary step is 2 s; the coalescence time for the second binary step is 5 s; the maximum number of binary steps is 3, which takes 6.5 s for coalescence. The coalescence time increases with the increase of the coalescence step. At this time, the oil droplets are all separated from the water phase. The same trend is also reported by another study [120]. Five simulations were conducted to investigate the relationship between the separation distance between two droplets and coalescence time. Their results show that a higher value of the distance leads to a longer coalescence time.

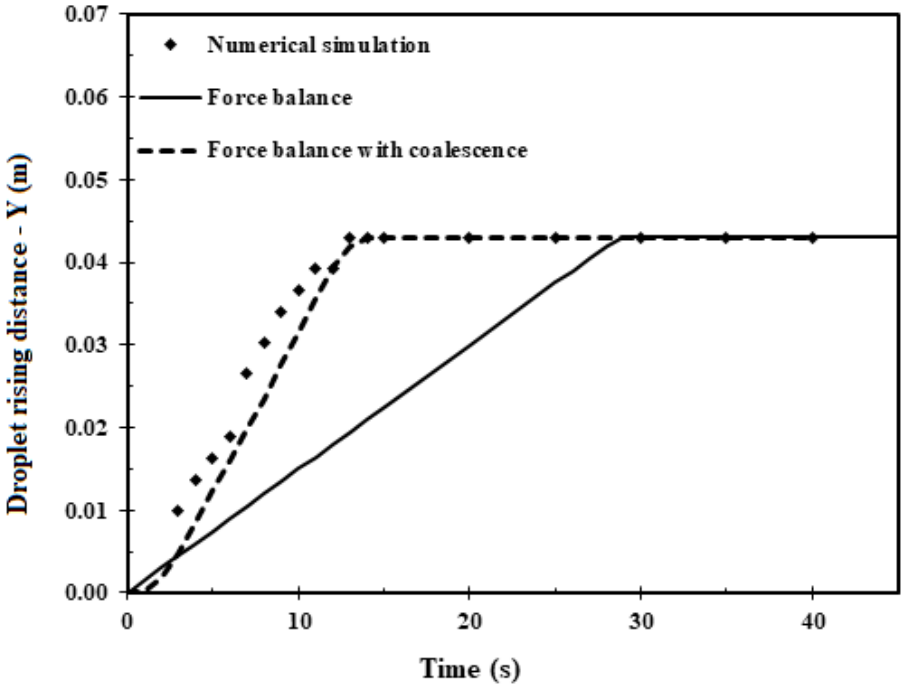

Figure 6.14: Oil droplets in the water phase coalescence model validation: oil volume fraction = 0.25.

There are two possible reasons for this trend. One of the reason is due to the longer approaching time between two droplets. The other reason is due to the less efficient conversion of kinetic energy to surface energy.

Meanwhile, when $\varepsilon_{oil} = 0.75$, the maximum number of binary steps for water droplets is 4. As shown in Figure 6.15, the time needed for droplet coalescence is reduced when compared to the oil volume fraction of 0.25. Validation results show that the proposed binary droplet coalescence model is capable of predicting the liquid / liquid separation process with average relative error for both cases of 6.3 % and 4.8 %, respectively.

The proposed coalescence model only applied force balance with droplet coalescence to predict the separation process. As previous studies have stressed, the droplets coalescence process is a complex process that includes coalescence frequency, coales-

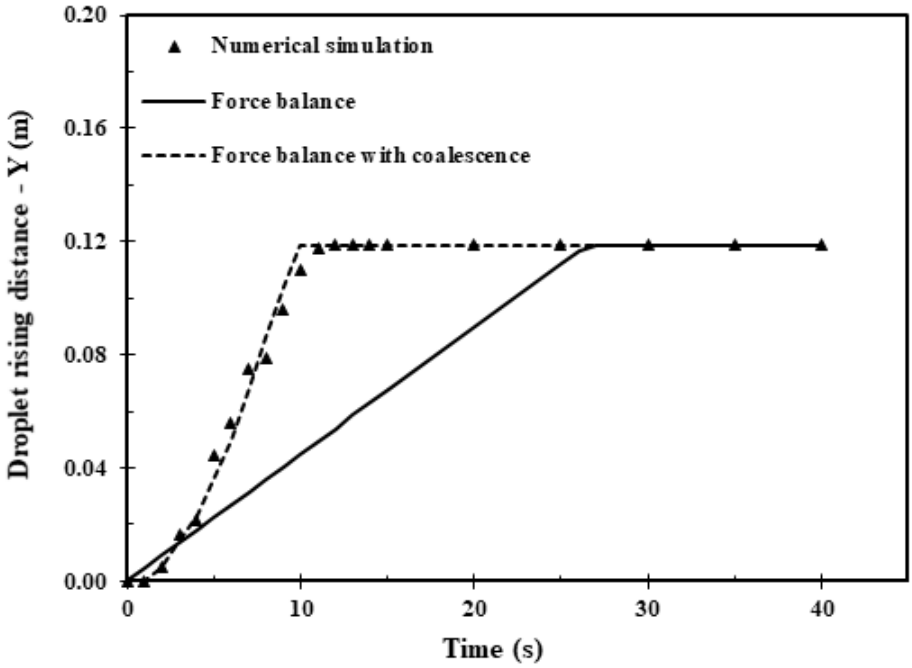

Figure 6.15: Water droplets in the oil phase coalescence model validation: oil volume fraction = 0.75

cence efficiency, and collision frequency. Also, there are several mechanisms that trigger a collision. All these factors contribute to the complexity of the oil / water droplet coalescence process. However, for this model, all these factors are combined into the force balance equation with the binary droplet coalescence process. This combination results in a relatively fundamental separation process compared to other coalescence models. The results of this work provide a useful new tool to predict liquid / liquid separation dynamics.

6.3 Summary

In this chapter, a new correlation was developed to predict droplet coalescence in liquid / liquid separation based on oil volume fraction and binary droplet coalescence. The new correlation has been developed using a numerical method based on a force

balance method in order to predict the separation dynamics of the droplets. The method has an average accuracy of 94.5 % based on the average error of the validation with experimental results. In order to predict the separation process, all the factors associated with the complexity of the oil / water droplets coalescence process are taken into account through the force balance between binary droplet phases. This combination results in a model that is relatively simple compared to other coalescence models proposed in the literature. These results provide a much simpler and more accurate tool to predict liquid / liquid separation dynamics.

Chapter 7

Numerical Simulation: Results and Discussion

This chapter discusses the main results of the numerical simulations. The various operational conditions that can have an effect on oil volume fraction, as well as the separation process with the oil volume fraction and pressure distribution over time, are presented and discussed in this chapter.

The location of the interface layer was used to track the separation process. As shown in Figures 7.1 and 7.2, Location 1 (L1) represents the bottom of the interface layer, which means there is only a water phase under Location 1. Location 2 (L2) represents the top of the interface layer. Dimensionless time (t*) and dimensionless distance (y*) were used to analyze the effect of operating factors on the separation process, as shown in the following equation:

$$t^* = \frac{\nu \cdot t}{{y_t}^2 \cdot \varepsilon_w} \tag{7.1}$$

where, ν is the kinematic viscosity of water in m^2/s, y_t is the theoretical thickness of the multiphase fluid, which represents the height of fluid in the separator, t is the

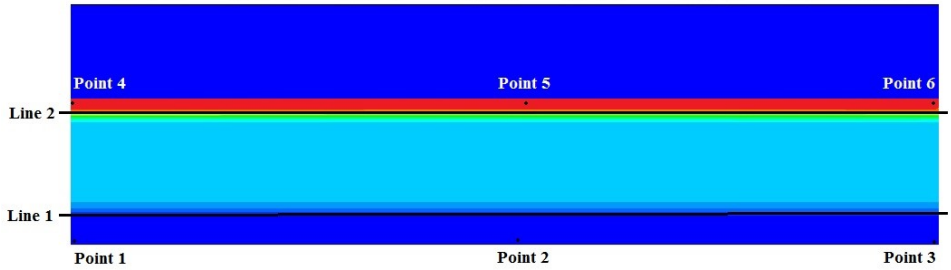

Figure 7.1: Sampling location in computational domain

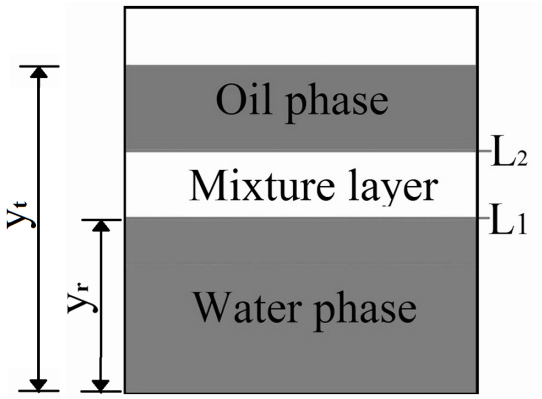

Figure 7.2: The distribution of mixture in the separator

resident time (see Figure 7.2).

The dimensionless distance (y*) is defined in Eq. 7.2:

$$y* = \frac{y_r}{y_t \cdot \varepsilon_w} \tag{7.2}$$

where, y_r is the thickness of the separated water phase at t resident time (see Figure 7.2), ε_w is the water volume fraction. The value of y^* ranges from 0 to 1.

These dimensionless variables are used in this chapter to analyze most of the results from the CFD simulation predictions.

7.1 Validation of the ANSYS Fluent Model

The oil volume fractions for both the experimental study and the simulation study are presented here. The sampling points used here are Point 1, 2, 3 in Figure 7.1 (Page 101). The average value of three points is used to compare with numerical results. The oil volume fraction curve obtained from the numerical simulation model shows a dramatic drop in the oil volume fraction at the very beginning ($t* < 200$) of the operation. The oil volume fraction decreases very slightly when the $t*$ ranges from 650 to 2000.

In this study, two numerical operating conditions with different oil volume fractions were investigated to validate the numerical model. As shown in Figure 7.3 and 7.4, both numerical prediction results generally showed a good agreement with the experimental results. This agreement demonstrates that the numerical model setting is suitable and the numerical prediction results are accurate enough for the other simulation cases. The fundamental operating condition case was selected, where the oil volume fraction was 0.2, the operating temperature was 20 °C, and the inlet flow velocity was 0.0137 m/s. The other operating condition with oil volume fraction was 0.5.

7.2 Numerical Software Simulation Results Accuracy Comparisons

To compare the simulation results among three different commercial CFD software, the same separator geometry used in the experimental investigation, and the same operating conditions as the base case in Fluent were also investigated in Flow-3D and OpenFOAM. That means for all comparable cases, the flow rate is 1.0 GPM, oil

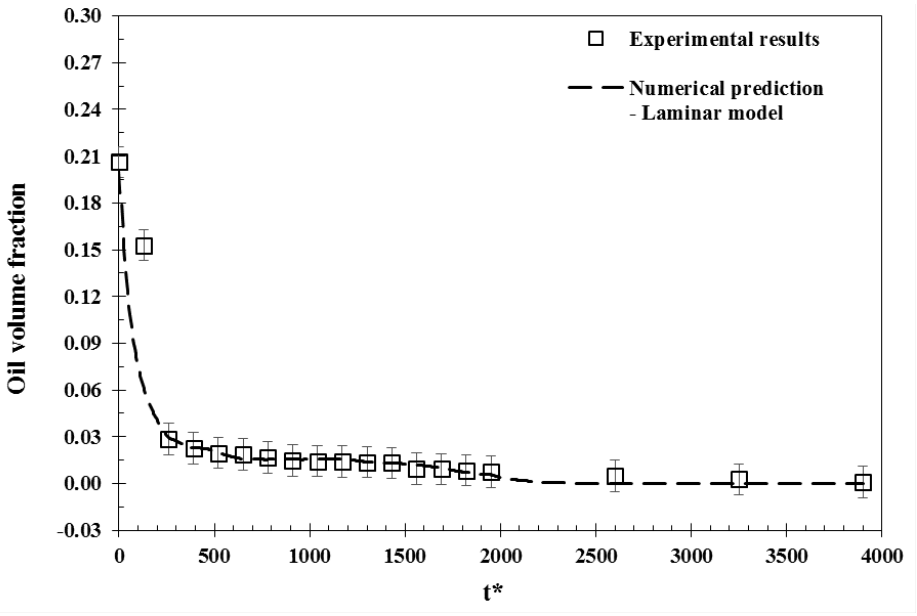

Figure 7.3: Validation of numerical results: Inlet velocity = 0.0137 m/s, $\varepsilon_{oil} = 0.2$, T = 20 °C

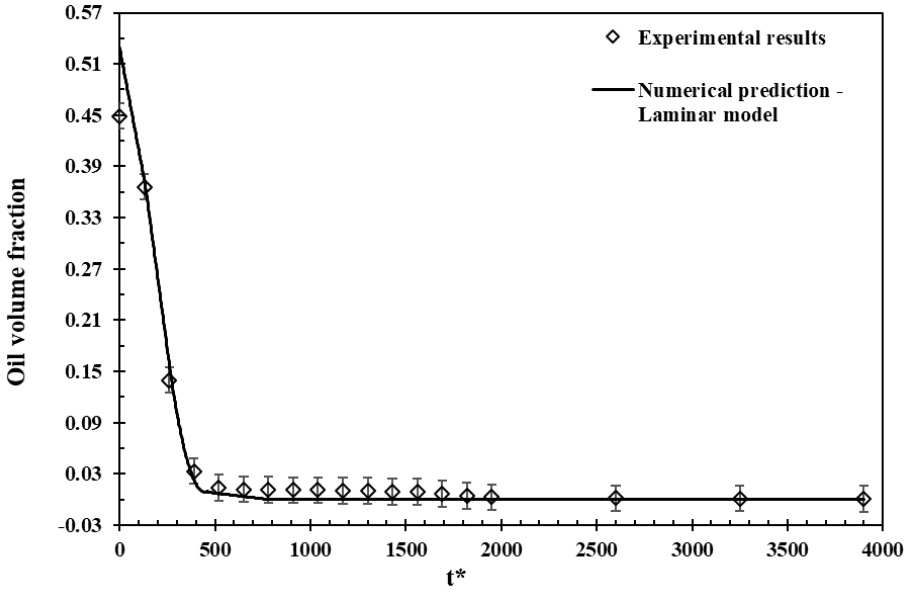

Figure 7.4: Validation of numerical results: Inlet velocity = 0.0137 m/s, $\varepsilon_{oil} = 0.5$, T = 20 °C

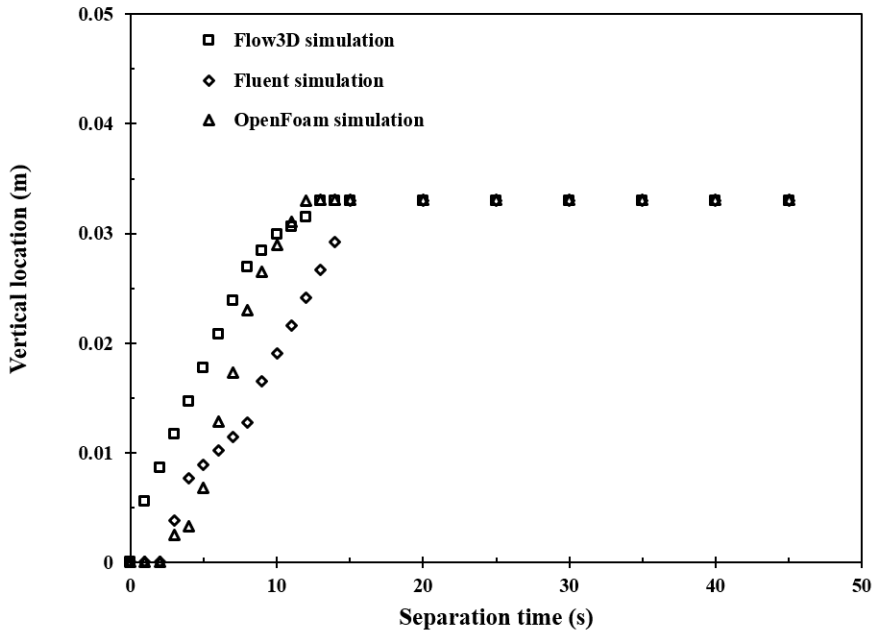

Figure 7.5: Three software comparison for the base case study.

volume fraction is 0.2, temperature is 20 °C, and pressure is 101.325 kPa.

The comparison of results from Fluent, Flow-3D, and OpenFoam is shown in Figure 7.5. In this figure, we can see that the Flow-3D presents the least accurate simulation results. However, the advantage of Flow3D is that it is able to provide approximate results very quickly in terms of computational time. For instance, the computational time for the Base Case using Flow-3D is around 15 min in this study; however, the computational time for Fluent is more than two weeks. The absolute average error between Fluent and OpenFoam results is 16.6 %, which means Fluent provides the most accurate results among the three software packages. Based on these results, all the simulation predictions are using ANSYS Fluent in this study.

The separation processes simulated by Fluent, Flow-3D, and OpenFoam are presented in detail in Appendix D, F, and H, respectively.

7.3 Investigated Cases

The systematic study of operating conditions, including inlet velocity, oil volume fraction, temperature, and pressure, are listed in Table 7.1. All the values in the Base Case are maintained in the experimental study. The minimum oil volume fraction of 0.2 and an inlet velocity of 13×10^{-3} m/s are selected according to the measurement range of the flow meter. A temperature of 20 °C is selected for the Base Case. The separation process operates in atmospheric conditions. For the investigated cases, the ranges of inlet velocity are determined by terminal velocity; oil volume fractions of 0.2, 0.5, and 0.8 are used to create different multiphase flow systems; the range of temperatures and surface tensions were determined by the linear relation in Sydney's [105] study.

For all investigated cases, the selected separation time is 900 s. In the separator design section, 15 min resident time was sufficient for oil droplets to separate from the water phase. The flow is laminar flow with various inlet flow speeds. Also, all simulations use the VOF multiphase simulation model. The simulation process is completed for 900,000-time steps (900 s). The base case involves the same material property and operating conditions as the experimental study. Excluding the base case, all the investigated cases involve modified operational conditions.

For Case 1 and 2, the inlet velocity was set to 0.0274 and 0.0352 m/s. For Case 3 and 4, the oil volume fraction was 0.5 and 0.8. For Case 5, 6, and 7, the temperature was 32, 40, and 50 °C. For Case 8, For Case 9, and Case 10, the operating pressure was 50, 100, and 150 psi. The summarized properties of all the investigated cases are presented in Table 7.1.

Table 7.1: Simulation Cases

Case	Inlet velocity (m/s)	Oil VOF ε_o	Temperature °C	Pressure kPa	Surface tension N/m
Base Case	0.0137	0.2	20	101.325	0.0356
Case 1	**0.0274**	0.2	20	101.325	0.0356
Case 2	**0.0374**	0.2	20	101.325	0.0356
Case 3	0.0137	**0.5**	20	101.325	0.0356
Case 4	0.0137	**0.8**	20	101.325	0.0356
Case 5	0.0137	0.2	**32**	101.325	0.0356
Case 6	0.0137	0.2	**40**	101.325	0.0356
Case 7	0.0137	0.2	**50**	101.325	0.0356
Case 8	0.0137	0.2	20	**344.738**	0.0356
Case 9	0.0137	0.2	20	**698.476**	0.0356
Case 10	0.0137	0.2	20	**1,034.214**	0.0356
Case 11	0.0137	0.2	20	101.325	**0.0365**
Case 12	0.0137	0.2	20	101.325	**0.0389**

7.4 Impact of Various Operating Conditions

This section discusses the numerical simulation results predicted by Fluent.

7.4.1 Effect of oil volume fraction

Variations of oil volume fraction have an impact on the viscosity and density of the mixture, which affects the flow conditions in the separator and further influences the separation process. The mixing system can be divided into two systems with the oil volume fraction is 0.5. When the oil volume fraction is less than 0.5, the mixture is defined as oil droplets in the water system, and the water phase as continual phase; however, when the oil volume fraction is more than 0.5, water is the dispersed phase, and oil is the continuous phase. Figure 7.6 presents the contour plot of oil volume fraction at resident time t = 900 s, which provides sufficient residence time for the dispersed phase to reach its maximum separation efficiency. Figure 7.6 illustrates the contours of oil volume fraction for the fluid, after separation, for three different initial ε_o. In addition, since the separation process reached its maximum separation efficiency, Figure 7.6 cannot show the effect of various initial ε_o on the separation process; therefore, the variation of y* with t* are presented in Figure 7.7.

As illustrated in Figure 7.7, the transient location of y* is slightly affected by the oil volume fraction. When the oil volume fraction ranges from 0.2 to 0.5 (oil droplets are dispersed in the water phase), an increased oil volume fraction requires more time for L2 (location of L2 (top of the interface layer, see Figure 7.1)) to reach the same y* location. The same trend applies to water droplets in a continuous oil phase (when the oil volume range is 0.5 - 0.8). Also, when the oil volume fraction is 0.8, the mixture is defined as water droplets in a continuous oil phase, which means the dispersed phase (water) had the same volume fraction as the oil volume fraction (0.2).

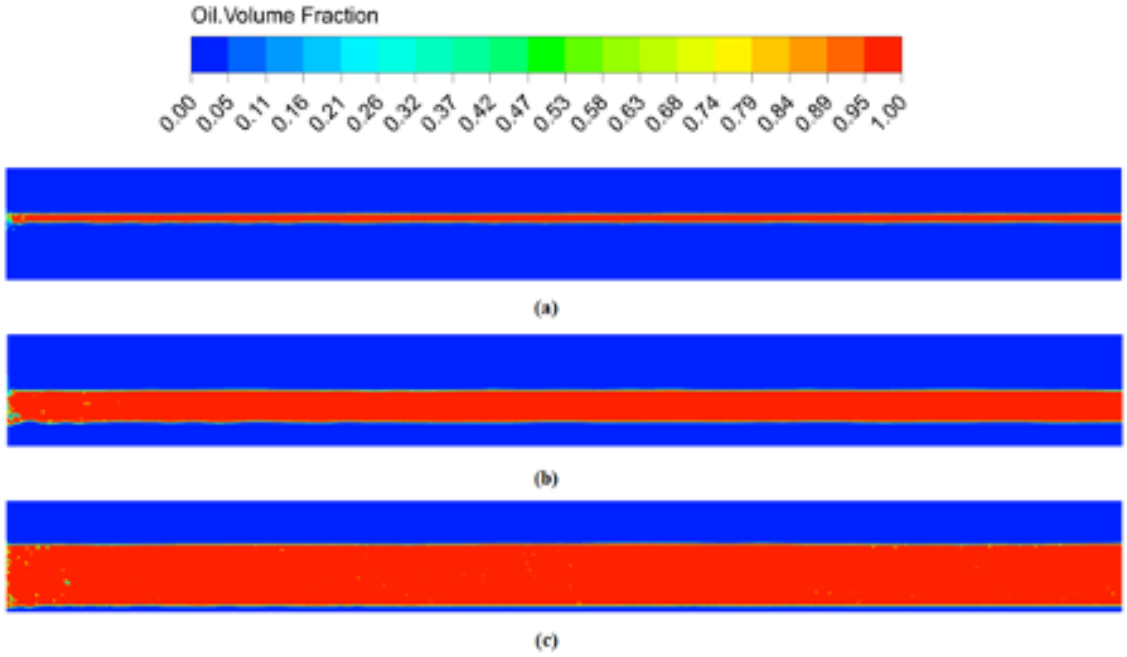

Figure 7.6: Contour plots of oil volume fraction: (a) $\varepsilon_o = 0.2$, (b) $\varepsilon_o = 0.5$, (c) $\varepsilon_o = 0.8$

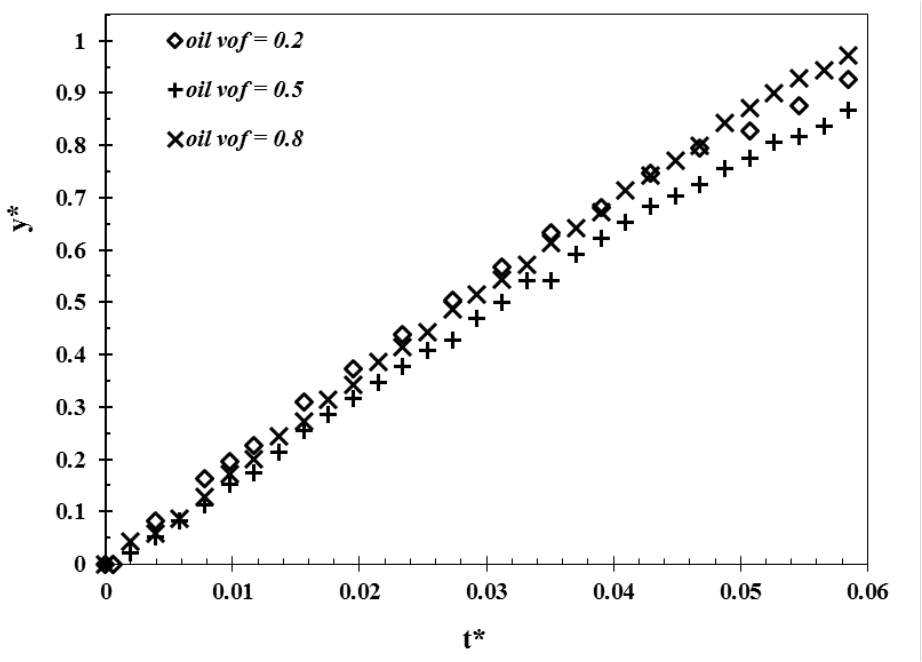

Figure 7.7: Impact of oil volume fraction (vof) on separation efficiency

7.4.2 Effect of temperature

The operating temperature is also a major factor for oil / water separation, as it affects the thermophysical properties of oil and water, such as density and viscosity. Four different operating temperatures between 20 and 50 °C were investigated. As illustrated in Figure 7.8, increasing temperature increases initial separation speed by reducing the oil viscosity; hence, increasing the oil droplets rising velocity. However, in Figure 7.8, the curves values overlap for t*>0.4. This phenomenon suggests that with enough resident time, the oil / water separation efficiency is independent of temperature. According to droplet force balance, droplet diameter is the critical factor that controls the droplet rising velocity, which is independent of operating temperature. Therefore, the effect of temperature is not significant for the overall oil / water separation. The overlapped curves also indicated that when the resident time is 900 s, investigation cases 5 to 7 share the same oil volume fraction distribution as the Base Case. The oil volume fraction contour plot of the Base Case, as shown in Figure 7.6 (a).

7.4.3 Effect of operating pressure

Operating pressures of 101.325, 344.738, 689.476, and 10134.214 kPa are investigated. Since the pressure distribution is the same in the horizontal direction, it only changes in the vertical direction; therefore, a cross-sectional area is selected to demonstrate the contour plot of pressures fields, as presented in Figure 7.9. All four investigated cases present a similar pressure distribution trend that the bottom of the separator has the highest pressure, and the top has the lowest pressure. This is because the density of water is higher than the density of oil, as the maximum separation efficiency is approached, the water phase formed at the bottom, with a relatively higher pressure

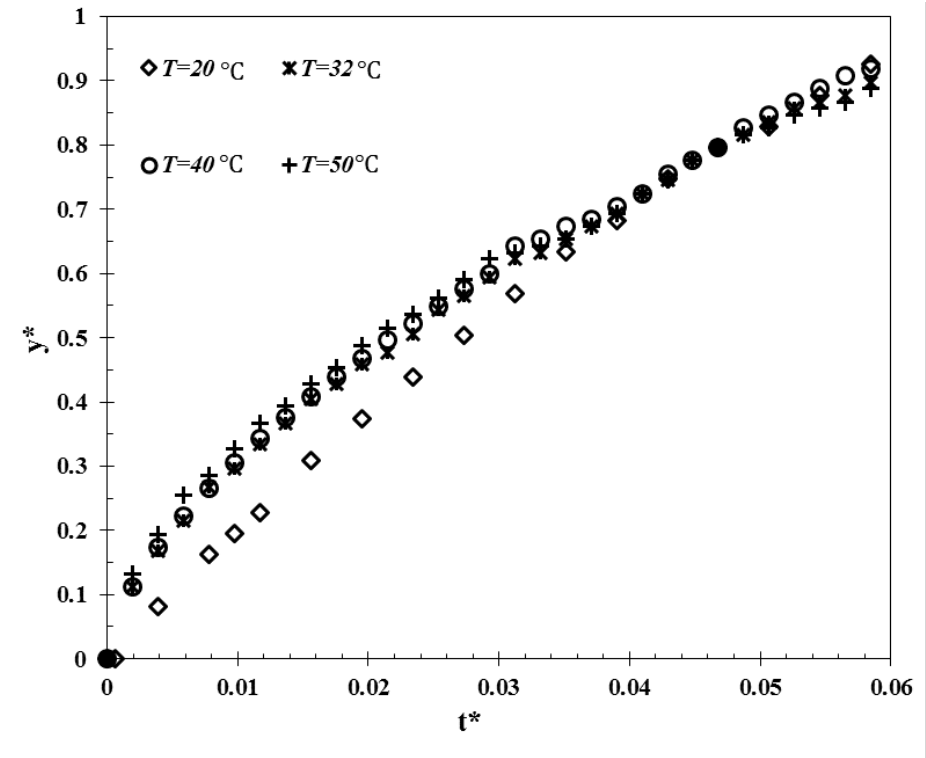

Figure 7.8: Impact of temperature on separation efficiency

than the oil phase at the top. The effect of operating pressure on the separation process is presented in Figure 7.10. The slope of the curves decreases with increasing operating pressure, which means that separation speed decreases with pressure. As illustrated in Figure 7.10, to reach the same height (y*=0.3), t* needs to be 0.016 and 0.025 for the operating pressure of 101.325 kPa and 1034.214 kPa, respectively. This indicates that increased pressure can significantly increase the time to separate oil from water. The reason for increasing the separation time is because a high pressure limits the oil droplet rising velocity. Also, the effect of pressure on separation declines as pressure increases. When pressure is over 689.476, the pressure effects on y* can be neglected, which is confirmed by comparing the results of pressure 689.476 and 1,034.214 kPa in Figure 7.10. The vertical distance between lines is reduced until they almost overlap with each other.

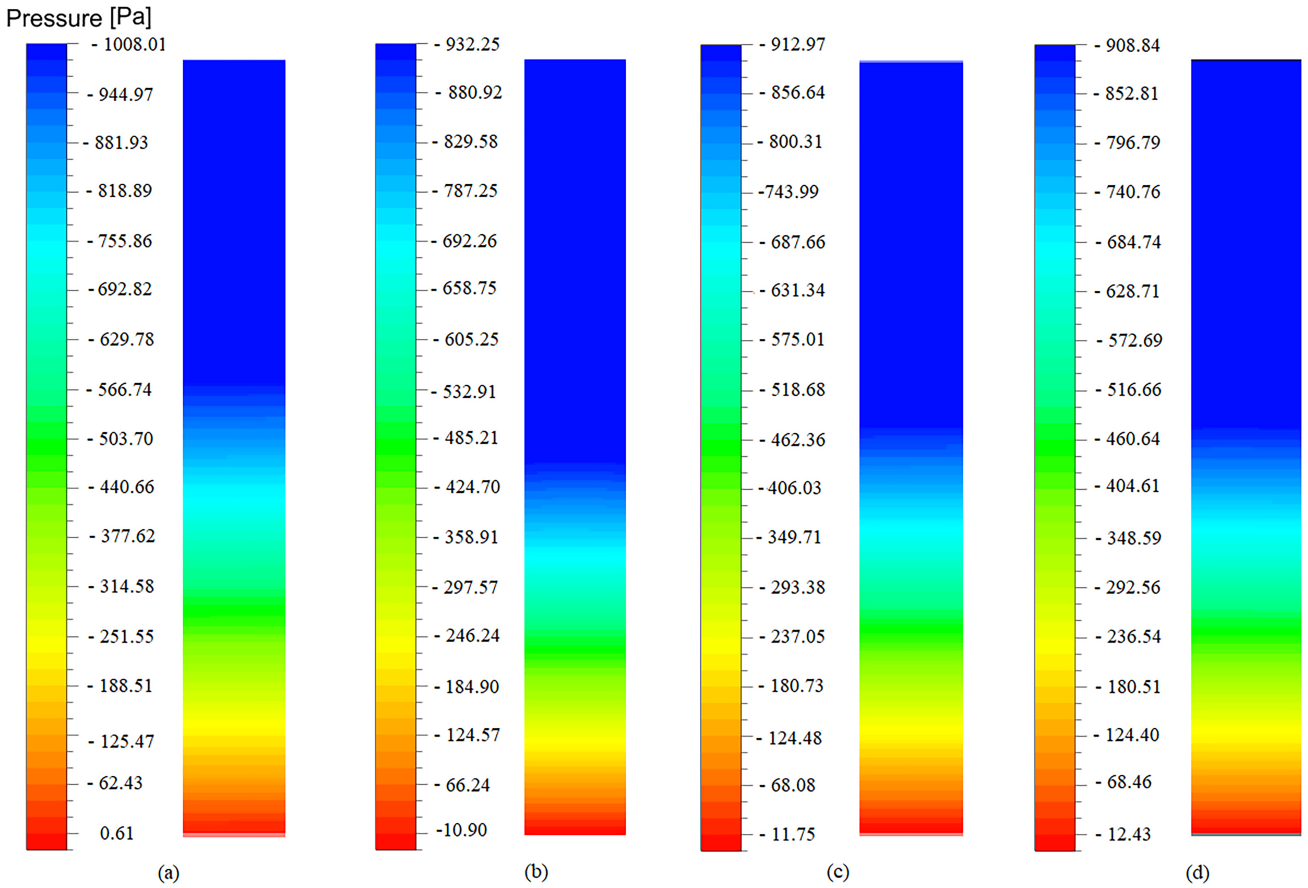

Figure 7.9: Contour plots of pressure distribution: (a) P = 101.325 kPa, (b) P = 344.738 kPa, (c) P = 689.476 kPa, (d) P = 1034.214 kPa

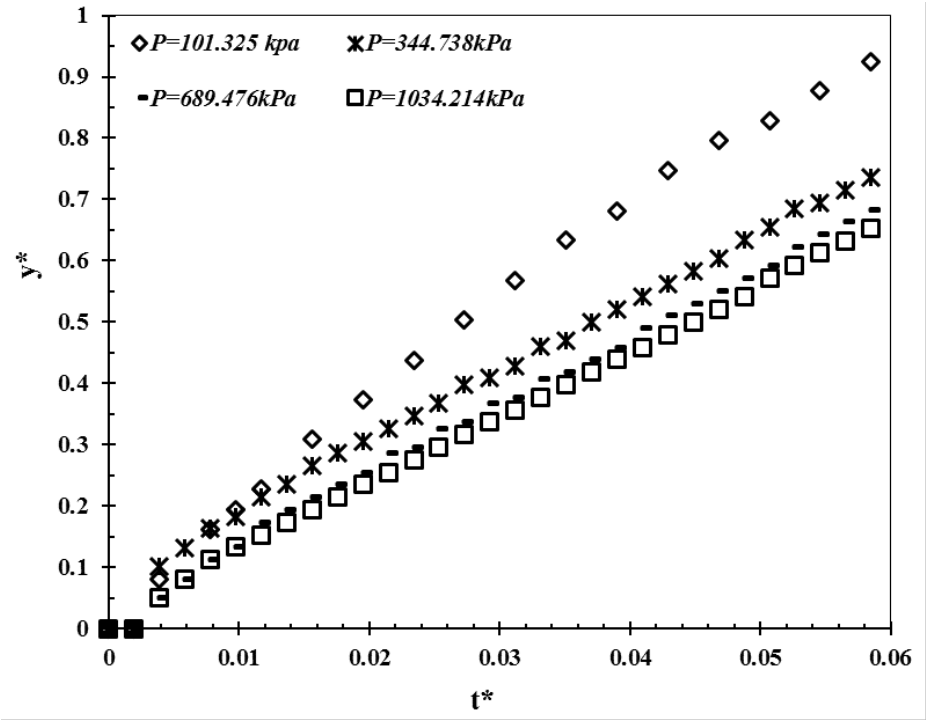

Figure 7.10: Impact of pressure on separation efficiency

7.5 Oil volume fraction contour and velocity vector

The oil volume fraction in the water phase is presented in this section. Due to the fact that the top area of the separator only has the air phase, with no oil or water phase, the oil volume fraction is zero. To understand the distribution feature of the separation process, the contour of the oil volume fraction in separator Zone 2 at 300, 600, and 900 s is shown in Figure 7.11. There is a region where the separated oil phase was moved vertically but firmly upward, and the thickness of the separated phase increases with time, as presented in Figure 7.11. The maximum oil volume fraction in the oil phase is 0.98. As the separation process starts and continues, the water volume fraction in the bottom layer increases as the oil volume fraction decreases with time. In the top layer, the oil volume fraction increases while the water volume fraction decreases. Thus, the

separated water phase and oil phases form in the separator. Also, the oil volume fraction distribution results show that there is a mixed zone in the entrance where the oil volume fraction is relatively low compared to the same vertical location of the rest of the separator. This is because the oil volume fraction in this mixture is 0.2, which is relatively lower than the volume in the separated phase. When the mixture combines with the separated oil phase at the entrance, it results in the divergence of the oil volume fraction in that area.

The fluid velocity vectors at Zone 1 are shown in Figure 7.12. The evaluation of the mixing properties at different times has been restricted to the visual observation of the velocity profiles. To obtain a clear and detailed velocity vector, considering the size of Zone 2, only 1/8 of the length of Zone 2 was chosen. The fluid was dispersed at the bottom of the separator, where oil droplets start to rise because of the buoyancy effect. The general flow patterns for the configurations presented high velocities at the inlet. At t = 300 s, as the flow reaches the bottom, the velocity drops significantly. In Zone 2, oil droplets move with constant velocity, which follows Stokes' law.

As the filling process continues, at t = 600 s, the fluid level inside the tank rises; therefore, there is a small mixing zone near the inlet due to high relative velocity. The velocity drops back to the terminal velocity after the mixing zone. The mixing zone area becomes more significant when the fluid level is close to the same vertical height as the vertical location of the inlet pipe, as shown when t = 900 s in Figure 7.12. Also, a minimal vortex zone is obtained when t = 900 s, which are similar to the previous simulation of hydrodynamic characteristics, presented by Behin and Bahrami [45] which used a small-scale three-dimensional separator to model the flow pattern through the separation process. Mixing zone, plug zone, and dead zone were defined according to the velocity vector in their study. Their results also proposed that an increase in the inlet flow rate results in an increase in mixing zone volume.

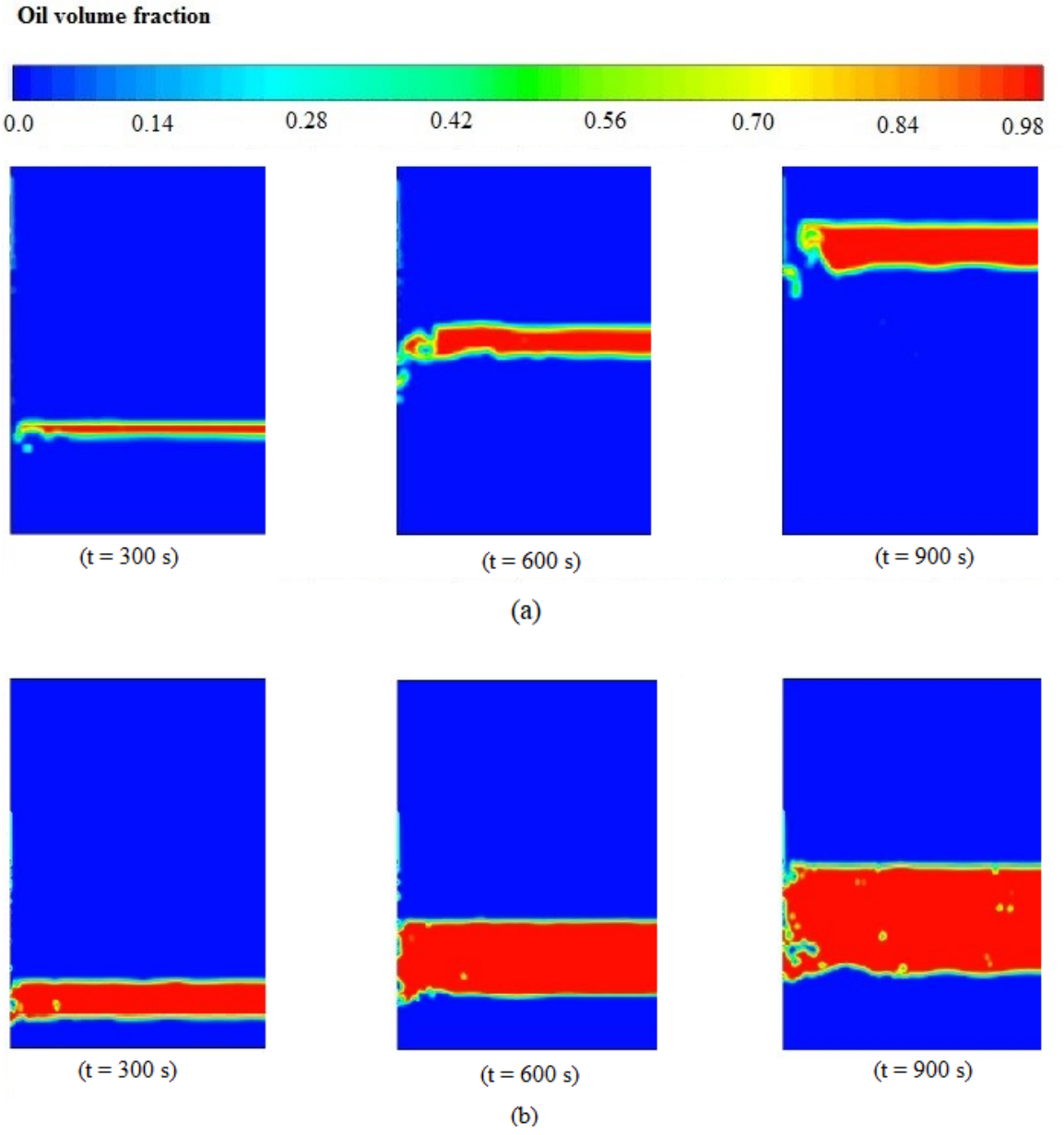

Figure 7.11: The contour of oil volume fraction: (a) Initial oil volume fraction = 0.2 (b) Initial oil volume fraction = 0.5

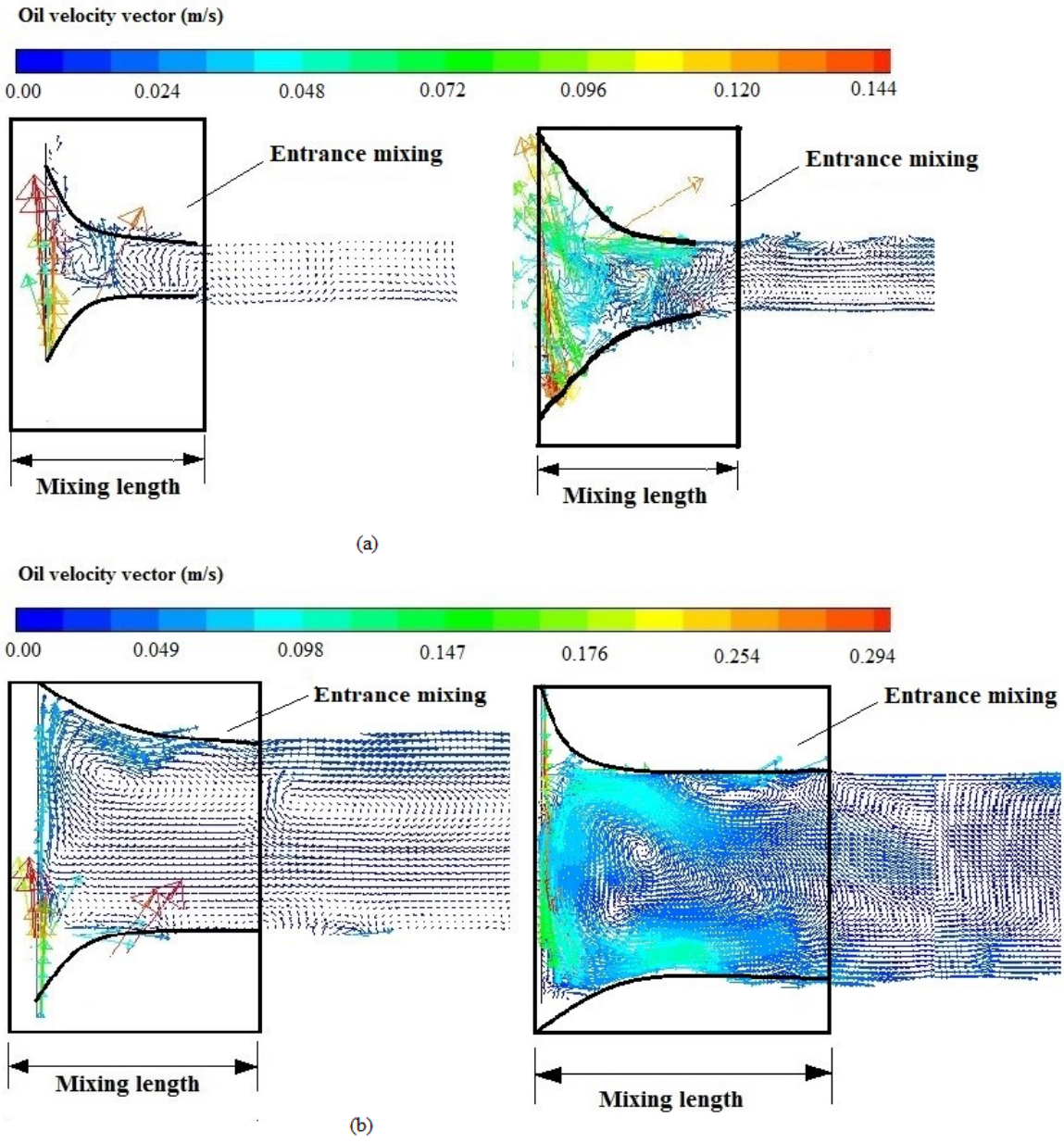

Figure 7.12: Velocity vector : (a) Initial oil volume fraction = 0.2, left: $v = 0.0137m/s$, right: $v = 0.0274m/s$ (b) Initial oil volume fraction = 0.5, left: $v = 0.0137m/s$, right: $v = 0.0274m/s$

However, the main objective is to estimate the trends of the flow behavior in Behin and Bahrami's study [45], such as the percentage of mixing zone volume and dead zone volume.

7.6 Effect of the velocity on the mixing length

There is a mixing zone formed at the entrance of the inlet, as shown in Figure 7.11. The mixing length depends on the inlet velocity. Therefore, the velocity effect on the mixing length is investigated in this section. The velocity simulation cases are listed in Table 7.2, and divided into three regions. Region 1 is when the inlet velocity is less than 0.1 m/s, Region 2 is when the inlet velocity is between 0.1 and 0.5 m/s, and Region 3 is when the inlet velocity is between 1.0 and 2.0 m/s. The data is taken from Line 2 in Figure 7.1. The mixing length was determined by the average horizontal length over different times when the oil volume is 1.

The results and comparison of the inlet velocity effect on mixing length are presented in Table 7.2. Increasing the inlet velocity increases the mixing length. In Region 1, the Re number of the fluid in the separator is less than 20, and the oil / water multiphase fluid is in the laminar range. One of the characteristics of laminar flow is that the fluid moves relatively slowly, and the inlet velocity has little impact on the overall flow. Fluid velocity varies in Region 2, where the Re number of the fluid in this area is $50 < \mathrm{Re} < 150$. The multiphase flow in the separator is still a laminar flow. However, the mixing length is doubled due to the increase in inlet velocity. In Region 3, the Re number of the fluid in the separator ranges from 500 to 1000, which means fluid in the separator is in the transient range.

As shown in Table 7.2, the mixing length increases sharply from Region 1 to Region 3. The main reason is that oil droplets increase inlet velocity as the droplet

Table 7.2: Impact of inlet velocity on mixing length

Region	Cases	Velocity (m/s)	Mixing length $l_m(m)$	Percentage l_m/L(%)
Region 1	Case 1	0.0137	0.028	1.57
	Case 2	0.0274	0.099	5.57
	Case 3	0.0374	0.29	16.3
Region 2	Case 4	0.105	0.555	31.2
	Case 5	0.274	0.639	35.9
Region 3	Case 6	1.05	1.40	78.8
	Case 7	1.5	1.42	79.9
	Case 8	1.75	1.56	87.8

horizontal velocity increases. In the same separation time, oil droplets move further. This results in a longer mixing length.

7.7 Summary

In this chapter, simulation results were also validated by the experimental results under the same operating conditions for oil / water separation efficiency. The studies of different CFD software results show that Fluent presents the most accurate predictions. Thus, more CFD modeling used the Fluent software to simulate the dynamic fluid effects in a gravity separator. Further, detailed simulations were performed to study oil / water separation in a filling process.

Also, oil volume fractions and the velocity vector distribution in the separator were investigated. Both of the results show that there was a mixing zone located at the entrance, which has a relatively lower oil volume fraction and a higher velocity. In addition, this study analyzed the inlet velocity's affect on the mixing length, and

the results show that it was closely related to the inlet velocity. When the fluid in the separator was in the laminar region, the mixing length was less than 40 % of the total separator length; however, increasing the inlet velocity until the fluid in the separator was in the transient region, results in the mixing length occupying 90 % of the total separator length.

Chapter 8

Predictive Correlation of Oil / Water Separation

In this chapter, the numerical prediction results and the investigation of the relationship of the selected dimensionless groups are discussed. The relationship between the dimensionless groups, Re number, Eu number, and We number is determined under the same separation efficiency value at the outlet. The correlation is presented and analyzed using nonlinear regression on the x-y Cartesian coordinate system. Manual iterations are performed to determine the coefficients in the general correlation relationship.

A study of operation conditions, including inlet velocity, oil volume fraction, temperature, and pressure, are listed in Table 8.1. With the same operating conditions, the results of the Base Case and Case 0 are compared with experimental results to validate the simulation model of this numerical study.

Table 8.1: Summary of Simulation Cases

Case	Inlet velocity (m/s)	Oil vof	Temperature °C	Pressure kPa	Surface tension (N/m)	Viscosity model
Base Case	0.0137	0.2	20	101.325	0.0356	Laminar
Case 0	0.0137	0.2	20	101.325	0.0356	**Turbulent**
Case 1	**0.0274**	0.2	20	101.325	0.0356	Laminar
Case 2	**0.0374**	0.2	20	101.325	0.0356	Laminar
Case 3	0.0137	**0.5**	20	101.325	0.0356	Laminar
Case 4	0.0137	**0.8**	20	101.325	0.0356	Laminar
Case 5	0.0137	0.2	**32**	101.325	0.0356	Laminar
Case 6	0.0137	0.2	**40**	101.325	0.0356	Laminar
Case 7	0.0137	0.2	**50**	101.325	0.0356	Laminar
Case 8	0.0137	0.2	20	**344.738**	0.0356	Laminar
Case 9	0.0137	0.2	20	**698.476**	0.0356	Laminar
Case 10	0.0137	0.2	20	**1,034.214**	0.0356	Laminar
Case 11	0.0137	0.2	20	1,034.214	**0.0356**	Laminar
Case 12	0.0137	0.2	20	1,034.214	**0.0389**	Laminar

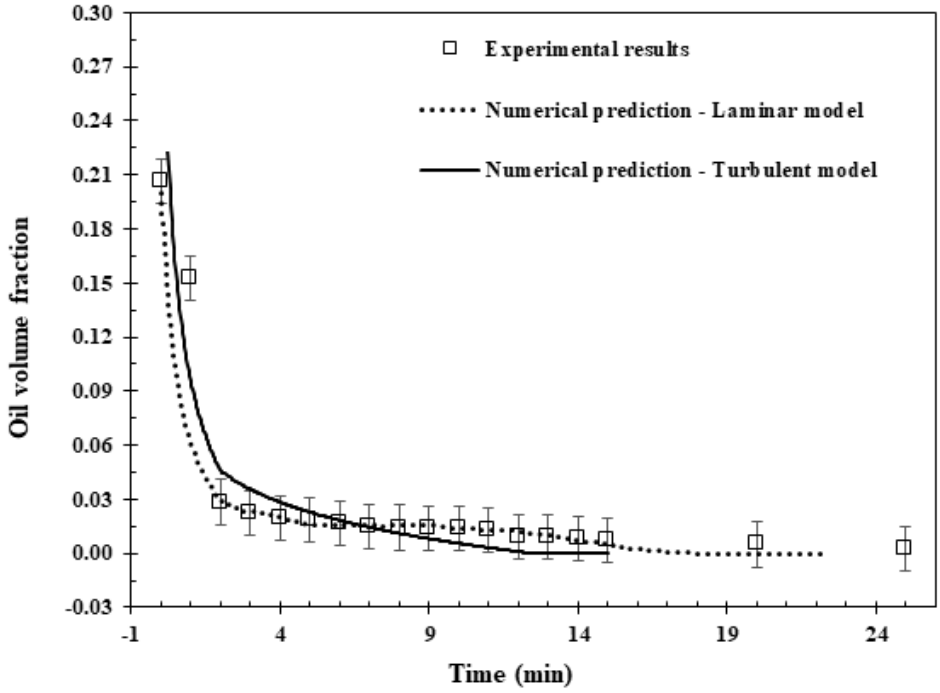

Figure 8.1: Comparison between experimental data and model predictions for the base case

8.1 Validation of the CFD Model

Two numerical prediction methods using a turbulent model and a laminar model, were compared with the experimental results to obtain the more precise method for this study. The oil volume fraction curve obtained from the numerical simulation model showed a dramatic drop in oil volume fraction at the very beginning (first two minutes) of the operation. The oil volume fraction decreased very slightly from 5 minutes to 15 minutes. After 15 minutes, the separation process reached a steady-state process. As illustrated in Figure 5, the trend of the oil volume in water for the CFD simulation study was similar to the experimental results, with an mean error of 2.76 %, and the maximum error of 7.54%.

If the fluid in the separator is laminar, the flow in the separator can be treated as an open channel flow. For open channel flow, the Reynolds number is defined as

$Re = \frac{UR_H}{\nu}$, where, $R_H = \frac{A}{P}$. The Reynolds number in the Base Case is between 5 and 75. Therefore, the oil / water flow in the separator is laminar.

8.2 Correlation Model Development

The numerical prediction results and the investigation of the relationship of the selected dimensionless groups are discussed in this section. The relationship between the dimensionless groups is determined under the same separation efficiency value at the outlet. The correlation is presented and analyzed using nonlinear regression on the x-y Cartesian coordinate system. Manual iterations are performed to determine the coefficients in the general correlation relationship. The simulation data are analyzed and plotted to calculate the constants in Eq. 8.1.

$$\frac{x}{h} = C \cdot \left(\frac{h \cdot v \cdot \rho_m}{\mu}\right)^{n_1} \cdot \left(\frac{P}{v^2 \cdot \rho_m}\right)^{n_2} \cdot \left(\frac{h \cdot v^2 \cdot \rho_m}{\sigma_{o/w}}\right)^{n_3} \tag{8.1}$$

8.2.1 Reynolds number (Re)

Correlation of the Reynolds number is created by varying the inlet velocity, density, and viscosity of the mixture, and the Reynolds number in a range of $5 \leqslant \mathrm{Re} \leqslant 75$. The viscosity is changed by using different oil volume fractions (ε_o), as seen in Eq. 3.47 and 3.48. The correlation development of Π_1 as a function of the Re number is shown in Figure 9. The exponent correlation for the relationship between Π_1 and Re term is 0.1915, with an R-squared of 0.9188. The Reynolds number has a direct correlation with the separator geometry design; thus, an increase in Re requires a separator with a larger length to height ratio.

The results are shown in Figure 8.2 indicate that the required separator size increases with Re. This behavior is in line with our expectation of the effect of Re on

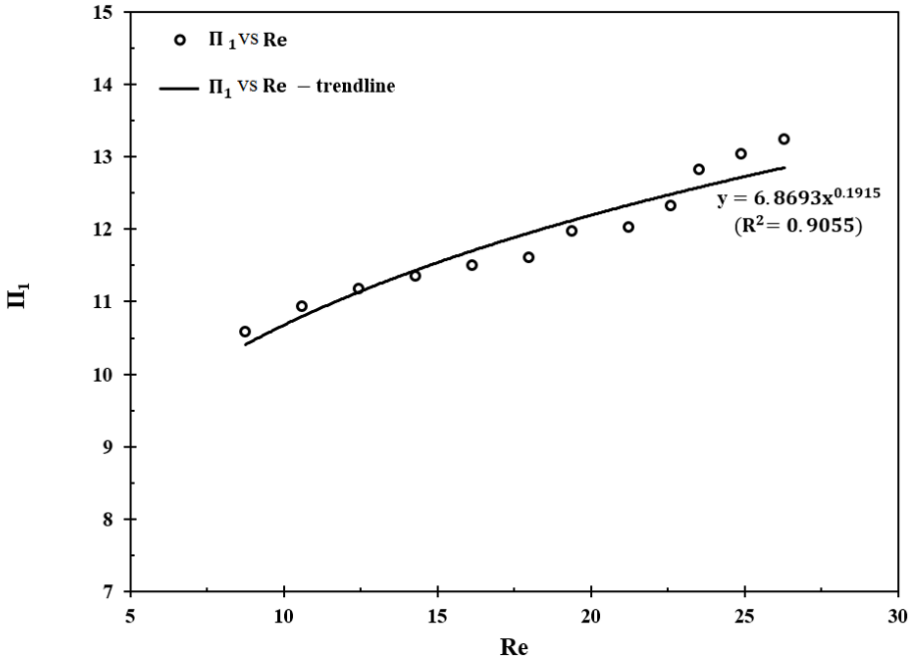

Figure 8.2: The effect of Re number on separator size design

oil/water separation efficiency. As the Re number increases, i.e., the importance of the viscous force with respect to the inertial forces increases, the separation efficiency decreases. Therefore, a bigger separator is required to maintain the same separation efficiency. These results are only for low Re numbers, where the fluid is in the laminar region. For small Re numbers, Rieber and Frohn [121] conducted a simulation study to analyze the droplet collision behavior. Collision frequency decreases with the increase of the Re number in this regime. One of the reasons for this phenomenon, according to Rieber and Frohn, is that the initial kinetic energy dissipates after the collision of the two droplets. These simulation results were also validated by the experimental study conducted by Qian and Law [122].

8.2.2 Euler number (Eu)

The Eu number represents the ratio of the pressure forces to the internal forces, which is used for analyzing fluid flow dynamics where the pressure is important. In this study, the correlation between separator geometric design and pressure is investigated based on the Euler number. The exponent of the correlation shown in Figure 8.3 indicates that the operational pressure has a direct correlation with separator geometry, i.e., increasing the operating pressure requires a separator with a larger length to height ratio. The reason for this trend is that the Euler number is a dimensionless group that represents the ratio of pressure forces to inertial forces; thus, for a higher Euler value, a larger separator geometry is required to main the same separation efficiency. Luiz et al. [123] found a similar effect of Euler number on the hydrocyclone separator. In the study, to achieve the separation duty, the energy cost of the separator increases with an increase in Euler number.

The correlation developed for Euler number is in the range $0 \leqslant \text{Eu} \leqslant 6.0 \text{ x } 10^6$. In this range, the new Euler number correlation presents a high accuracy; as shown in Figure 8.3, the R-square is 0.9055. According to the correlation, the value of n_2 is 0.235.

8.2.3 Weber number (We)

The Weber number is mainly used for studying the interface between two fluid, such as oil and water interface. The developed correlation of the Weber number presents a negative exponent with separator geometry, as illustrated in Figure 8.4. The value of n_3 is -0.214, with R-square of 0.9768. The negative exponent relationship means that the required separator size decreases with the Weber number. In an oil / water mixture, the surface tension determines the shape of oil droplets in the water. When

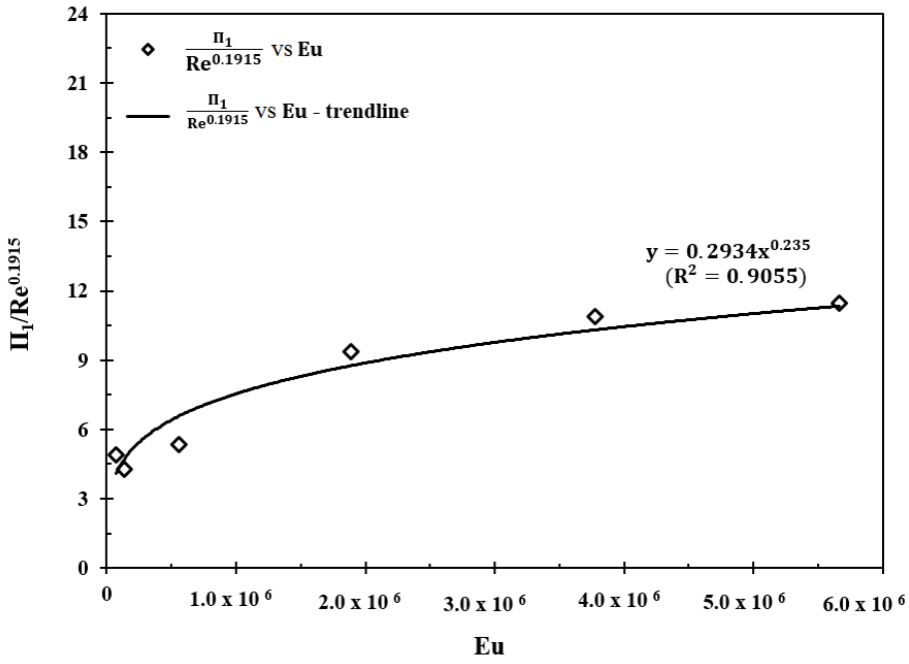

Figure 8.3: The effect of Eu number on separator size design

a surface tension gradient is generated between interfaces, it increases the pressure in the space between them, which results in the increase of oil/water separation efficiency. Therefore, a separator with a smaller length to height ratio is sufficient to maintain the same separation efficiency. The correlation developed in the range $0 \leqslant \text{We} \leqslant$. According to the results in this study, when the Weber number is less than 3, the higher oil / water interfacial tension leads to greater droplet collision efficiency, which improves the separation efficiency and requires a separator with a smaller length to height ratio. The experiment of Jiang et al. [124] investigated the coalescence behavior of droplets. In their study, they found that increasing the Weber number increases the coalescence efficiency, thus improving the separation efficiency. This, in turn, requires smaller separator size to maintain the same separation efficiency. Similar effects of Weber number on the droplet breakup process are also confirmed by Jain et al. [125]. Their study found that at a low range of Weber number ($\text{We} < 12$), droplet breakup

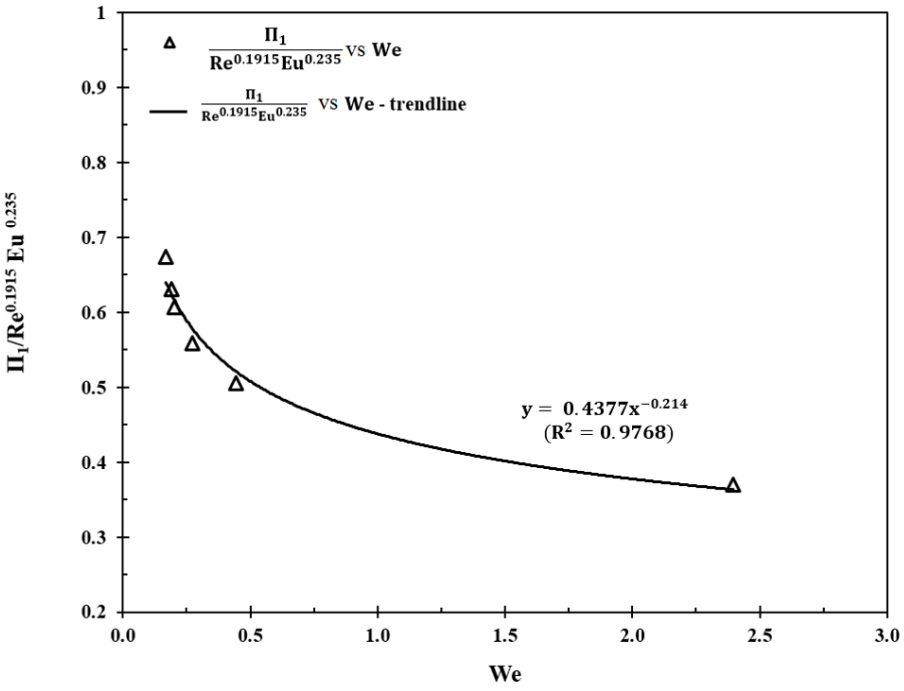

Figure 8.4: The effect of We number on separator size design

speed is decreased with the increase of Weber number.

In order to create a correlation with better accuracy, a larger R^2 value is used, and the second manual iteration was conducted. The values of n_1, n_2, n_3, and C were calculated with respect to the numerical simulation results. The improved correlations are listed in Table 8.2. The minimum value of R^2 increased by 8.3% to a value of 0.9807.

Table 8.2: The comparison of two iteration values

Constants	**First manual iteration**		**Second iteration**	
	Exponent	R^2	Exponent	R^2
n_1	0.1915	0.9055	0.4055	0.9807
n_2	0.235	0.9788	0.2383	0.99968
n_3	-0.214	0.9768	-0.232	0.9868

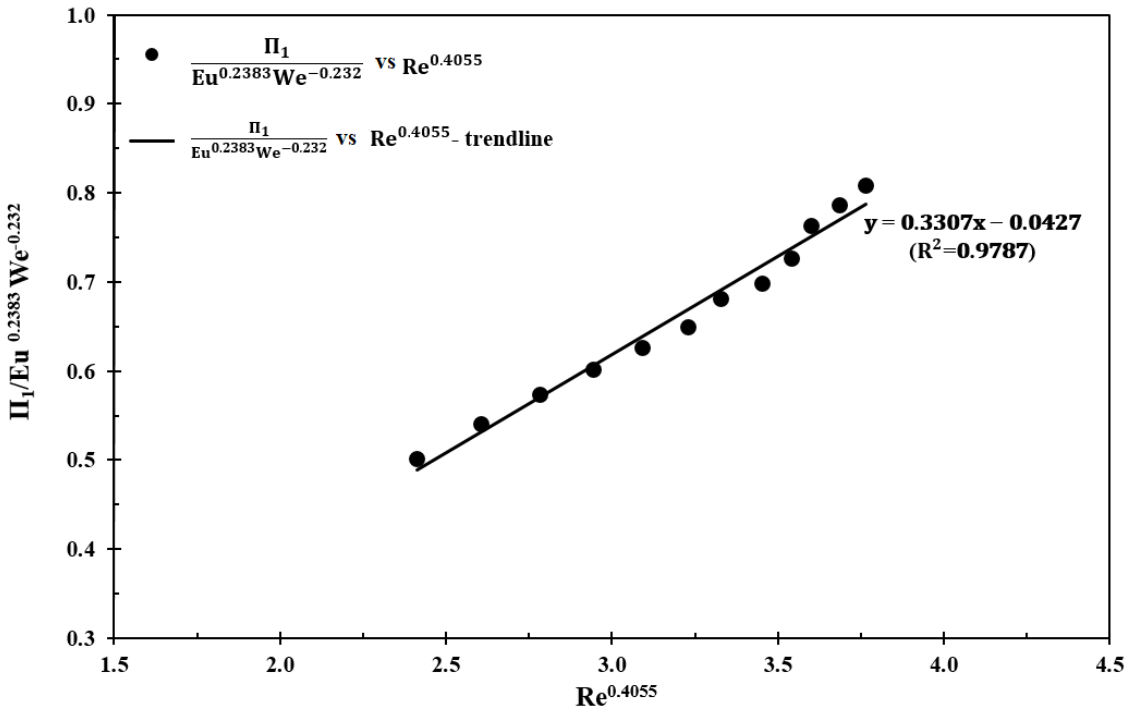

Figure 8.5: x/h versus the combined dimensionless groups

To determine the value of C, the slope of the correlation lines were combined with all the dimensionless groups with respect to x/h, as shown in Figure 8.5. The final correlation model developed in this study is:

$$\frac{x}{h} = 0.3307 \cdot (Re)^{0.4055} \cdot (Eu)^{0.2383} \cdot (We)^{-0.232} \tag{8.2}$$

8.3 Correlation Validation

Two new simulations for different conditions of oil / water multiphase flow were conducted, which is to validate the new correlation (Table 8.3). The validation range of the correlation is limited to the studied domain of the parameter and phase properties of oil and water.

As illustrated in Figure 8.6, the simulation results are close to the correlation's

Table 8.3: Validation for simulation cases

Pressure	**Oil volume fraction**	**Mixture density**	**Mixture viscosity**
Pa	α_o	ρ_m	μ_m
689,475	0.5	9355	0.1441
1,034,214	0.8	897.2	0.2298

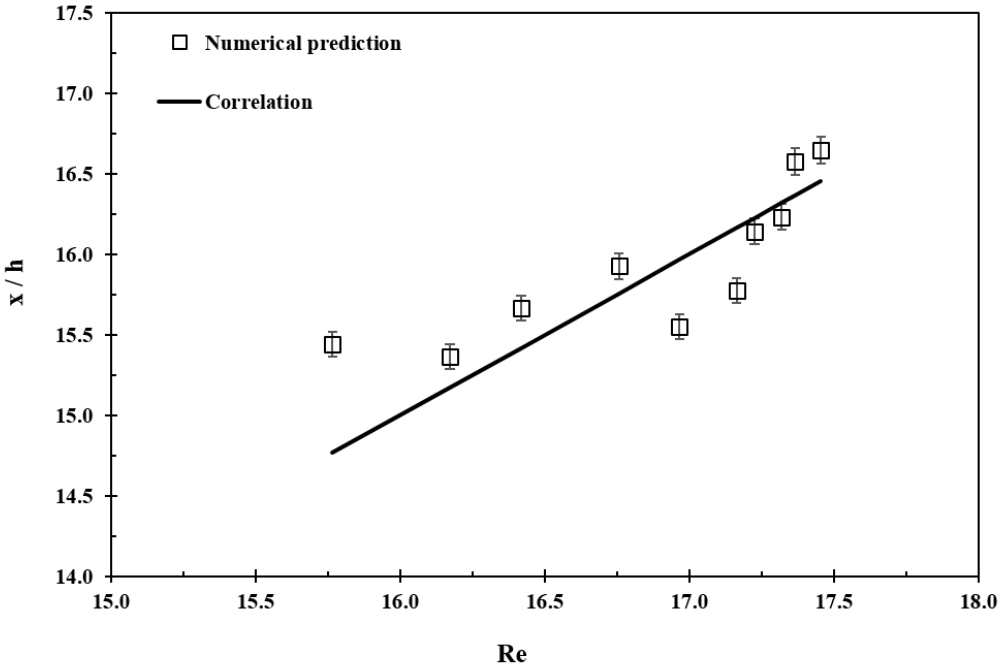

Figure 8.6: Comparison of the numerical simulation results with the correlation model

predicted values, with an average error of 1.7 % and a maximum error of 4.38 % between the two methods. In industrial applications, the new correlation developed in this chapter, Eq. 8.2 provides new insights into separator design for various operating conditions as well as new insights into the operating conditions that will achieve high separation efficiencies. As a further validation, the effect of inlet flow rate, which refers to Re number in this study, on separator size is compared with previous studies [97, 126]. The results from Ref. [126] proved that an increase inlet flow rate reduces the separation efficiency. Also, based on their model, a larger separator is

required to maintain the same separation efficiency. Even the exact separator length and height ratio are not provided in their work; however, their results obtained the same design requirement as our correlation predicted with Re number from 2 to 500.

8.4 Summary

A series of gravity-based, oil / water separation simulations were conducted to investigate the relationship between separator geometric design and multiphase fluid density (ρ_m), multiphase fluid viscosity (μ_m), fluid velocity (v), surface tension between two phases ($\sigma_{o/w}$), and operating pressure (P) by using a dimensionless analysis method. The CFD model was validated with experimental data. Then, a parametric study was conducted using different values of inlet velocity, oil volume fraction, temperature, pressure, and oil / water interfacial tension.

The simulation results revealed that the oil volume fraction has a complex effect on the separation process due to the different fluid mixture systems. Higher operating temperature increases the droplet rising velocity, but it does not change the overall separation efficiency. Operating pressure has a significant effect on the oil / water separation process by affecting the separation time. As found in this section, a rise of pressure greatly increases the separation time.

Also, the results presented in this chapter indicate that the minimum theoretical length of the separator increases with Re number and Eu number; however, it decreases with We number. Finally, a new correlation (Eq. 8.2) has been developed among the four dimensionless groups to predict a more optimal geometric design of the separator.

Chapter 9

Conclusions, Contributions and Recommendations

9.1 Conclusions

9.1.1 Conclusions of coalescence model development

In this work, a high-level semi-analytical model of droplet coalescence was developed to predict droplet coalescence in liquid / liquid separation. The model is based on oil volume fraction and binary droplet coalescence. The new model is combined with a force balance method to predict the separation dynamics with an accuracy of 94.5 % (based on three validation simulations). The numerical simulation results showed that an increase in oil volume fraction resulted in a decrease of the coalescence time of oil droplets in the water phase. However, for water droplets in the oil phase system, the coalescence time increases with the oil volume fraction. The validated simulation results presented good match with the developed model to predict the coalescence time.

9.1.2 Conclusions of experimental study

Two models, batch separation model, and continuous separation model, were developed that can be tested at normal pressures and temperatures in order to validate or calibrate the analytical and numerical models. The uncertainty of the measurements of this experimental study was ±2.75%. The results of the experiments showed that the inlet flow rate has a negative effect on the oil / water separation process. When the initial oil volume fraction increases, the oil volume fraction in the water phase increases for the first 2 minutes. However, it does not affect the total separation time.

9.1.3 Conclusions of CFD simulation study

In this thesis, multiphase flow modeling was developed, which applied ANSYS Fluent (16.2) to simulate the dynamic fluid effects in a gravity separator. The grid-independence study showed that an element size of 0.05 inches was the optimal size. The simulation results were validated with experimental results under the same operating conditions for oil / water separation efficiency. Further, oil volume fractions and the velocity vector distribution in the separator were investigated. Both of the results showed that there is a mixing zone located at the entrance, which has a relatively lower oil volume fraction and a higher velocity. Thus, the inlet velocity's affect on the mixing length had been investigated. The results showed that when inlet velocity is in the region where the fluid in the separator is in the laminar regime, the mixing length is less than 40 % of the total separator length. However, increasing the inlet velocity until the fluid in the separator is in the transition zone, resulting in the mixing length occupying 90 % of the total separator length.

9.1.4 Conclusions of correlation development

A series of gravity-based, oil / water separation simulations were conducted to develop a correlation to allow CFD results matched with the lab-scale experimental data, to be scaled up to prototype behavior. The dimensional analysis was used to investigate the relationship between separator geometric design and multiphase fluid density (ρ_m), multiphase fluid viscosity (μ_m), fluid velocity (v), surface tension between two phases ($\sigma_{o/w}$), and operating pressure (P), by using a dimensionless analysis method. The proposed CFD model was validated with experimental data based on our study. Then, a parametric study was carried out using different values of inlet velocity, oil volume fraction, temperature, pressure, and oil / water interfacial tension.

The simulation results reveal that oil volume has a complex effect on the separation process due to the different emulsion systems. Increased operating temperature increases the droplet rising velocity, but it does not change the overall separation efficiency. Operating pressure exerts a significant effect on the oil / water separation process, and the time needed for oil to separate from the water phase increases with the increase of pressure.

In addition, the results of the correlation presented in this work indicate that the theoretical minimum length of the separator increases with the Re number, and the Eu number; however, decreases with the We number. These correlation results are consistent since an increase in the Re number, and Eu number decreases the separation efficiency. Therefore, it requires a larger separator to keep the same separation efficiency. Conversely, when the We number is less than 3, a higher oil / water surface tension leads to greater droplet collision efficiency, improving the separation efficiency, and thus requires smaller separator geometry.

Finally, a new correlation (Eq. 8.2) has been developed among the four dimensionless groups to predict the geometric design of separator.

9.2 Contributions

This research provided valuable new insights into liquid / liquid separation. The research included numerical predictions, new experimental data, correlation development, and semi-analytical modeling. The developed CFD predictions and semi-analytical model provided both macroscopic and microscopic understanding of the liquid / liquid separation phenomenon. Compared with the previous CFD based studies of multiphase flow, the current study provides detailed information about oil / water separation process, and the thesis provides all details of developed CFD models. The other significant accomplishments are as follows:

- In this study, the whole separator volume was modeled in numerical simulation, which provided more accurate results compared with symmetrical geometry profiles that have been assumed in previous studies.

- A high accuracy simulation model was developed in this study, which can be used to model other immiscible liquids separation in a wider range of operating parameters. The accuracy of the simulation model was approved based on comparing the numerical simulation accuracy among various commercial software, and different viscosity models.

- This study developed a semi-analytical model to improve the understanding of the droplet coalescence process. The developed innovative coalescence model can be used to predict liquid / liquid separation for immiscible liquids with arbitrary volume fraction.

- The new correlation developed in this study can provide new insights into separator design for various operating conditions as well as new insights into the operating conditions that will achieve high separation efficiencies.

9.3 Recommendations for Future Work

The research results show that the CFD simulation method can provide an accurate prediction for liquid / liquid separation processes, and the developed semi-analytical model can be used to the optimization of the design of new separators. Recommendations for future work are the following:

- In previous CFD studies, the one-factor-one-time method has been used to design separators. As noted, this method is not efficient. Thus, it is recommended that the correlation developed in this research should be used for optimizing the geometric design of a separator.

- Although the developed correlation predicted accurate results for gravity separator design, it is recommended that this correlation should be empirically validated using different industry field fluids in the large-scale liquid / liquid separators.

- Testing alternative liquid / liquid systems, increasing knowledge of the droplet coalescence process, especially for fluids in the wider Re range, would be a necessary precursor to validating the coalescence model, which is proposed in this study.

- With expected development in CFD modeling technologies, separation conditions involved subsea environment, such as high pressures, low temperatures can be simulated, and the realistic separation performance of separator would be studied.

- The binary coalescence model would be extended to model the binary bubble coalescence process. Thus, for future study, gas bubbles separation from liquid can be predicted with a binary bubble coalescence model. Therefore, the binary

coalescence model developed in this thesis can be tested and extended to the three-phase separation process.

Bibliography

[1] AC Gjerdseth, A Faanes, et al. The tordis ior project. In *Offshore technology conference*. Offshore Technology Conference, 2007.

[2] T Horn, G Eriksen, W Bakke, et al. Troll pilot-definition, implementation and experience. In *Offshore Technology Conference*. Offshore Technology Conference, 2002.

[3] R Orlowski, ML Euphemio, et al. Marlim 3 phase subsea separation system-challenges and solutions for the subsea separation station to cope with process requirements. In *Offshore Technology Conference*. Offshore Technology Conference, 2012.

[4] L Bon and A Pazflor. World technology first in deep offshore development. 2009.

[5] D Denney. Subsea separation and reinjection of produced water. *Journal of Petroleum Technology*, 52(04):48–51, 2000.

[6] T Horn, W Bakke, et al. Experience in operating world's first subsea separation and water injection station at troll oil field in the north sea. In *Offshore Technology Conference*. Offshore Technology Conference, 2003.

[7] AK Gupta, R Rai, et al. Produced-water separation at unmanned offshore wellhead platform: A concept report. In *SPE Annual Technical Conference and Exhibition*. Society of Petroleum Engineers, 2009.

[8] A Falconer. Gravity separation: old technique/new methods. *Physical Separation in Science and Engineering*, 12(1):31–48, 2003.

[9] L Powers et al. New perspective on oil and gas separator performance (includes associated papers 26945 and 26947). *SPE Production & Facilities*, 8(02):77–83, 1993.

[10] DJ McClements. *Food emulsions: principles, practices, and techniques*. CRC press, 2015.

[11] J Sjöblom, NR Aske, et al. Our current understanding of water-in-crude oil emulsions.: Recent characterization techniques and high pressure performance. *Advances in Colloid and Interface Science*, 100:399–473, 2003.

[12] JD Schwarzkopf, M Sommerfeld, et al. *Multiphase flows with droplets and particles*. CRC press, 2011.

[13] J Hinze. Fundamentals of the hydrodynamic mechanism of splitting in dispersion processes. *AIChE Journal*, 1(3):289–295, 1955.

[14] W Stanley and E Walas. Chemical process equipment-selection and design. *Butterman-Heinemam Series*, 1990.

[15] R Smith. *Chemical process: design and integration*. John Wiley & Sons, 2005.

[16] M Mostafaiyan, MR Saeb, et al. Application of evolutionary computational approach in design of horizontal three-phase gravity separators. *Journal of Petroleum Science and Engineering*, 119:28–35, 2014.

[17] NO Skeie and M Halstensen. Level estimation in oil/water separators based on multiple pressure sensors and multivariate calibration. *Journal of Chemometrics*, 24(7-8):387–398, 2010.

[18] R Branion. Principles for the separation of oil drops from water in gravity type separators. In *Oil in Freshwater: Chemistry, Biology, Countermeasure Technology*, pages 431–442. Elsevier, 1987.

[19] R Arntzen. *Gravity separator revamping*. PhD thesis, University of Science and Technology, 2001.

[20] HV Smith. Oil and gas separators. *Petroleum Engineering Handbook*, 1987.

[21] M Stewart and K Arnold. *Gas-liquid and Liquid-liquid Separators*. Gulf Professional Publishing, 2008.

[22] WY Svrcek and WD Monnery. Design two-phase separators within the right limits. *Chemical engineering progress*, 89(10):53–60, 1993.

[23] JF Keller. Oil-water separation process, 1975. US Patent 3,867,285.

[24] R Padilla, MC Ruiz, et al. Separation of liquid-liquid dispersions in a deep-layer gravity settler: Part i. experimental study of the separation process. *Hydrometallurgy*, 42(2):267–279, 1996.

[25] ME Rowley and G Davies. Design of plate separators for the separation of oil-water dispersions. *Chemical Engineering Research and Design*, 66(4):313–322, 1988.

[26] L Schlieper, M Chatterjee, et al. Liquid–liquid phase separation in gravity settler with inclined plates. *AIChE journal*, 50(4):802–811, 2004.

[27] EY Fitnawan, RM Rivera, et al. Inclined gravity downhole oil-water separator: Using laboratory experimental results for predicting the impact of its application in high rate production wells. In *Asia Pacific Oil and Gas Conference & Exhibition*. Society of Petroleum Engineers, 2009.

[28] SK Jeelani, R Hosig, et al. Kinetics of low reynolds number creaming and coalescence in droplet dispersions. *AIChE journal*, 51(1):149–161, 2005.

[29] N Yusuf, Y Al-Wahaibi, et al. Effect of oil viscosity on the flow structure and pressure gradient in horizontal oil–water flow. *Chemical Engineering Research and Design*, 90(8):1019–1030, 2012.

[30] ZS Bai, HL Wang, et al. Oil–water separation using hydrocyclones enhanced by air bubbles. *Chemical Engineering Research and Design*, 89(1):55–59, 2011.

[31] C Gomez, J Caldentey, et al. Oil/water separation in liquid/liquid hydrocyclones (llhc): Part 1-experimental investigation. *SPE Journal*, 7(04):353–372, 2002.

[32] LR Castilho and RA Medronho. A simple procedure for design and performance prediction of bradley and rietema hydrocyclones. *Minerals Engineering*, 13(2):183–191, 2000.

[33] DF Kelsall. A further study of the hydraulic cyclone. *Chemical Engineering Science*, 2(6):254–272, 1953.

[34] TJ Olson and R Van Ommen. Optimizing hydrocyclone design using advanced cfd model. *Minerals engineering*, 17(5):713–720, 2004.

[35] XJ Zhang, Y Cheng, et al. Simulation of multiphase flow of the oil-water separation in a rotating packed bed for oil purification. *Mathematical Problems in Engineering*, 2013, 2013.

[36] N Butin, C Candelier, et al. A new simple and efficient technology for subsea bulk oil/water separation for production enhancement-3c cyclonic separator. In *Offshore Mediterranean Conference and Exhibition*. Offshore Mediterranean Conference, 2011.

[37] NM Kocherginsky, CL Tan, et al. Demulsification of water-in-oil emulsions via filtration through a hydrophilic polymer membrane. *Journal of membrane science*, 220(1-2):117–128, 2003.

[38] M Eshrati, T Al-Wahaibi, et al. Experimental study of drag reduction of polymer-polymer mixtures in horizontal dispersed oil-water flow. *Experimental Thermal and Fluid Science*, 83:169–176, 2017.

[39] JM Lee, R Khan, et al. Debottlenecking and cfd studies of high-and low-pressure production separators. In *SPE Annual Technical Conference and Exhibition*. Society of Petroleum Engineers, 2008.

[40] CM Lee, M Legg, et al. Field confirmation of cfd design for fpso-mounted separator. In *Offshore Technology Conference*. Offshore Technology Conference, 2004.

[41] YJ Lu, JM Lee, et al. Effect of internal baffles on volumetric utilization of an fwko–a cfd evaluation. In *SPE Annual Technical Conference and Exhibition*. Society of Petroleum Engineers, 2007.

[42] T Austrheim. Experimental characterization of high-pressure natural gas scrubbers. 2006.

[43] P Laleh. *CFD simulation of multiphase separators*. PhD thesis, University of Calgary, 2010.

[44] YT Liang, SQ Zhao, et al. Numerical simulation on flow field of oilfield three-phase separator. *Journal of Applied Mathematics*, 2013, 2013.

[45] J Behin and S Bahrami. Modeling an industrial dissolved air flotation tank used for separating oil from wastewater. *Chemical Engineering and Processing: Process Intensification*, 59:1–8, 2012.

[46] HA Hussein, R Abdullah, et al. Numerical model of baffle location effect on flow pattern in oil and water gravity separator tanks. *World Applied Sciences Journal*, 26(10):1351–1356, 2013.

[47] S Huang. Numerical simulation of oil-water hydrocyclone using reynolds-stress model for eulerian multiphase flows. *The Canadian Journal of Chemical Engineering*, 83(5):829–834, 2005.

[48] YL Lü, L He, et al. Numerical simulation of flow field inside gravitational separator with different internals. *China Petroleum Machinery*, 2:5, 2008.

[49] HF Liu, JY Xu, et al. Numerical study on oil and water two-phase flow in a cylindrical cyclone. *Journal of Hydrodynamics, Ser. B*, 22(5):832–837, 2010.

[50] S Noroozi and S H Hashemabadi. Cfd simulation of inlet design effect on deoiling hydrocyclone separation efficiency. *Chemical engineering & technology*, 32(12):1885–1893, 2009.

[51] S Noroozi and SH Hashemabadi. Cfd analysis of inlet chamber body profile effects on de-oiling hydrocyclone efficiency. *Chemical Engineering Research and Design*, 89(7):968–977, 2011.

[52] D Wilkinson, B Waldie, et al. Baffle plate configurations to enhance separation in horizontal primary separators. *Chemical Engineering Journal*, 77(3):221–226, 2000.

[53] T Frankiewicz and CM Lee. Using cfd simulation to model fluid motion in process vessels on fixed and floating platforms. In *Proceedings of SPE Annual Technical Conference, San Antonio*, 2002.

[54] LQ Chen, SJ Wu, et al. Numerical simulation and structural optimization of the inclined oil/water separator. *PloS one*, 10(4):e0124095, 2015.

[55] H Zhou, WM Sun, et al. Application of cfd in the modification of an oil–gas separator design. *J. Hydrodyn., Ser. A*, 19:926–929, 2004.

[56] AJ Yamaguchi. A numerical study on the oil-water separation process. In *SPE Annual Technical Conference and Exhibition*. Society of Petroleum Engineers, 2013.

[57] KS Kim, MH Kim, et al. Dynamic coupling between ship motion and three-layer-liquid separator by using moving particle simulation. *International Journal of Offshore and Polar Engineering*, 24(02):122–128, 2014.

[58] M Modigell and M Weng. Pressure loss and separation characteristics calculation of a uniflow cyclone with a cfd method. *Chemical Engineering & Technology: Industrial Chemistry-Plant Equipment-Process Engineering-Biotechnology*, 23(9):753–758, 2000.

[59] SY Shi, YX Wu, et al. A study on separation performance of a vortex finder in a liquid-liquid cylindrical cyclone. *Journal of Hydrodynamics, Ser. B*, 22(5):391–397, 2010.

[60] ZL Li, SP Dong, et al. Internal flow field in gravity oil-gas-water separators. *China Petroleum Machinery*, 7:3, 1999.

[61] HB Luo, J Feng, et al. Cfd simulation of the inner flow fie1d of the gas-liquid measure cyclones. *Mechanical Engineer*, 1:74–76, 2007.

[62] EW Hansen. Phenomenological modelling and simulation of fluid flow and separation behavior in offshore gravity separators. *ASME-PUBLICATIONS-PVP*, 431:23–30, 2001.

[63] Y Zhang, MH Jiang, et al. Design and experimental study of hydrocyclone in series and in bridge of downhole oil/water separation system. In *ASME 2009 28th International Conference on Ocean, Offshore and Arctic Engineering*, pages 429–434. American Society of Mechanical Engineers Digital Collection, 2009.

[64] H Breisig, M Schmidt, et al. Droplet-based liquid–liquid extraction inside a porous capillary. *Chemical Engineering Journal*, 307:143–149, 2017.

[65] Sleicher J. Axial mixing and extraction efficiency. *AIChE Journal*, 5(2):145–149, 1959.

[66] SC Cheung, GH Yeoh, et al. Population balance modeling of bubbly flows considering the hydrodynamics and thermomechanical processes. *AIChE journal*, 54(7):1689–1710, 2008.

[67] D Ramkrishna. The status of population balances. *Reviews in chemical engineering*, 3(1):49–95, 1985.

[68] V Nguemaha and HX Zhou. Liquid-liquid phase separation of patchy particles illuminates diverse effects of regulatory components on protein droplet formation. *Scientific reports*, 8(1):1–11, 2018.

[69] AA Hyman, CA Weber, et al. Liquid-liquid phase separation in biology. *Annual review of cell and developmental biology*, 30:39–58, 2014.

[70] D Zwicker, R Seyboldt, et al. Growth and division of active droplets provides a model for protocells. *Nature Physics*, 13(4):408–413, 2017.

[71] S Alberti, A Gladfelter, et al. Considerations and challenges in studying liquid-liquid phase separation and biomolecular condensates. *Cell*, 176(3):419–434, 2019.

[72] A Shakya, S Park, et al. Liquid-liquid phase separation of histone proteins in cells: role in chromatin organization. *Biophysical Journal*, 118(3):753–764, 2020.

[73] YX Liao and D Lucas. A literature review on mechanisms and models for the coalescence process of fluid particles. *Chemical Engineering Science*, 65(10):2851–2864, 2010.

[74] JA Melheim and M Chiesa. Simulation of turbulent electrocoalescence. *Chemical Engineering Science*, 61(14):4540–4549, 2006.

[75] R Shinnar and JM Church. Statistical theories of turbulence in predicting particle size in agitated dispersions. *Industrial & Engineering Chemistry*, 52(3):253–256, 1960.

[76] JC Lee and TD Hodgson. Film flow and coalescence-i basic relations, film shape and criteria for interface mobility. *Chemical Engineering Science*, 23(11):1375–1397, 1968.

[77] EG Sinaiski and EJ Lapiga. *Separation of multiphase, multicomponent systems*. John Wiley & Sons, 2007.

[78] ST Thoroddsen and K Takehara. The coalescence cascade of a drop. *Physics of Fluids*, 12(6):1265–1267, 2000.

[79] F Blanchette and TP Bigioni. Partial coalescence of drops at liquid interfaces. *Nature Physics*, 2(4):254, 2006.

[80] KJ Valentas and NR Amundson. Breakage and coalescence in dispersed phase systems. *Industrial & Engineering Chemistry Fundamentals*, 5(4):533–542, 1966.

[81] HA Jakobsen, H Lindborg, et al. Modeling of bubble column reactors: progress and limitations. *Industrial & engineering chemistry research*, 44(14):5107–5151, 2005.

[82] SM Damian, GC Buscaglia, et al. Water/oil separation modeling by population balance equations-solution of the probability density function. In *Congreso sobre Métodos Numéricos y sus Aplicaciones, 21*. Instituto Balseiro-Centro Atómico Bariloche, 2014.

[83] BA Grimes. Population balance model for batch gravity separation of crude oil and water emulsions. part i: model formulation. *Journal of Dispersion Science and Technology*, 33(4):578–590, 2012.

[84] MC Ruiz and R Padilla. Separation of liquid-liquid dispersions in a deep-layer gravity settler: Part ii. mathematical modeling of the settler. *Hydrometallurgy*, 42(2):281–291, 1996.

[85] WJ Howarth. Coalescence of drops in a turbulent flow field. *Chemical Engineering Science*, 19(1):33–38, 1964.

[86] F Lehr, M Millies, et al. Bubble-size distributions and flow fields in bubble columns. *AIChE Journal*, 48(11):2426–2443, 2002.

[87] WJ Howarth. Measurement of coalescence frequency in an agitated tank. *AIChE Journal*, 13(5):1007–1013, 1967.

[88] H Sovova. Breakage and coalescence of drops in a batch stirred vessel—ii comparison of model and experiments. *Chemical Engineering Science*, 36(9):1567–1573, 1981.

[89] AK Chesters. Modelling of coalescence processes in fluid-liquid dispersions: a review of current understanding. *Chemical engineering research and design*, 69(A4):259–270, 1991.

[90] V Alopaeus, JK Koskinen, et al. Simulation of the population balances for liquid–liquid systems in a nonideal stirred tank. part 2—parameter fitting and the use of the multiblock model for dense dispersions. *Chemical Engineering Science*, 57(10):1815–1825, 2002.

[91] MW Vaughn and JC Slattery. Effects of viscous normal stresses in thin draining films. *Industrial & engineering chemistry research*, 34(10):3185–3186, 1995.

[92] W Podgórska and J Bałdyga. Scale-up effects on the drop size distribution of liquid–liquid dispersions in agitated vessels. *Chemical engineering science*, 56(3):741–746, 2001.

[93] SP Liu and DM Li. Drop coalescence in turbulent dispersions. *Chemical Engineering Science*, 54(23):5667–5675, 1999.

[94] MJ Prince and HW Blanch. Bubble coalescence and break-up in air-sparged bubble columns. *AIChE journal*, 36(10):1485–1499, 1990.

[95] TF Wang, JF Wang, et al. Population balance model for gas- liquid flows: Influence of bubble coalescence and breakup models. *Industrial & engineering chemistry research*, 44(19):7540–7549, 2005.

[96] ML Powers. Analysis of gravity separation in freewater knockouts. *SPE Production Engineering*, 5(01):52–58, 1990.

[97] AF Sayda and JH Taylor. Modeling and control of three-phase gravilty separators in oil production facilities. In *2007 American Control Conference*, pages 4847–4853. IEEE, 2007.

[98] C Noik, JQ Chen, et al. Electrostatic demulsification on crude oil: A state-of-the-art review. In *International Oil & Gas Conference and Exhibition in China*. Society of Petroleum Engineers, 2006.

[99] JP Estrade, H Carentz, et al. Experimental investigation of dynamic binary collision of ethanol droplets–a model for droplet coalescence and bouncing. *International Journal of Heat and Fluid Flow*, 20(5):486–491, 1999.

[100] FC Wang, FQ Yang, et al. Size effect on the coalescence-induced self-propelled droplet. *Applied Physics Letters*, 98(5):53112, 2011.

[101] T Frising, C Noïk, et al. The liquid/liquid sedimentation process: from droplet coalescence to technologically enhanced water/oil emulsion gravity separators: a review. *Journal of dispersion science and technology*, 27(7):1035–1057, 2006.

[102] G Narsimhan. Model for drop coalescence in a locally isotropic turbulent flow field. *Journal of colloid and interface science*, 272(1):197–209, 2004.

[103] JA Boxall, CA Koh, et al. Measurement and calibration of droplet size distributions in water-in-oil emulsions by particle video microscope and a focused beam

reflectance method. *Industrial & engineering chemistry research*, 49(3):1412–1418, 2010.

[104] PJ Pritchard and JW Mitchell. *Fox and McDonald's Introduction to Fluid Mechanics*. John Wiley & Sons, 2016.

[105] S Ross. Variation with temperature of surface tension of lubricating oils. Technical report, Stanford University CA, 1950.

[106] JA Boxall, CA Koh, et al. Measurement and calibration of droplet size distributions in water-in-oil emulsions by particle video microscope and a focused beam reflectance method. *Industrial & Engineering Chemistry Research*, 49(3):1412–1418, 2009.

[107] GB Young, WD Wakley, et al. Oil-water separation using hydrocyclones: An experimental search for optimum dimensions. *Journal of petroleum science and engineering*, 11(1):37–50, 1994.

[108] YC Tan, AP Lee, et al. Droplet coalescence by geometrically mediated flow in microfluidic channels. *Microfluidics and Nanofluidics*, 3(4):495–499, 2007.

[109] FA Mcclintock. Describing uncertainties in single-sample experiments. *Mechanical Engineering*, 75(1):3–8, 1953.

[110] Ansys Fluent. 12.0 user's guide. *Ansys Inc*, 2009. `https://d1wqtxts1xzle7.cloudfront.net/39020281/ANSYS_FLUENT_12.0_UDF_Manual.pdf?1444104412=&response-content-disposition=inline`.

[111] D A Colman and M T Thew. Hydrocyclones to give a highly concentrated sample of a lighter dispersed phase. In *The International Conference Hydrocyclone, BHRA Fluid Engineering, Cambridge, UK*, 1980.

[112] S V Patankar. Numerical fluid flow and heat transfer. 1980.

[113] EM Hansen, H Heitmann, et al. Numerical simulation of fluid flow behavior inside, and redesign of a field separator. In *Proc*, pages 117–129, 1993.

[114] CW Hirt, NC Romero, et al. Sola-df: A solution algorithm for nonequilibrium two-phase flow. Technical report, Los Alamos Scientific Lab., 1979.

[115] JM Sicilian, CW Hirt, et al. Flow-3d: Computational modeling power for scientists and engineers. *Flow Science Report (FSI-87-00-1)*, 1987 - 2016.

[116] H Rusche. *Computational fluid dynamics of dispersed two-phase flows at high phase fractions*. PhD thesis, University of London, 2003.

[117] J Christopher. Openfoam user guide, v5. 0. *OpenFOAM Foundation Ltd*, 230. `http://foam.sourceforge.net/docs/Guides-a4/OpenFOAMUserGuide-A4.pdf`.

[118] JT Davies. Drop sizes of emulsions related to turbulent energy dissipation rates. *Chemical Engineering Science*, 40(5):839–842, 1985.

[119] DM Sztukowski and HW Yarranton. Oilfield solids and water-in-oil emulsion stability. *Journal of colloid and interface science*, 285(2):821–833, 2005.

[120] M Mohammadi, S Shahhosseini, et al. Direct numerical simulation of water droplet coalescence in the oil. *International Journal of Heat and Fluid Flow*, 36:58–71, 2012.

[121] M Rieber and A Frohn. Navier-stokes simulation of droplet collision dynamics. In *Proc. 7th Int. Symp. On Comp. Fluid Dynamics,(ed. by Zhuang, FG) Beijing, China*, pages 520–525, 1997.

[122] J Qian and CK Law. Regimes of coalescence and separation in droplet collision. *Journal of Fluid Mechanics*, 331:59–80, 1997.

[123] G M Vieira and A S Barrozo. Effect of vortex finder diameter on the performance of a novel hydrocyclone separator. *Minerals Engineering*, 57:50–56, 2014.

[124] YJ Jiang, A Umemura, et al. An experimental investigation on the collision behaviour of hydrocarbon droplets. *Journal of Fluid Mechanics*, 234:171–190, 1992.

[125] WH Chou, LP Hsiang, et al. Temporal properties of drop breakup in the shear breakup regime. *International Journal of Multiphase Flow*, 23(4):651–669, 1997.

[126] B Wiencke. Fundamental principles for sizing and design of gravity separators for industrial refrigeration. *International journal of refrigeration*, 34(8):2092–2108, 2011.

Appendix A

Flow Meter Calibration

The two flow meters are used in this flow loop are provided by Omega with model number FTB-956 Liquid Turbine Flowmeter. Model FTB-956 belongs to the OMEGA FTB-950 Series turbine meters. This series of flow meters have male flared end fittings for easy connections. They come with a mating 2-wire connection and are able to provide 4 to 20 mA, or 0 to 5 Vdc, or amplified pulse outputs. The accuracy of this is $\pm$ 0.5 % rig. Repeatability is $\pm$ 0.05 %. The maximum pressure drop is 4 psi. The properties of this flow meter are listed in table A.1.

In this section, in order to calibrate the flowmeter, it has to be connected with a straight tube or pipe and a reference flow meter. Make sure the length of the inlet tube is at least 10 times longer than the diameter of the flow meter. The length of outlet tube has to be more than 5 times of the diameter of the flow meter.

For the reference flow meter, an FTB 692A-NPT flowmeter was used. The advantage of this flowmeter is, first of all, the local flow rate can be obtained directly by the display chart. Second, this flow meter has a self-calibration system which can be calibrated by just push the right button. For reading the signal, the flow meter needs to be connected to a computer. Various flow rates need to be tested in order

Table A.1: Table A.1 FTB-956 Flowmeter Properties

Range (water)	GPM	4 - 60
Nominal K factor		500
Maximum operating pressure	psi	4000
Temperature range	°C	-268 - 65
Length	$inch$	3.25
Approx weight	g	624

to get the calibration line. Flow rates are controlled by a valve from the inlet. The calibration curve of a turbine flow meter 1 and two are shown in Figure A.1 and A.2.

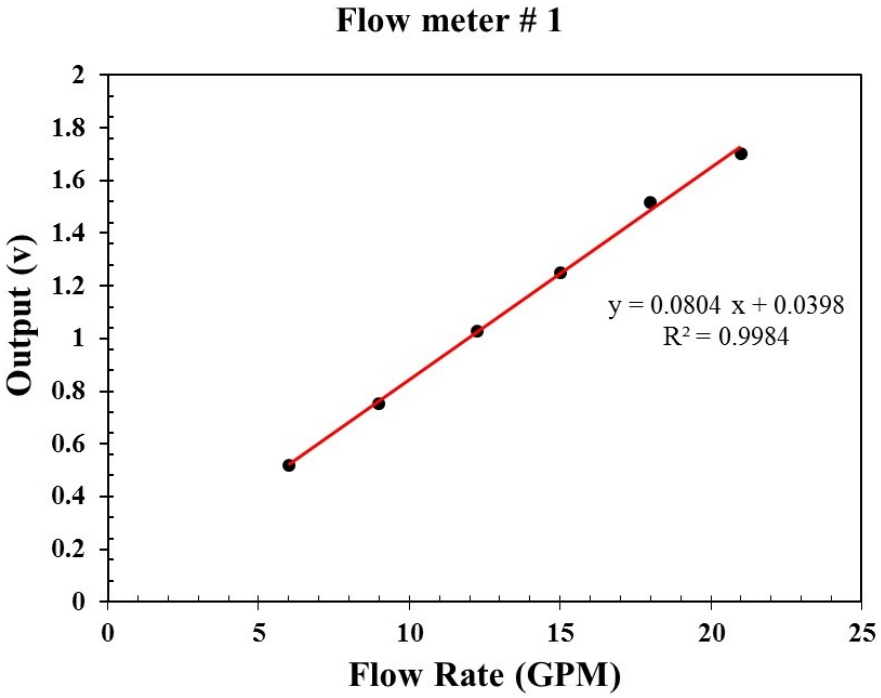

Figure A.1: Calibration curve for flowmeter 1

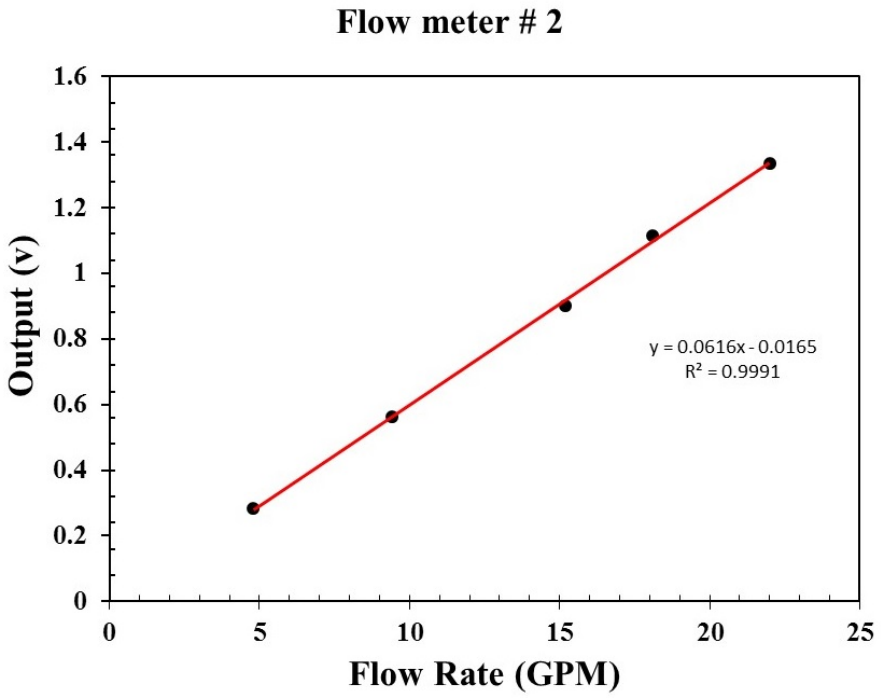

Figure A.2: Calibration curve for flowmeter 2

Appendix B

Outline of ANSYS Fluent CFD Simulation

ANSYS Fluent simulation is developed in workbench platform. The workbench platform breaks simulation procedure into five parts: geometry, mesh, setup, solution, and results.

Following the detail steps for each part.

- **Geometry** Geometry for the CFD simulation was created using ANSYS Design Modeler. Both 2-D and 3-D geometry can be developed by Design Modeler. Also, geometries, which are modeled in SOLIDWORKS and AutoCAD software, are able to export in for future simulation.

- **Mesh** ANSYS meshing was used for performing meshing for the CFD simulations. Initially the geometry domain is automeshed to give an overall indication of the meshing requirements for the simulation. Both global and local meshing are optional for user to choose to refine the mesh in critical areas. Global mesh controls are used to make global adjustment in the meshing strategy, which includes sizing function, inflation, smoothing, parameter inputs, et al., Local

mesh controls are used to define the local mesh size, which includes edge sizing, face sizing, and body sizing.

- **Mesh quality** several metrics define mesh quality, skewness and orthogonal quality are two of the important values used to determine if a mesh is adequate. Skewness values indicate how close an element or face is to the ideal, equilateral, version of that shape. Skewness values range from 0 to 1, with 0 being the best (equilateral), and 1 being the worst. Orthogonal quality is computed using face normal vectors for each face, vectors from the cell centroid to each of the faces, and vectors from the cell centroid to the centroids of each adjacent cell. Orthogonal quality for three dimensional cells also ranges from 0 to 1, but for this metric 0 is the worst, and 1 is the best quality cell.

- **Physics Setup** The fluid physical parameters, viscosity model, boundary conditions, convergence conditions, solver selection, and time step selection are all defined in here.

- **Postprocessing** It includes many tools for analyzing CFD restuls: Isosurfaces, vector plots, contour plots, streamlines and pathlines, XY plotting and animation creation. Also, postprocessing is able to analyize results based on user-defined memory through custom field functions.

Appendix C

Oil / water Separation Process Plots for ANSYS Fluent Simulation Results

The separation process is presented by oil volume fraction change with time. The color red represents phase of oil phase. Time step $t = 0.1s, 100s, 200s, 300s, 400s, 500s, 600s,$ and $672s$ were selected in this section. As evidenced by figure C.1 to C.8, the separation process is visible and the oil volume fraction is clearly changing in the separator. As shows by C.1Figure 8, at the beginning, oil-water multiphase are homogeneous mixtures since the oil volume fraction is uniform over the separator, which is 0.202. With the separation process continuing, the oil volume fraction is increasing at the top layer, and it is decreasing at the bottom. The maximum oil volume fraction in the separator at the selected time steps are 0.202, 0.403, 0.630, 0.676, 0.748, 0.883, 0.935, and 0.944, respectively. Figure 8 also shows that not only the oil volume fraction is increasing with time, also the separated oil volume is increasing over time. This shows the dynamic separation process by using CFD simulation method.

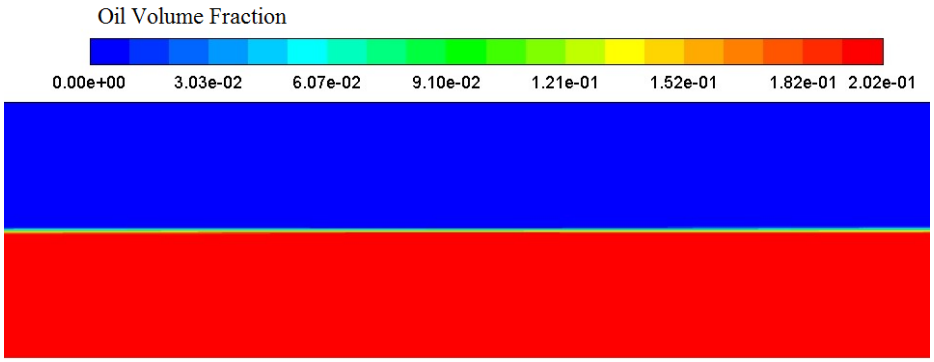

Figure C.1: Separation process plots at time = 0.1 sec

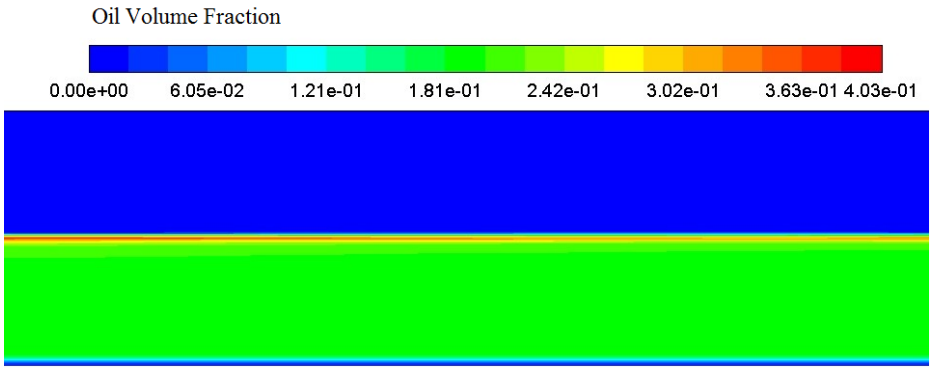

Figure C.2: Separation process plots at time = 100 sec

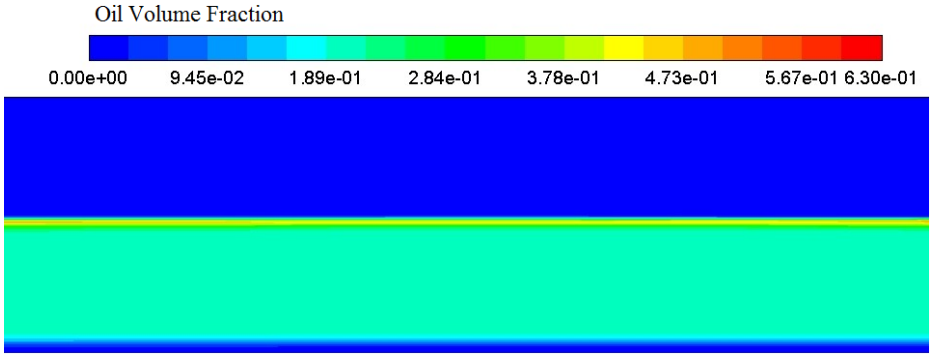

Figure C.3: Separation process plots at time = 200 sec

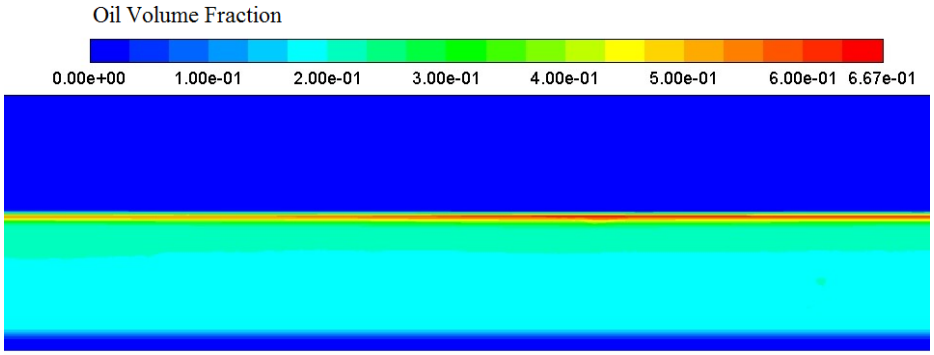

Figure C.4: Separation process plots at time = 300 sec

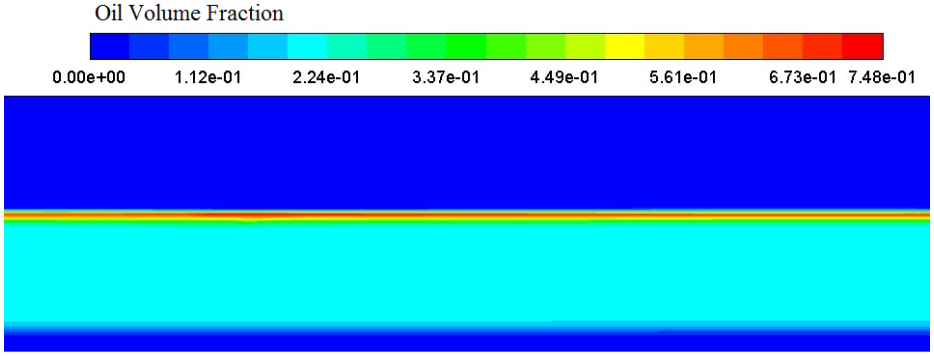

Figure C.5: Separation process plots at time = 400 sec

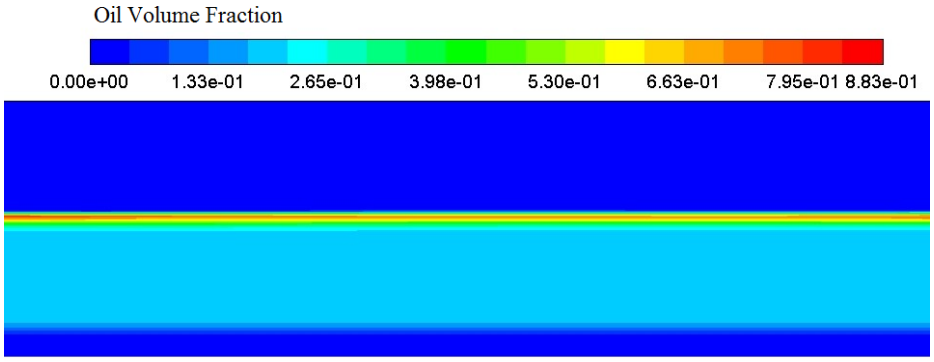

Figure C.6: Separation process plots at time = 500 sec

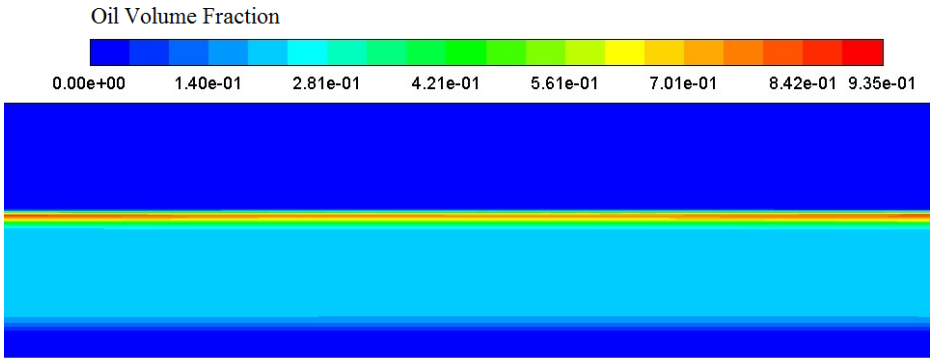

Figure C.7: Separation process plots at time = 600 sec

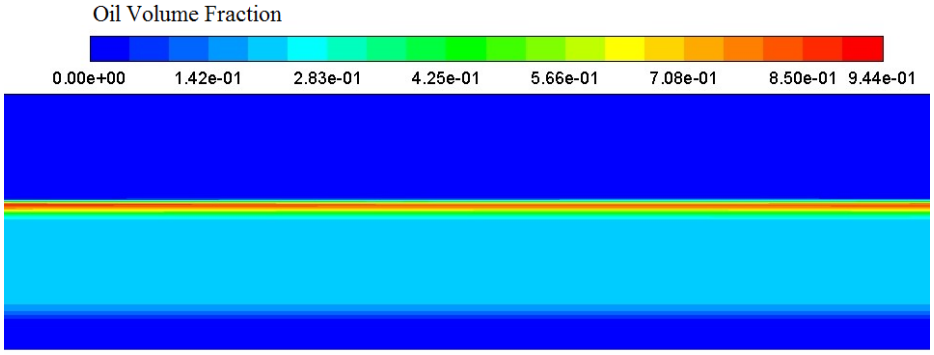

Figure C.8: Separation process plots at time = 672 sec

Appendix D

Outline of Flow3D CFD Simulation

The procedure of setup Flow 3D model are briefly described in this section.
Create a CFD mesh of separator. Import the stl. file for the separator drawn by Solidworks into the mesh. Set the simulation parameters. Run the simulation to get the simulation process in the separator step by step in time. Use the **GENERAL HISTORY** data source and **GRAPHICAL** output form under **PROBE** in **ANALYZE** to get the separation efficiency of the oil/water multiphase flow.
Following the detail steps for the operation of Flow3D software.

- Click on the FLOW 3D icon to get to Navigator.
- Under Navigator create new workspace on desktop.
- Under Navigator create new simulation on desktop.
- Click on Model Setup to get its sub-menus.
- Under General set things like free surface.
- Under Physics activate things like GMO.
- Under Fluids load data for water.

- Under Mesh Setup create the mesh.
- Under Mesh Setup import body STL file.
- Scale and translate body to fit mesh.
- Under Boundaries set boundary types.
- Under Initial set things like speeds.
- Under Output set data spacing.
- Under Numerics click on one fluid with interface.
- Under Simulation click on run.
- Under Analyze click on 3D probe.
- Expand time and click on STL and Render.Click on animation
- Under Analyze click on Probe and then on General History and then on Graphical Display,record RAO data.

Appendix E

Oil / water Separation Process Plots for FLOW-3D Simulation Results

Both batch separation (E.1 to E.3 and steady stage separation process (**??** to E.6) are simulated by using FLOW-3D software. Figure E.4 to E.6 and Figure E.7 to E.9 shows the simulation results of steady state separation process by using laminar and RNG turbulence model.

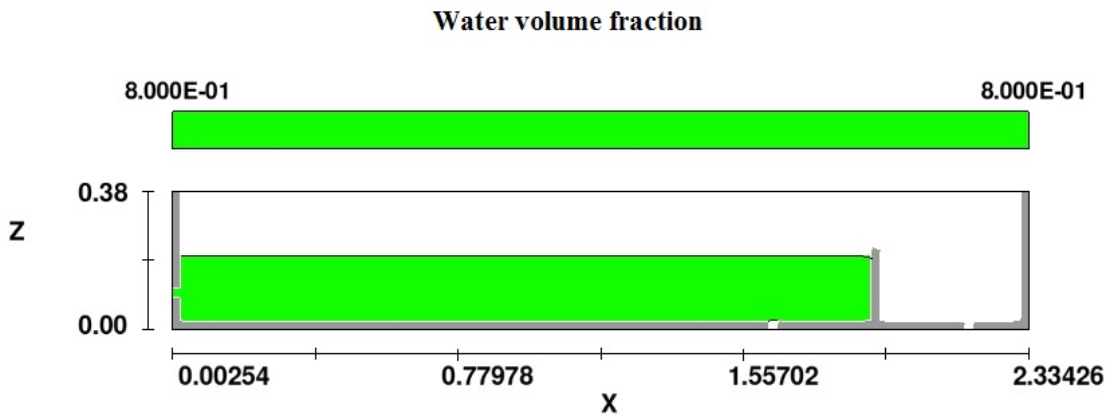

Figure E.1: Batch Separation process plots at time = 0 sec

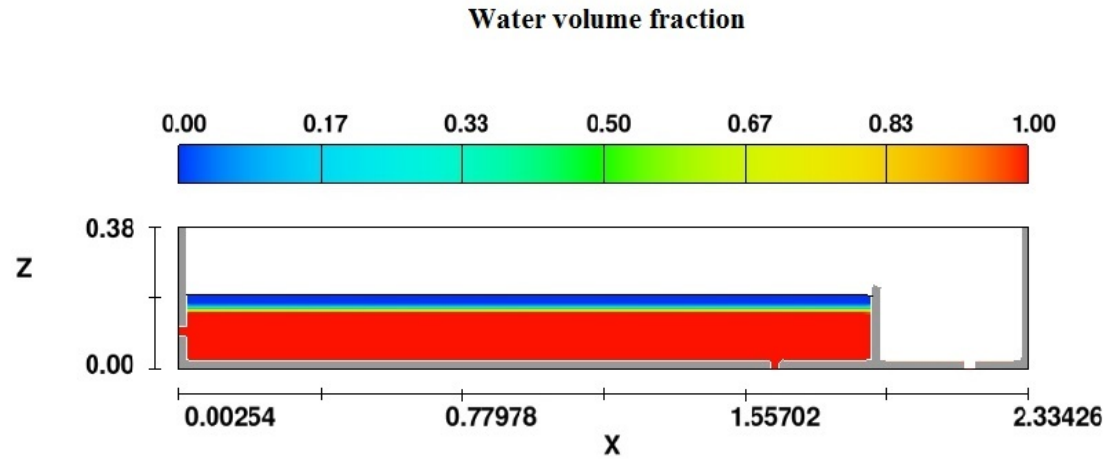

Figure E.2: Batch Separation process plots at time = 450 sec

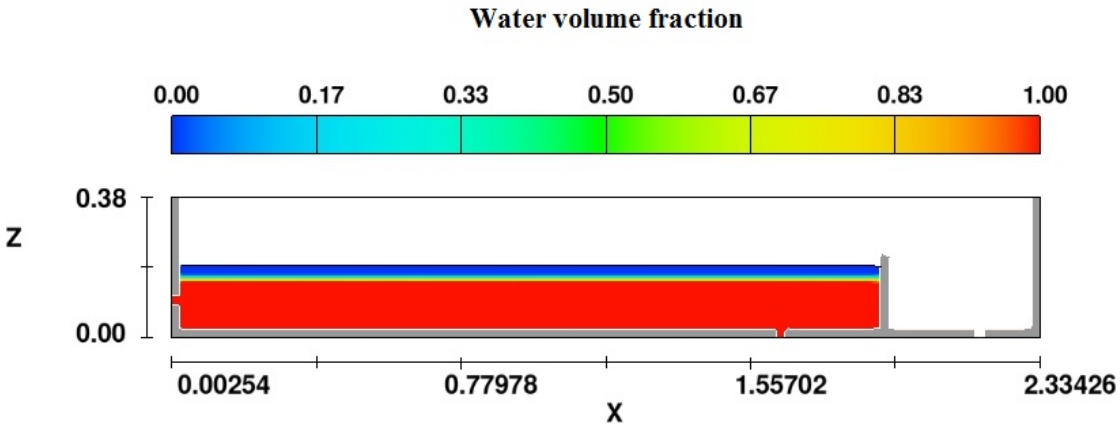

Figure E.3: Batch Separation process plots at time = 900 sec

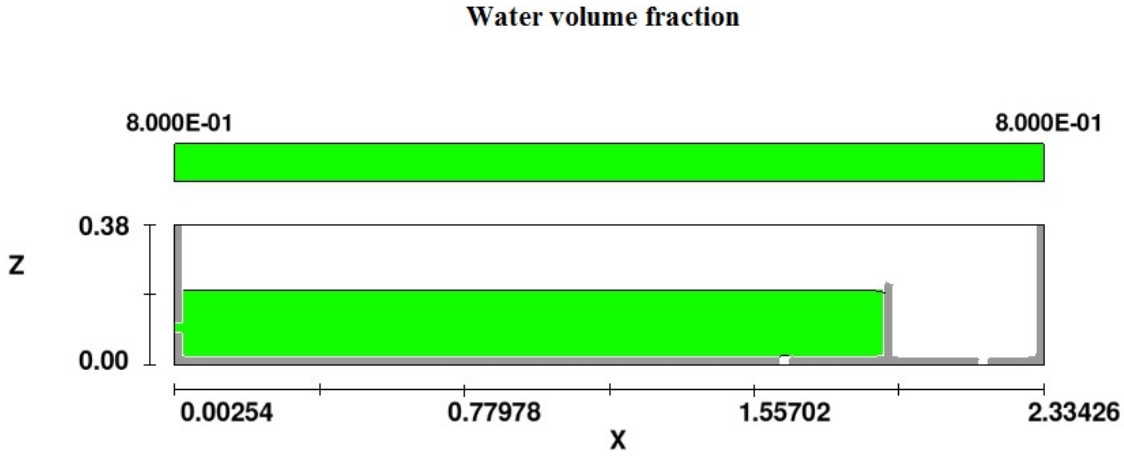

Figure E.4: Steady-state Separation process plots at time = 0 sec

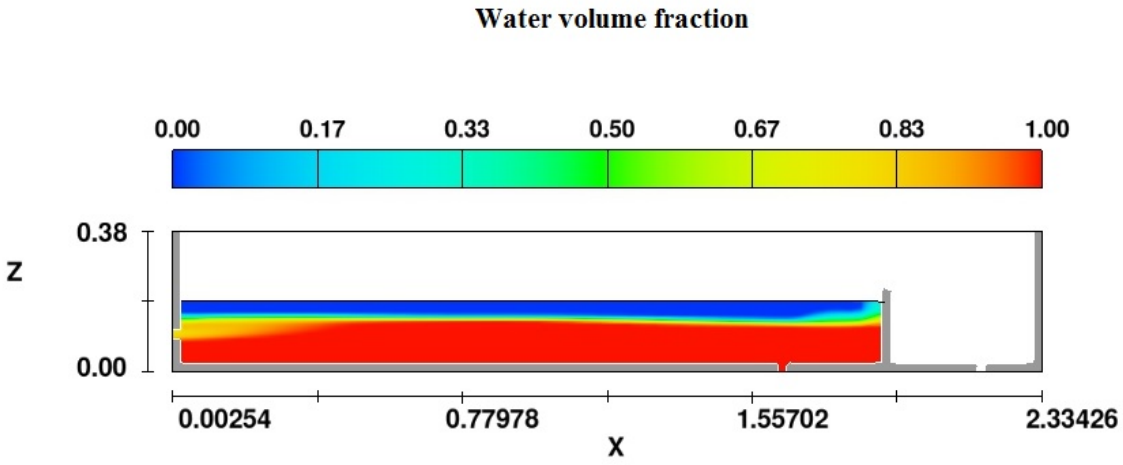

Figure E.5: Steady-state Separation process plots at time = 450 sec

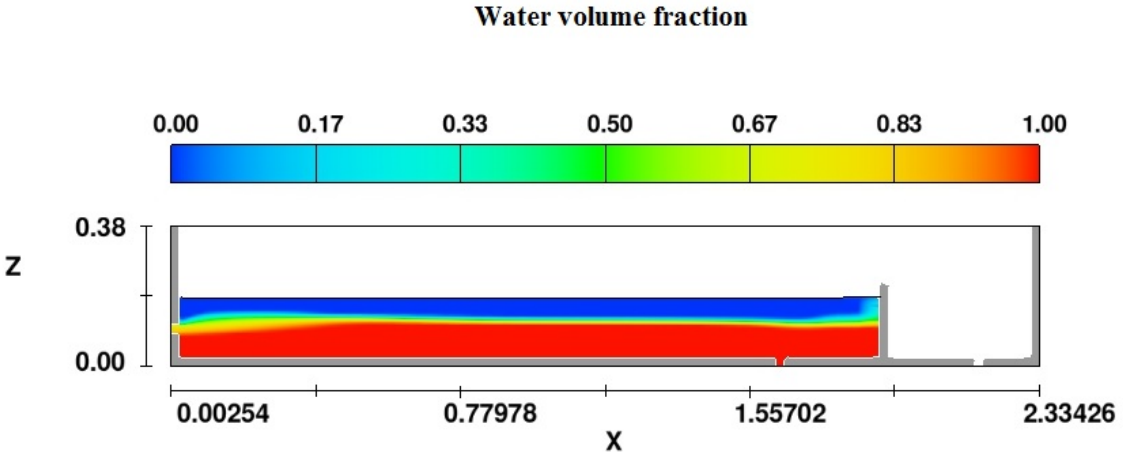

Figure E.6: Steady-state Separation process plots at time = 900 sec

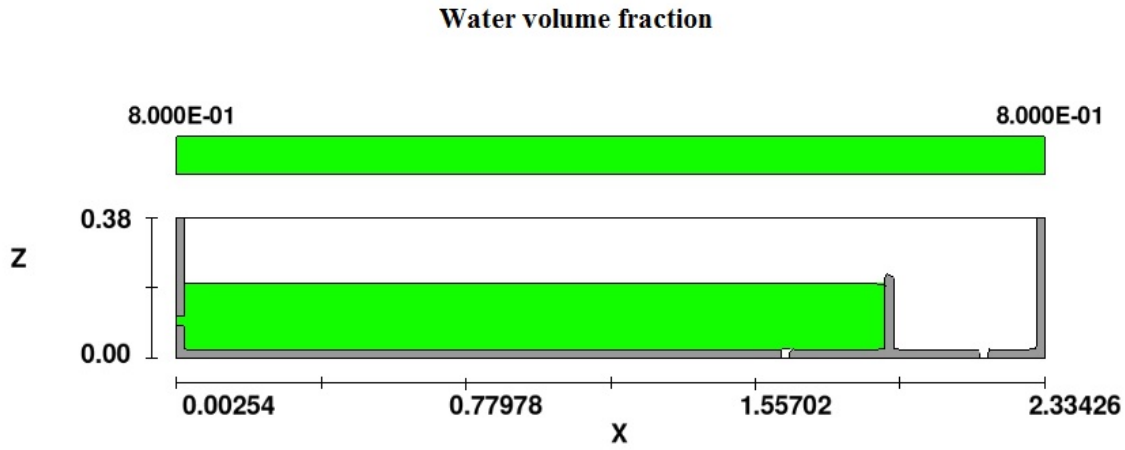

Figure E.7: Steady-state Separation process plots at time = 0 sec

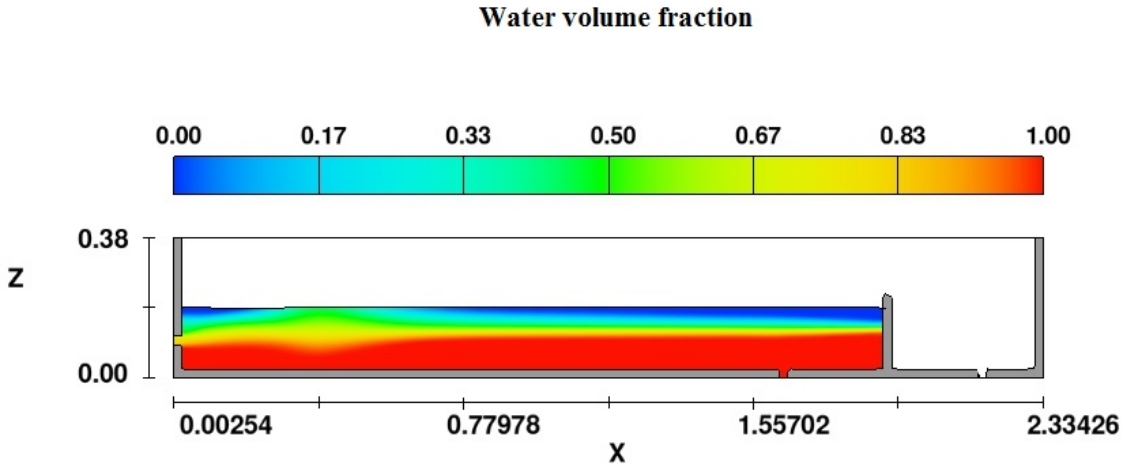

Figure E.8: Steady-state Separation process plots at time = 450 sec

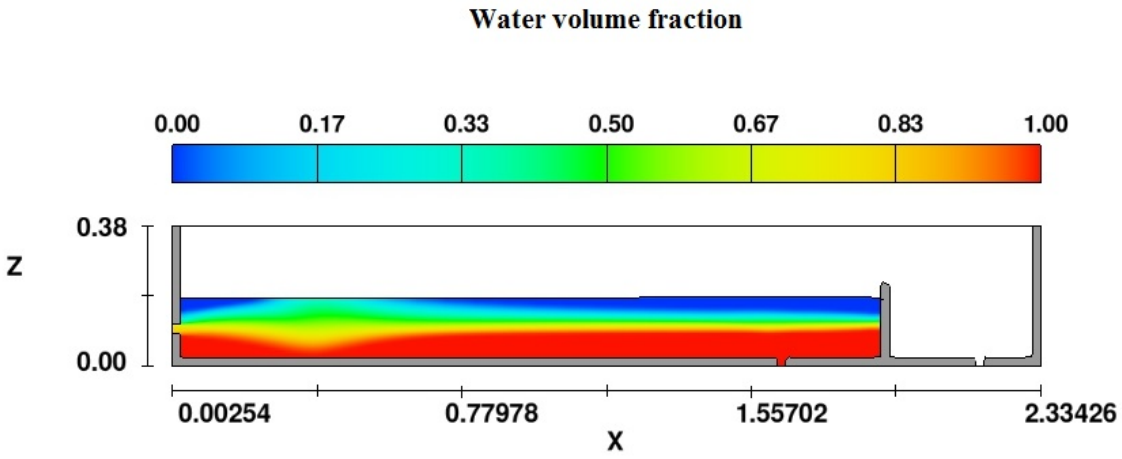

Figure E.9: Steady-state Separation process plots at time = 900 sec

Appendix F

Outline of OpenFoam CFD Simulation

OpenFoam is an open source CFD. A series of C^{++} functions are used to set up a problem. Below each of these functions is identified and briefly described.

The functions are contained in 2 folders. These are **system** and **constant**. Many functions contain Dict, which is an abbreviation of Dictionary, as part of their name.

The main functions in **system** are: controlDict, blockMeshDict, snappyHexMeshDict, meshQualityDict, setFieldsDict, surfaceFeatureExtractDict, fvSchemes, fvSolution.

The main functions in **constant** are: transportProperties, turbulenceProperties, motionProperties, g. The folder **constant** also contains a subfolder trisurface, which contains the stl file for the problem geometry.

The initial conditions on variables are contained in folder **0.orig**. The folder also contains the initial state of the mixture: alpha.air, alpha.water, alpha.oil, epsilon, k, nut, p-rgh, and U.

File **controlDict** identifies the problem type. It gives the start and end times of the

simulation and the maximum allowable courant number of the simulation.

File **blockMeshDict** gives the dimensions of a block that intersects the geometry and creates inlets and outlets for the system. It also identifies boundary types.

File **snappyHexMeshDict** develops the mesh for the simulation. Refinement levels are set by the user.

File **setFieldsDict** sets the initial state of the domain.

File **transportProperties** gives the properties of the fluids in the system such as density and viscosity.

Appendix G

Oil / water Separation Process Plots for OpenFOAM Simulation Results

OpenFOAM was used to investigate the same operating condition as the base case in Fluent. A similar oil volume fraction pattern as the Fluent and Flow-3D is found in OpenFoam, as shown in Figure G.4. After a 900 s residence time, most oil droplets are separated from the water phase, and form an oil phase on the top layer. By 10 s, the separation process has already started, however, there are still a small amount of

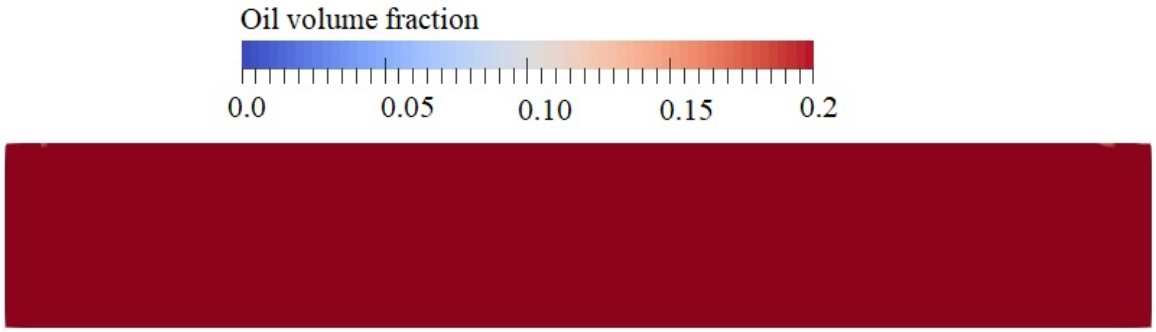

Figure G.1: Oil volume fraction, t = 0 s

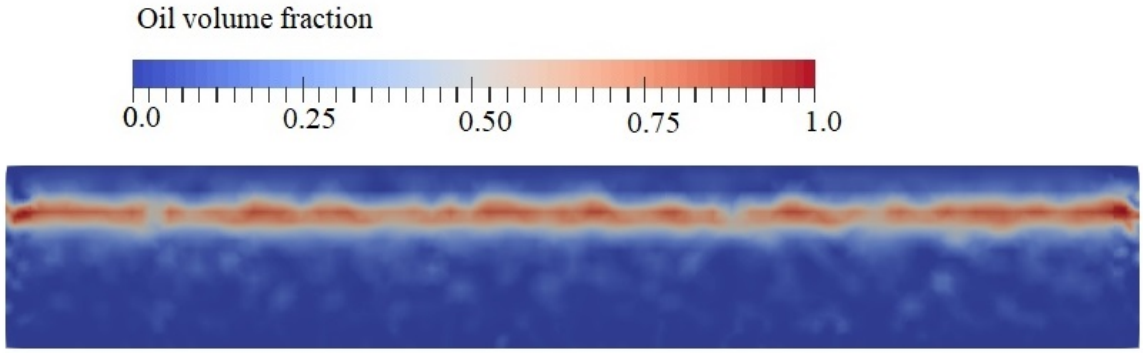

Figure G.2: Oil volume fraction, t = 10 s

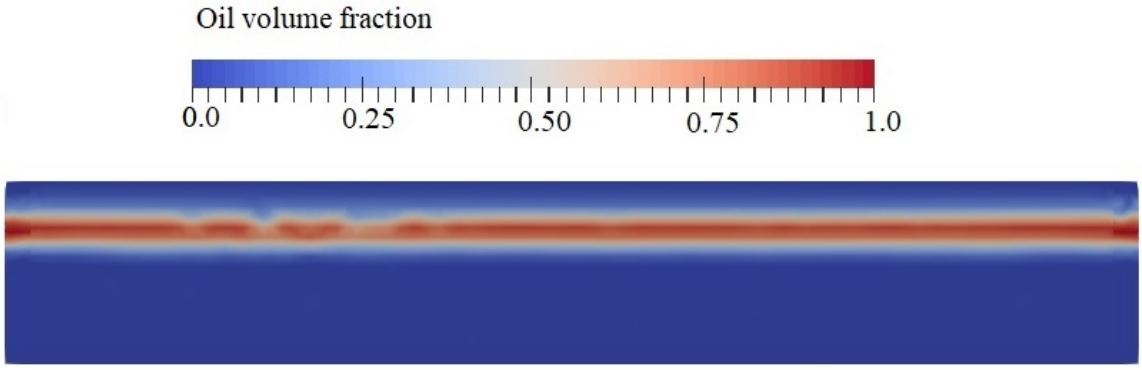

Figure G.3: Oil volume fraction, t = 450 s

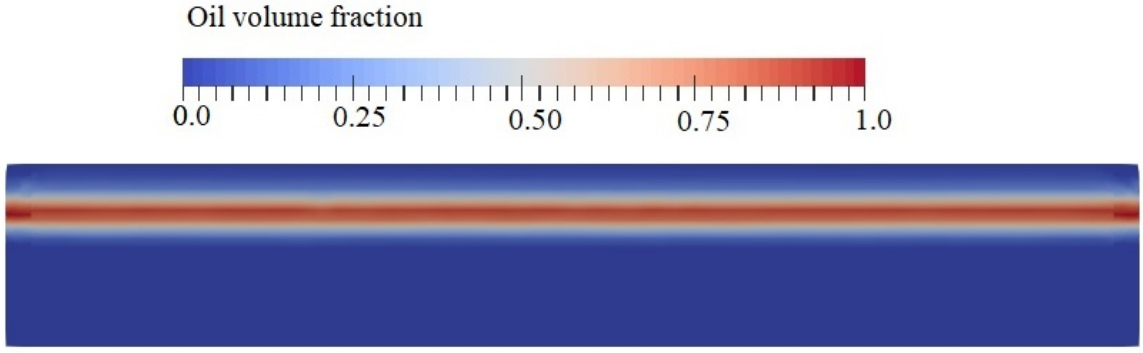

Figure G.4: Oil volume fraction, t = 900 s

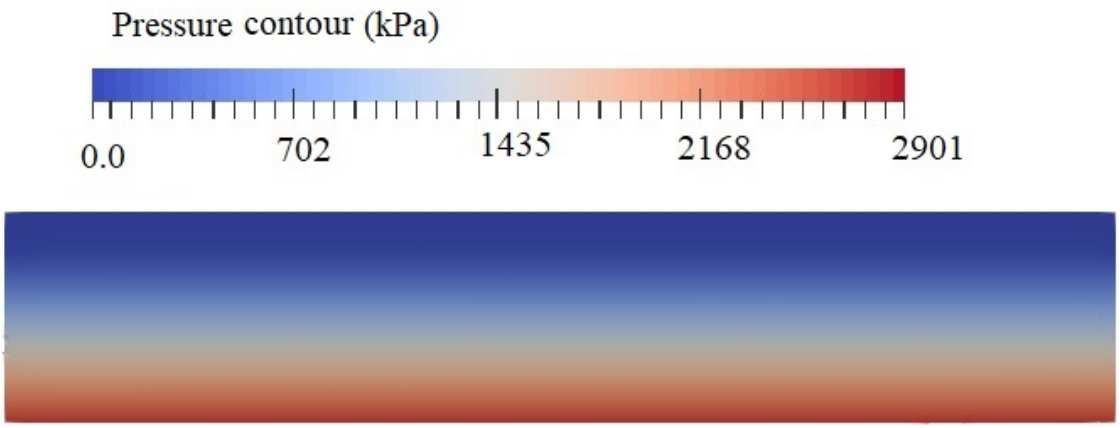

Figure G.5: Pressure distribution in the separator, t = 10 s

oil droplets left in the water phase (Figure G.2 to G.4).

The pressure distribution contour is presented in figure G.5. The bottom layer of the separator is present with the maximum pressure because only the water phase exists. The pressure decreases gradually with the increase in the vertical height. On the top layer, the pressure is 0. In the simulation setup, the operation pressure was defined as the atmospheric pressure, which means that the gage pressure was 0.

Appendix H

OpenFoam Code

/*———————————*- C++ -*———————————-*

version : 2.0;

format : ascii;

class : dictionary;

location : "system";

object : controlDict;

// * //

application : multiphaseInterFoam;

startFrom : startTime;

startTime : 0;

stopAt : endTime;

endTime : 1000;

deltaT : 0.00001;

writeControl : adjustableRunTime;

writeInterval : 250;

purgeWrite : 0;

writeFormat : ascii;

writePrecision: 6;

writeCompression :uncompressed;

timeFormat : general;

timePrecision : 6;

runTimeModifiable :yes;

adjustTimeStep: yes;

maxCo : 1; maxAlphaCo : 1;

maxDeltaT : 0.01;

```
/*--------------------*- C++ -*----------------------*
version: 2.0;
format : ascii;
class : dictionary;
object : blockMeshDict;
// * * * * * * * * * * * * * * * * * * * * * * * * * * * * * * * * * * * * * * * * * * * * * * * * * // convertToMeters 1;
vertices
(
(-0.01 -0.13 -0.20)
( 2.29 -0.13 -0.20)
( 2.29 0.13 -0.20)
(-0.01 0.13 -0.20)

(-0.01 -0.13 0.18)
( 2.29 -0.13 0.18)
( 2.29 0.13 0.18)
(-0.01 0.13 0.18)
);
blocks
(
hex (0 1 2 3 4 5 6 7)    (61 7 10)   simpleGrading (1 1 1)
);
edges
(
);
patches
```

```
(
patch inlet
(0 4 7 3)
patch outlet
(3 2 1 0)
wall others
(1 2 6 5)
(3 7 6 2)
(0 1 5 4)
patch atmosphere
(4 5 6 7)
);
mergePatchPairs
(
);
// ************************************************************//
```

```
/*--------------------*- C++ -*----------------------*
version: 2.0;
format: ascii;
class: dictionary;
location: "constant";
object: transportProperties;
// * * * * * * * * * * * * * * * * * * * * * * * * * * * * * * * * * * * * * * * * * // phases
(
water
transportModel Newtonian;
nu [0 2 -1 0 0 0 0] 1e-06;
rho [1 -3 0 0 0 0 0] 1000;

oil
transportModel Newtonian;
nu [0 2 -1 0 0 0 0] 1e-05;
rho [1 -3 0 0 0 0 0] 800;

air
transportModel Newtonian;
nu [0 2 -1 0 0 0 0] 1e-06;
rho [1 -3 0 0 0 0 0] 1.2;

);
sigmas
(
```

(air water) 0.07

(air oil) 0.03

(water oil) 0.07

);

// **//

```
/*--------------------*- C++ -*----------------------*
version: 2.0;
format: ascii;
class: volVectorField;
location: "0";
object: U;
// * * * * * * * * * * * * * * * * * * * * * * * * * * * * * * * * //
dimensions    [0 1 -1 0 0 0 0];
internalField    uniform (0 0 0);
boundaryField
{
inlet
{
type    fixedValue; value    uniform (0.5 0 0); }
outlet
{
type    pressureInletOutletVelocity; value    uniform (0 0 0);
}
atmosphere
{
type    pressureInletOutletVelocity; value    uniform (0 0 0); }
tank
{
type    noSlip; }
}
// ************************************************************//
```

```
/*--------------------*- C++ -*----------------------*
version: 2.0;
format : ascii;
class : volScalarField;
location : "0";
object : p_rgh;
// * * * * * * * * * * * * * * * * * * * * * * * * * * * * * * * * //
dimensions   [1 -1 -2 0 0 0 0];
internalField    uniform 0;
boundaryField
{
inlet
{
type    fixedFluxPressure;
gradient    uniform 0;
value    uniform 0;
}
outlet
{
type    totalPressure;
p0    uniform 0;
}
atmosphere
{
type    totalPressure;
p0    uniform 0;
```

```
}
tank
{
type    fixedFluxPressure;
gradient    uniform 0;
value    uniform 0;
}
}
// ************************************************************//
```

```
/*--------------------*- C++ -*----------------------*
version: 2.0;
format: ascii;
class: volScalarField;
location: "0";
object: alpha.air;
// * * * * * * * * * * * * * * * * * * * * * * * * * * * * * * * * //
dimensions    [0 0 0 0 0 0 0];
internalField    uniform 1;
boundaryField
{
inlet
{
type     fixedValue;
value     uniform 0;
}
outlet
{
type     zeroGradient;
}
atmosphere
{
type    inletOutlet;
inletValue    uniform 1;
value     uniform 1;
}
```

```
tank
{
type    zeroGradient;
}
}
// ************************************************************************* //
```

```
/*--------------------*- C++ -*----------------------*
version: 2.0;
format: ascii;
class: volScalarField;
location: "0";
object: alpha.oil
// * * * * * * * * * * * * * * * * * * * * * * * * * * * * * * * * //
dimensions    [0 0 0 0 0 0 0];
internalField    uniform 0;
boundaryField
{
inlet
{
type     fixedValue;
value     uniform 0.2;
}
outlet
{
type     zeroGradient;
}
atmosphere
{
type    inletOutlet;
inletValue    uniform 0;
value     uniform 0;
}
```

```
tank
{
type    zeroGradient;
}
}
// ************************************************************* //
```

```
/*--------------------*- C++ -*----------------------*
version: 2.0;
format: ascii;
class: volScalarField;
location: "0";
object: alpha.water
// * * * * * * * * * * * * * * * * * * * * * * * * * * * * * * * * //
dimensions    [0 0 0 0 0 0 0];
internalField    uniform 0;
boundaryField
{
inlet
{
type     fixedValue;
value     uniform 0.8;
}
outlet
{
type     zeroGradient;
}
atmosphere
{
type    inletOutlet;
inletValue    uniform 0;
value     uniform 0;
}
```

```
tank
{
type    zeroGradient;
}
}
// ********************************************************* //
```

```
/*--------------------*- C++ -*----------------------*
version: 2.0;
format: ascii;
class: volScalarField;
location: "0";
object: setFieldsDict
// * * * * * * * * * * * * * * * * * * * * * * * * * * * * * * * * //
defaultFieldValues
( volScalarFieldValue   alpha.air 1
volScalarFieldValue   alpha.water 0
volScalarFieldValue   alpha.oil 0
volVectorFieldValue   U (0 0 0));
regions
(
boxToCell
{
box (0.0 -0.12 -0.19) (2.28 0.12 0.17);
fieldValues
( volScalarFieldValue    alpha.water 0
volScalarFieldValue    alpha.oil 0
volScalarFieldValue   alpha.air 1
);
}
);
// ************************************************************* //
```

```
    /*--------------------------------*- C++ -*----------------------------------*
version: 2.0;
format: ascii;
class: volScalarField;
object: snappyHexMeshDict
// * * * * * * * * * * * * * * * * * * * * * * * * * * * * * * * * * * * * * //
// Which of the steps to run
castellatedMesh true;
snap true;
addLayers false;
// Geometry. Definition of all surfaces. All surfaces are of class
// searchableSurface.
// Surfaces are used
// - to specify refinement for any mesh cell intersecting it
// - to specify refinement for any mesh cell inside/outside/near
// - to 'snap' the mesh boundary to the surface
geometry
{
tank3D.stl
{
type triSurfaceMesh;
name tank;
patchInfo
{ type wall; } }


    };
```

// Settings for the castellatedMesh generation.

castellatedMeshControls

{

// Refinement parameters

//

    // If local number of cells is >= maxLocalCells on any processor switches from from refinement followed by balancing (current method) to (weighted) balancing before refinement.

maxLocalCells 200000000;

// Overall cell limit (approximately). Refinement will stop immediately upon reaching this number so a refinement level might not complete.

// Note that this is the number of cells before removing the part which is not 'visible' from the keepPoint. The final number of cells might actually be a lot less.

maxGlobalCells 2000000000;

// The surface refinement loop might spend lots of iterations refining just a few cells. This setting will cause refinement to stop if <= minimumRefine are selected for refinement. Note: it will at least do one iteration (unless the number of cells to refine is 0)

minRefinementCells 0;

// Number of buffer layers between different levels.

// 1 means normal 2:1 refinement restriction, larger means slower refinement.

nCellsBetweenLevels 2;

// Explicit feature edge refinement

//

    // Specifies a level for any cell intersected by its edges.

// This is a featureEdgeMesh, read from constant/triSurface for now.

features

(

{ file "tank3D.eMesh";

level 2; }

);

// Surface based refinement

// Specifies two levels for every surface. The first is the minimum level, every cell intersecting a surface gets refined up to the minimum level.

// The second level is the maximum level. Cells that 'see' multiple intersections where the intersections make an angle $resolveFeatureAnglegetrefineduptothemaximumlevel.$

$refinementSurfaces$

{

tank { // Surface-wise min and max refinement level level (1 2); }

}

// Feature angle:

// - used if min and max refinement level of a surface differ used if feature snapping (see snapControls below) is used resolveFeatureAngle 30;

//- Optional increment (on top of max level) in small gaps gapLevelIncrement 2;

// Planar angle: used to determine if surface normals // are roughly the same or opposite. Used

// - in proximity refinement // - to decide when to merge free-standing baffles (if e.g. running in surfaceSimplify mode set this to 180 to merge all baffles) // - in

snapping to avoid snapping to nearest on 'wrong' side of thin gap

// If not specified same as resolveFeatureAngle planarAngle 30;

// Region-wise refinement
//

// Specifies refinement level for cells in relation to a surface. One of three modes
// - distance. 'levels' specifies per distance to the surface the wanted refinement level. The distances need to be specified in descending order.
// - inside. 'levels' is only one entry and only the level is used. All cells inside the surface get refined up to the level. The surface needs to be closed for this to be possible.
// - outside. Same but cells outside.

refinementRegions { }
// Mesh selection
//

// After refinement patches get added for all refinementSurfaces and all cells intersecting the surfaces get put into these patches. The section reachable from the locationInMesh is kept.
// NOTE: This point should never be on a face, always inside a cell, even after refinement.
locationInMesh (1.0 0.0 0.0);

// Whether any faceZones (as specified in the refinementSurfaces) are only on the boundary of corresponding cellZones or also allow free-standing zone faces. Not used if there are no faceZones.

allowFreeStandingZoneFaces false; //true;

}

// Settings for the snapping.

snapControls

{ //- Number of patch smoothing iterations before finding correspondence to surface

nSmoothPatch 5;

// Number of smoothing of internal points on refinement interfaces

nSmoothInternal $nSmoothPatch;

//- Relative distance for points to be attracted by surface feature point or edge. True distance is this factor times local maximum edge length.

tolerance 2.0;

//- Number of mesh displacement relaxation iterations. nSolveIter 30;

//- Maximum number of snapping relaxation iterations. Should stop before upon reaching a correct mesh.

nRelaxIter 5;

// Feature snapping

//- Number of feature edge snapping iterations.

// Leave out altogether to disable.

```
nFeatureSnapIter 10;

    //- Detect (geometric only) features by sampling the surface
// (default=false).
implicitFeatureSnap false;

    //- Use castellatedMeshControls::features (default = true)
explicitFeatureSnap true;

    //- Detect points on multiple surfaces (only for explicitFeatureSnap)
multiRegionFeatureSnap true;//false;

    //-When to run face spliting ( never at first iteration, always at last iteration
// Is interval. Deafault -1 (disabled)
// Recommendation: set to half the number of feature snap iterations

    nFcaeSplitInterval 10;
}

    // Settings for the layer addition.
addLayersControls
{
// Are the thickness parameters below relative to the undistorted size of the refined
cell outside layer (true) or absolute sizes (false).
relativeSizes false;
```

// Per final patch (so not geometry!) the layer information layers { }

// Expansion factor for layer mesh

expansionRatio 1.2;

// Wanted thickness of final added cell layer. If multiple layers is the thickness of the layer furthest away from the wall.

// Relative to undistorted size of cell outside layer.

// See relativeSizes parameter.

firstLayerThickness 0.00357;

// Minimum thickness of cell layer. If for any reason layer cannot be above minThickness do not add layer.

// See relativeSizes parameter.

minThickness 0.00357;

// If points get not extruded do nGrow layers of connected faces that are also not grown. This helps convergence of the layer addition process close to features.

// Note: changed(corrected) w.r.t 17x! (didn't do anything in 17x)

nGrow 0;

// Advanced settings

// Static analysis of starting mesh

// When not to extrude surface. 0 is flat surface, 90 is when two faces are per-

pendicular
featureAngle 60;

// When to merge patch faces. Default is featureAngle. Useful when featureAngle is large.
//mergePatchFacesAngle 45;
// Stop layer growth on highly warped cells
maxFaceThicknessRatio 100;

// Patch displacement

// Number of smoothing iterations of surface normals nSmoothSurfaceNormals 10;

// Smooth layer thickness over surface patches nSmoothThickness 150;

// Do not extrude around sharp edge if not both faces are extruded.
// Default is 0.5*featureAngle. Set to -180 always attempt extrusion
layerTerminationAngle 60;
// Medial axis analysis (for use with default displacementMedialAxis)
// Angle used to pick up medial axis points
// Note: changed(corrected) w.r.t 17x! 90 degrees corresponds to 130
// in 17x.
minMedialAxisAngle 90;

// Reduce layer growth where ratio thickness to medial distance is large
maxThicknessToMedialRatio 100; //0.3;

```
    // Number of smoothing iterations of interior mesh movement direction
nSmoothNormals 3;

    // Optional: limit the number of steps walking away from the surface.
// Default is unlimited.
nMedialAxisIter 10;

    // Optional: smooth displacement after medial axis determination.
// default is 0.
nSmoothDisplacement 90;

    // (wip)Optional: do not extrude any point where (false) : all surrounding faces
are not fully extruded
// (true) : all surrounding points are not extruded // Default is false.
//detectExtrusionIsland true;

    // Optional: at non-patched sides allow mesh to slip if extrusion
// direction makes angle larger than slipFeatureAngle. Default is
// 0.5*featureAngle.
slipFeatureAngle 30;

    // Maximum number of snapping relaxation iterations. Should stop
// before upon reaching a correct mesh.
nRelaxIter 5;
```

/* // Mesh shrinking

// Select the solver-based mesh shrinking method meshShrinker displacement-MotionSolver;

// Select the Laplacian method solver displacementLaplacian;

// Settings for the Laplacian method
displacementLaplacianCoeffs
{ //- Increase diffusivity close to all walls
diffusivity quadratic inverseDistance
1("JBC.*");
}
*/
// Create buffer region for new layer terminations, i.e. gradually
// step down number of layers. Set to <0 to terminate layer in one go.
nBufferCellsNoExtrude 0;
// Overall max number of layer addition iterations. The mesher will exit if it reaches this number of iterations; possibly with an illegal mesh.
nLayerIter 50;
// Max number of iterations after which relaxed meshQuality controls get used. Up to nRelaxedIter it uses the settings in
// meshQualityControls,
// after nRelaxedIter it uses the values in meshQualityControls::relaxed.
nRelaxedIter 50;
// Additional reporting: if there are just a few faces where there are mesh errors

(after adding the layers) print their face centres.

// This helps in tracking down problematic mesh areas.

//additionalReporting true;

}

// Generic mesh quality settings. At any undoable phase these determine where to undo.

meshQualityControls

{

include "meshQualityDict"

// Optional : some meshing phases allow usage of relaxed rules.

// See e.g. addLayersControls::nRelaxedIter.

relaxed

{ // Maximum non-orthogonality allowed. Set to 180 to disable.

maxNonOrtho 75; }

// Advanced

// Number of error distribution iterations nSmoothScale 4;

// amount to scale back displacement at error points errorReduction 0.75;

}

// Advanced

// writeFormat ASCII;

//// Write flags

writeFlags

```
(
// scalarLevels    // write volScalarField with cellLevel for postprocessing
// layerSets    // write cellSets, faceSets of faces in layer
// layerFields    // write volScalarField for layer coverage
);

    // Merge tolerance. Is fraction of overall bounding box of initial mesh.
// Note: the write tolerance needs to be higher than this. mergeTolerance 1e-5;
// ************************************************************************* //
```